

## **INFORMATION TO USERS**

**This manuscript has been reproduced from the microfilm master. UMI films the text directly from the original or copy submitted. Thus, some thesis and dissertation copies are in typewriter face, while others may be from any type of computer printer.**

**The quality of this reproduction is dependent upon the quality of the copy submitted. Broken or indistinct print, colored or poor quality illustrations and photographs, print bleedthrough, substandard margins, and improper alignment can adversely affect reproduction.**

**In the unlikely event that the author did not send UMI a complete manuscript and there are missing pages, these will be noted. Also, if unauthorized copyright material had to be removed, a note will indicate the deletion.**

**Oversize materials (e.g., maps, drawings, charts) are reproduced by sectioning the original, beginning at the upper left-hand corner and continuing from left to right in equal sections with small overlaps.**

**Photographs included in the original manuscript have been reproduced xerographically in this copy. Higher quality 6" x 9" black and white photographic prints are available for any photographs or illustrations appearing in this copy for an additional charge. Contact UMI directly to order.**

**Bell & Howell Information and Learning  
300 North Zeeb Road, Ann Arbor, MI 48106-1346 USA  
800-521-0600**

**UMI<sup>®</sup>**



***Desulfurization of INCO Semi-Blister Copper***

by

**Ioannis John Roumeliotis**

**Department of Mining and Metallurgical Engineering  
McGill University  
Montreal, Canada**

**January 1999**

**A thesis submitted to the Faculty of Graduate Studies and  
Research in partial fulfillment of the requirements  
for the degree of Master of Engineering**

**© I. J. Roumeliotis**



**National Library  
of Canada**

**Acquisitions and  
Bibliographic Services**

395 Wellington Street  
Ottawa ON K1A 0N4  
Canada

**Bibliothèque nationale  
du Canada**

**Acquisitions et  
services bibliographiques**

395, rue Wellington  
Ottawa ON K1A 0N4  
Canada

*Your file Votre référence*

*Our file Notre référence*

**The author has granted a non-exclusive licence allowing the National Library of Canada to reproduce, loan, distribute or sell copies of this thesis in microform, paper or electronic formats.**

**The author retains ownership of the copyright in this thesis. Neither the thesis nor substantial extracts from it may be printed or otherwise reproduced without the author's permission.**

**L'auteur a accordé une licence non exclusive permettant à la Bibliothèque nationale du Canada de reproduire, prêter, distribuer ou vendre des copies de cette thèse sous la forme de microfiche/film, de reproduction sur papier ou sur format électronique.**

**L'auteur conserve la propriété du droit d'auteur qui protège cette thèse. Ni la thèse ni des extraits substantiels de celle-ci ne doivent être imprimés ou autrement reproduits sans son autorisation.**

0-612-50657-6

**Canada**

The INCO finishing procedure represents the near final stages of copper production at the Copper Cliff Smelter in Sudbury, Ontario, whereby semi-blister copper, at 4-6 wt % Ni and 2-3 wt % S, is processed into blister copper, at 100 ppm S and 0.4 wt % Ni, in a modified Pierce-Smith converter combining top-blown oxygen injection and bottom-blown nitrogen stirring of the melt to accelerate semi-blister desulfurization. The procedure is performed in two stages of equal duration: in the first, melt saturation with oxygen and sulfur elimination from 2-3 wt % S to 300 ppm is achieved by 45 minutes of oxygen top-blowing and nitrogen bottom stirring; in the second stage, oxygen injection is terminated and sulfur removal from 300 ppm to 30-100 ppm proceeds by the reaction of dissolved S and O under a further 45 minutes of nitrogen stirring.

The apparent decrease in the rate kinetics of sulfur elimination during second stage finishing prompted an investigation into the possible causes impeding sulfur removal. Two possible causes were identified: the cessation of surface tension driven flow, or 'Marangoni convection', upon oxygen saturation of the melt and surface coverage by nickel oxidation. In this study 1 to 2 kg liquid charges of Cu - 1 wt % S, Cu - 3 wt % Ni and cathode copper were impinged with an oxygen gas stream of 75 cm<sup>3</sup>/min from a gas lance 1.5 cm above the melt surface to examine whether Marangoni convection can indeed be provoked in these systems and to compare sulfur elimination between Cu-S and Cu-Ni-S melts. Marangoni convection was not observed in these systems but surface oxidation did occur readily and was found to impede sulfur elimination; the effect being more pronounced in the Cu-Ni-S melts.

Cu-S and Cu-Ni-S alloys were also exposed to the open atmosphere to examine desulfurization of stagnant melts under air. Although surface oxidation immediately occurred in these melts, it was found that at a particular concentration of S and O in the liquid Cu-S alloy the melt periodically erupted with effervescence resulting in disintegration of the oxidized surface layer and accelerated S removal. The Cu-Ni-S alloy which did not undergo spontaneous bubbling maintained the integrity of its slag layer and sulfur removal was therefore gradual.

La procédure d'affinage INCO représente le stage une des dernières étapes de la production de cuivre à l'affinerie Copper Cliff de Sudbury, en Ontario. Dans cette opération, le cuivre semi-blister (c.-à-d. ayant des cloques en surface), à 4-6 % pds de Ni et 2-3 % pds de S, est traité pour être transformé en cuivre blister contenant 100 ppm de S et 0,4 % pds de Ni. Ce traitement a lieu dans un convertisseur Pierce-Smith modifié dans lequel on insuffle de l'oxygène au haut du four et, au bas, de l'azote qui assure le mélange du métal en fusion pour accélérer la désulfuration du semi-blister. L'opération s'effectue en deux étapes de durée égale (45 minutes). Au cours de la première, on sature le métal en fusion d'oxygène et on en réduit la teneur en soufre à 300 ppm en continuant à souffler l'oxygène par le haut et l'azote par le bas pour assurer le mélange. À la seconde étape, on cesse d'injecter de l'oxygène mais la réduction de la teneur en soufre, se poursuit jusqu'à 30 à 100 ppm. par réaction de S et de O dissous grâce au mélange par l'azote.

La diminution apparente de la cinétique d'élimination du soufre au cours de la seconde étape de l'affinage a donné lieu à une étude visant à déterminer les causes susceptibles de nuire à cette élimination. Nous avons identifié deux causes possibles: la cessation d'écoulement induit par la tension superficielle, ou convection de Marangoni, après saturation en oxygène du métal fondu, et la formation d'une couche de nickel oxydé à la surface. Dans le cadre de l'étude, des phases liquides à 1 kg - 2 kg de Cu à 1 % pds de S, de Cu à 3 % pds de Ni et 1 % pds S, et de cuivre pur ont été bombardées d'un flux de gaz d'oxygène de 75 cm<sup>3</sup>/min provenant d'une buse à gaz placée à 1,5 cm au-dessus de la surface du métal en fusion, afin de déterminer s'il était effectivement possible de provoquer la convection de Marangoni dans ces systèmes et pour comparer les taux d'élimination du soufre dans le Cu-S et le Cu-Ni-S en fusion. On n'a pas observé de convection de Marangoni dans ces systèmes; par contre, l'oxydation en surface s'y produit facilement et affecte l'élimination de soufre, cet effet étant plus prononcé dans le cas du Cu-Ni-S en fusion.

On a aussi exposé les alliages Cu-S et Cu-Ni-S à l'air libre pour étudier le processus de désulfuration des bains stagnants à l'air. Même s'il y avait oxydation immédiate à la surface de ces alliages en fusion, il a été déterminé qu'une certaine concentration de S et de O dans l'alliage liquide Cu-S provoquait périodiquement l'effervescence du métal fondu, ce

qui entraînait la désintégration de la couche superficielle oxydée et accélérât l'élimination du S. Dans le cas de l'alliage Cu-Ni-S, qui ne connaissait pas un tel bouillonnement spontané, l'intégrité de la couche de scories étant maintenue, l'élimination du soufre se faisait moins rapidement.

This research program could not have been carried out without the financial support of NSERC and INCO which in the case of the latter was complemented by the indispensable technical support provided by its staff, Dr. Sam Marcuson, Mike Humphries, and Jin Liu, and through the use of its analytical facilities at Copper Cliff.

Special thanks to the teaching staff of the Department of Mining and Metallurgical Engineering at McGill University, including Department Chairman Prof. G. Demopoulos for his personal involvement in the course of this investigation, Prof. A. Laplante for his discussion on statistical analysis and in conjunction with Florence Paray as co-editor of the translated abstract, and especially my supervisor Prof. Ralph Harris whose continued faith, moral encouragement, technical assistance and discussions proved invaluable for the completion of this study.

The technical staff of the Department of Mining and Metallurgical Engineering who also deserve particular mention are H. Ward, M. Riendeau, R. Paquette, H. Campbell and E. Fernandez for providing technical assistance and consultation beyond their duty requirements. To former and fellow graduate students, T. Brzezinski, Y. Baik, R. Sankanarayanan, H. Abulewufa, B. Handle, M. Ikezawa, T. Luganova-Shrenyakova and Qi Xia, I would like to thank them all for providing a forum for moral support and technical discourse while H. Abulewufa's contribution of his data acquisition equipment for use in this study was additionally appreciated.

Gratitude and recognition go to Claudia Cieri and Richard Thesi for their time and effort donated to translating the abstract of this thesis to french. I would also like to thank my immediate family, Eugenia, Ioanna, Demosthenes and David for providing continued encouragement throughout this research program and to Donatella Battista whose faith, support and inspiration were indispensable for completing this work. Additional thanks also go out to John Kappos, Sami Ramadan and other friends for their moral support and other intangible contributions.

# ***Table of Contents***

v

---

<b>Abstract</b> .....	<b>I</b>
<b>Résumé</b> .....	<b>ii</b>
<b>Acknowledgements</b> .....	<b>iv</b>
<b>Table of Contents</b> .....	<b>v</b>
<b>List of Figures</b> .....	<b>vii</b>
<b>List of Tables</b> .....	<b>xii</b>
<b>Nomenclature</b> .....	<b>xiii</b>
<b>Chapter 1. Introduction</b> .....	<b>1</b>
1.1 The Smelter Flowsheet in 1992.....	1
1.2 The Smelter Flowsheet in 1993.....	4
1.3 Blister Copper Production from MK Concentrate .....	5
1.3.1 Oxygen Flash Converting of MK Concentrate to Semi-Blister .....	5
1.3.2 Finishing of Semi-Blister to Blister.....	7
1.4 Research Objectives.....	10
<b>Chapter 2. Literature Review</b> .....	<b>11</b>
2.1 Thermodynamics and Thermochemistry of Copper Converting.....	11
2.1.1 Conventional Copper Converting.....	11
2.1.2 Copper Converting at INCO.....	13
2.2 Gas-Liquid Interactions.....	17
2.2.1 Top Blown Gas Injection with High Momentum Jets.....	18
2.2.2 Top Blown Gas Injection with Low Momentum Jets.....	20
2.3 Interfacial Phenomena.....	22
2.3.1 Surface Active Solutes and Surface Tension.....	22
2.3.2 The Role of Surface Active Solutes on Reaction Rates.....	27
2.3.3 Surface Tension Driven Flow.....	29
2.4 Oxidation Studies.....	32
2.5 Hypothesis.....	39
<b>Chapter 3. Experimental Methodology</b> .....	<b>40</b>
3.1 Experimental Program.....	40
3.2 Test Apparatus.....	40
3.2.1 Design Criteria.....	40
3.2.2 Selection of Furnace Technology.....	40
Parabolic Clamshell Heater.....	40
Silicon Carbide Resistance Heating Furnace.....	42
3.2.3 Reaction Vessel.....	45
3.2.4 Gas Regulation System.....	49

# Table of Contents

vi

	Gas Evacuation/Ventilation.....	49
	Gas Delivery.....	49
3.3	Experimental procedure.....	49
	Test 1 - Test 6.....	49
	Test 7 - Test 9.....	50
3.4	Elemental Analyses.....	50
3.5	Charge Preparation.....	51
3.5.1	In Situ Alloy Preparation.....	53
3.5.2	Master Alloy Preparation.....	54
3.6	Selection of Experimental Conditions.....	56
<b>Chapter 4.</b>	<b>Results.....</b>	<b>58</b>
4.1	Experimental Results.....	58
	Test 1: Desulfurization of a Cu - 3 wt % S Alloy.....	58
	Test 2: Desulfurization of a Cu - 1 wt % S Alloy with 66 cm <sup>3</sup> O <sub>2</sub> /min.....	61
	Test 3: Desulfurization of a Cu - 1 wt % S Alloy with 75 cm <sup>3</sup> O <sub>2</sub> /min.....	65
	Test 4: Desulfurization of Cu - 3 wt % Ni - 1 wt % S Alloy with 75 cm <sup>3</sup> O <sub>2</sub> /min.....	67
	Test 5, Test 6: Oxidation of Cathode Copper with 75 and 372 cm <sup>3</sup> O <sub>2</sub> /min.....	70
	Test 7, Test 8: Desulfurization of Cu-1 wt % S Alloy Exposed to Air.....	73
	Test 9: Desulfurization of Cu - 3 wt % Ni - 1 wt % S Alloy Exposed to Air.....	78
4.2	Discussion of Errors.....	81
<b>Chapter 5.</b>	<b>Discussion.....</b>	<b>83</b>
5.1	Discussion of Results.....	83
5.1.1	Marangoni Convection.....	83
5.1.2	The Role of Surface Films on Mass Transfer.....	85
5.1.3	Melt Effervescence.....	86
5.2	Summary.....	89
<b>Chapter 6.</b>	<b>Conclusions.....</b>	<b>91</b>
<b>Chapter 7.</b>	<b>Recommendations for Future Work.....</b>	<b>93</b>
<b>Appendix A.</b>	<b>X-Ray /SEM Analyses.....</b>	<b>94</b>
<b>References</b>	<b>.....</b>	<b>96</b>

**Chapter 1**

Figure 1.	The Copper Cliff Smelter flowsheet in 1992 operating separate nickel and copper production circuits <sup>2</sup> .....	2
Figure 2.	The current Copper Cliff Smelter flowsheet after implementation of process and equipment modifications in 1993 <sup>2</sup> .....	4
Figure 3.	The INCO Multi-purpose vessel (MPV) for finishing of semi-blister to blister <sup>1</sup> .....	8
Figure 4.	Process curve of sulfur for the INCO MPV <sup>19</sup> . Stage I sulfur elimination is performed by oxygen top-blowing and enhanced by nitrogen stirring. In Stage II, oxygen injection is terminated while nitrogen agitation of the melt is continued.....	9

**Chapter 2**

Figure 5.	The Cu-S phase diagram showing the oxidation path of Cu <sub>2</sub> S to blister Cu during conventional converting according to Biswas and Davenport <sup>21</sup> . The shaded region depicts the operating zone of the INCO finishing procedure.....	13
Figure 6.	The phase relations of the copper-rich region of the Cu-Ni-S phase diagram at 1473 K shown superimposed on the isoactivity line of Ni and S according to Larrain and Lee <sup>19,32</sup> .....	15
Figure 7.	The phase relations and various isotherms of the copper-rich corner of the Cu-Ni-O system according to Taskinen <sup>36</sup> and Kuxmann and Riecke <sup>38</sup> . The arrows trace the oxidation path followed by nickel during the INCO finishing procedure <sup>19</sup> .....	15
Figure 8.	The composition and temperature changes experienced by the copper charge during a pilot plant test of the INCO finishing procedure <sup>19</sup> .....	16
Figure 9.	(a) Dimpling of a liquid surface by a low momentum gas jet. (b) Increasing the jet momentum beyond a critical value results in splashing i.e. ejection of material from the impingement area. (c) At high jet momentum the gas penetrates the liquid resulting in a lower volume of ejected material. (d) Schematic depiction of the geometric model developed by Wakelin <sup>65</sup> and the ensuing dimensionless relationship.....	19
Figure 10.	Types of adsorption behaviour observed at liquid-metal interfaces (a) positive adsorption (b) negative adsorption (c) electrocapillary behaviour, according to Brimacombe <sup>72</sup> .....	23
Figure 11.	Effect of (a) dissolved oxygen and (b) dissolved sulphur on the surface tension of liquid copper at various temperatures according to Monma and Suto <sup>73</sup> .....	24

Figure 12.	Surface renewal by eddies at interfaces: (a) no surface active material present (b) in the presence of surface active material according to Richardson <sup>79</sup> .....	28
Figure 13.	Macro-scale interfacial motion on the surface of liquid copper generated by (a) the impingement of an oxygen jet on the melt surface which leads to (b) radial spreading of the oxide patch at high velocity towards the regions of highest surface tension (c).....	31
Figure 14.	(a) Micro-scale interfacial motion generated by the penetration of eddies at the gas-liquid interface with a solute composition exceeding that of the interface resulting in motion towards regions of higher interfacial tension according to Brimacombe <sup>72</sup> . (b) Macro-scale interfacial motion generated by the dissolution of a partially immersed solid resulting in liquid motion away from the solid-liquid interface when there is positive adsorption of the solute on the liquid surface and towards the solid-liquid interface when there is negative solute adsorption on the liquid surface according to Brimacombe <sup>72</sup> .....	32
Figure 15.	Variation of the sulfur dioxide pressure in equilibrium with $\text{Cu}_{(s)}$ , $\text{Cu}_2\text{S}$ , $\text{Cu}_2\text{O}$ and the liquidus curve of copper <sup>96</sup> .....	35
<b>Chapter 3</b>		
Figure 16.	Temperature versus total, normal emissivity of heavily oxidized stainless steel and aluminum oxide <sup>103</sup> .....	42
Figure 17.	Schematic representation of the (a) profile and (b) plan view of the silicon carbide resistance furnace designed and used in this investigation.....	43
Figure 18.	The time-temperature profiles of an iron block heated to 1473 K in the clamshell radiation furnace and to 1523 K in the SiC resistance furnace....	44
Figure 19.	Wiring diagram for the SiC resistance furnace featuring two Omega CN9111 series controllers which allowed for high thermal stability in the bath.....	45
Figure 20.	Schematic representation of the (a) cross section of the reaction vessel, crucible and accessories and (b) plan view of the Al water jacket and its access ports.....	46
Figure 21.	Schematic representation of the test apparatus when the quartz reaction vessel and graphite receptacle were used.....	47
Figure 22.	Photograph of the test apparatus during operation.....	48
Figure 23.	Broadside and cross section of the cathode copper sheet. Elemental analyses were performed on the shaded regions.....	52
Figure 24.	Cross section of crucible and solidified slag layer from Test 1.....	53

## List of Figures

ix

Figure 25.	Regions of alloy ingot sampled for elemental determinations.....	55
<b>Chapter 4</b>		
Figure 26.	The dissolved S and O concentration profile over time in Test 1. The vertical line coincides with the introduction of the O <sub>2</sub> -N <sub>2</sub> gas mixture onto the melt surface at 170.6 cm <sup>3</sup> /min and $\mathcal{P}_{O_2} = 0.62$ .....	59
Figure 27.	Photograph of the luminescent patch beneath the tip of the gas lance in Test 1 at the start of O <sub>2</sub> -N <sub>2</sub> gas blowing. The dark spot on the tube is a large droplet of material that had been ejected from the bath.....	60
Figure 28.	(a) Schematic diagram of the region on the quartz tube most affected by the melt ejections. (b) Photograph of the fractured reaction vessel near its radial bottom ringed with droplets of copper/copper oxide.....	60
Figure 29.	The time-temperature profile of the alloy melt in Test 1 relative to the sampling time. The horizontal line marks the bath setpoint temperature of 1498 K.....	61
Figure 30.	The dissolved S and O concentration profiles over time in Test 2. The vertical line coincides with the introduction of pure O <sub>2</sub> onto the melt surface at 66 cm <sup>3</sup> /min.....	63
Figure 31.	The time temperature profile of the melt in Test 2 relative to the sampling time $t = 0$ ; the depression in the curve near 1400 K indicates liquefaction of the alloy charge while the horizontal line marks the bath setpoint temperature of 1523 K.....	63
Figure 32.	Photographs of the alloy surface and oxide film from Test 2 at (a) 1523 K and $t = 70$ minutes; a highly emissive solid or liquid oxide near the crucible wall is surrounded by the darker liquid alloy and (b) room temperature where the blistered alloy surface is partially covered by dark regions of oxidized copper.....	64
Figure 33.	Photograph of the quartz reaction vessel, from Test 2, along its vertical length showing solidified droplets of ejected material.....	64
Figure 34.	The dissolved S and O concentration profile over time for Test 3 at 1523 K. The vertical line coincides with the introduction of pure O <sub>2</sub> onto the melt surface at 75 cm <sup>3</sup> /min.....	66
Figure 35.	The time temperature profile of the melt in Test 3 relative to the sampling time $t = 0$ ; the depression in the curve near 1400 K indicates liquefaction of the alloy charge while the horizontal line marks the bath setpoint temperature of 1523 K.....	67

## List of Figures

x

Figure 36.	The dissolved S, O and Ni concentration profile over time in Test 4. The first and second vertical lines coincide respectively with the introduction of pure O <sub>2</sub> onto the melt surface at 75 cm <sup>3</sup> /min and then at 372 cm <sup>3</sup> /min.....	69
Figure 37.	Photograph of the melt surface in Test 4 covered by an emissive oxide film at 1523 K and t = 40 minutes. The dark region is the liquid metal surface that was exposed after a sample had been extracted from the melt.....	69
Figure 38.	The time temperature profile of the melt in Test 4 relative to the sampling time t = 0; the depression in the curve near 1400 K indicates liquefaction of the alloy charge while the horizontal line marks the bath setpoint temperature of 1523 K.....	70
Figure 39.	The dissolved O concentration profile over time in Test 6. The first and second vertical lines coincide respectively with the introduction of pure O <sub>2</sub> onto the melt surface at 75 cm <sup>3</sup> /min and then at 372 cm <sup>3</sup> /min .....	72
Figure 40.	Photographs of the melt surface at 1523 K in (a) Test 6 covered by an emissive oxide layer after 22 minutes of O <sub>2</sub> blowing (i.e. t <sub>sampling</sub> = 32 minutes) and (b) Test 5 after 35 minutes of O <sub>2</sub> blowing at 75 cm <sup>3</sup> /min; note the mirror image of the gas lance on the dark but reflective melt surface....	72
Figure 41.	The time temperature profile of the melt in Test 6 relative to the sampling time t = 0; the depression in the curve near 1400 K indicates liquefaction of the alloy charge while the horizontal line marks the bath setpoint temperature of 1523 K.....	73
Figure 42.	Photograph of the melt surface in Test 8 covered by an emissive oxide at approximately t = 0 minutes. The darker spots are the exposed surface of the liquid alloy.....	75
Figure 43.	Photograph of the melt surface effervescing in Test 8 at t = 28 minutes.....	76
Figure 44.	The dissolved S and O concentration profiles over time for Test 7 and Test 8. The dashed and solid vertical lines respectively mark the occurrence and duration of effervescence in Test 7 and Test 8.....	76
Figure 45.	The time temperature profile of the melt in Test 7 relative to the sampling time t = 0; the plateau in the curve near 1400 K indicates liquefaction of the alloy charge while the horizontal line marks the bath setpoint temperature of 1523 K.....	77
Figure 46.	The time temperature profile of the melt in Test 8 relative to the sampling time t = 0; the plateau in the curve near 1400 K indicates liquefaction of the alloy charge while the horizontal line marks the bath setpoint temperature of 1523 K.....	77

Figure 47.	The S, O and Ni concentration profiles over time in Test 9. The vertical lines coincide respectively with the introduction of pure O <sub>2</sub> onto the melt surface at 75 cm <sup>3</sup> /min and submerged nitrogen injection at 2000 cm <sup>3</sup> /min.....	79
Figure 48.	Photograph of the melt surface in Test 9 covered by an oxide layer at t = 32 minutes.....	80
Figure 49.	The time temperature profile of the melt in Test 9 relative to the sampling time t = 0; the plateau in the curve near 1400 K indicates liquefaction of the alloy charge while the horizontal line marks the bath setpoint temperature of 1523 K.....	80
<b>Chapter 5</b>		
Figure 50.	The concentration profiles over time in Tests 1 and 2 adjusted to the time scale of Test 1. The vertical line coincides with the start of O <sub>2</sub> delivery to both melts.....	84
Figure 51.	The concentration profiles over time in Tests 3,4, and 6 adjusted to the time scale of Test 3. The vertical line coincides with the start of O <sub>2</sub> delivery to all the melts.....	84
Figure 52.	The concentration profiles over time in Tests 2 and 3 adjusted to the time scale of Test 3. The vertical line coincides with the start of O <sub>2</sub> delivery to both melts.....	85
Figure 53.	The S concentration profiles over time in Tests 8 and 9. The sampling time in Test 8 was adjusted to the time scale of Test 9 when a similar S concentration is observed in both melts.....	87
Figure 54.	The sulfur concentration profile from CS alloy blown with O <sub>2</sub> at 75 cm <sup>3</sup> /min, 500 cm <sup>3</sup> /min and 1000 cm <sup>3</sup> /min and from CNS alloy blown with oxygen at 1000 cm <sup>3</sup> /min, according to Rioux <sup>104</sup> .....	88
Figure 55.	The S concentration profile over time in Test 8 compared to Rioux's testwork with CS alloy blown with oxygen at 75 cm <sup>3</sup> /min. The time scale in Test 8 is adjusted to Rioux's sampling time when a similar S concentration is observed in both melts. The vertical line indicates the start of O <sub>2</sub> blowing at 75 cm <sup>3</sup> /min in Test 8.....	89
<b>Appendix A</b>		
Figure A1.	Qualitative identification of slag components in Test 1 by X-ray diffraction.....	94
Figure A2.	Qualitative identification of ejected material on the quartz reaction vessel in Test 1 by scanning electron microscopy.....	95

**Chapter 2**

Table 1.	Parameters of the experimental system used by Kikuchi <sup>67-70</sup> et al. according to Alyaser <sup>66</sup> .....	21
----------	--	----

**Chapter 3**

Table 2.	Dimensions of the reaction vessel and its accessories.....	46
Table 3.	Average elemental composition of INCO cathode copper sheet.....	52
Table 4.	Composition of HYCOR alumina crucible according to the manufacturer..	54
Table 5.	Elemental determinations for CS and CNS alloys.....	55
Table 6.	Experimental conditions used for desulfurization and oxidation tests .....	57

**Chapter 4**

Table 7.	Tabulated S and O assays from Test 1 conducted at 1498 K by blowing an O <sub>2</sub> -N <sub>2</sub> gas mixture with $\mathcal{F}_{O_2} = 0.62$ at 170.6 cm <sup>3</sup> /min on liquid Cu - 3 wt% S alloy .....	58
Table 8.	Tabulated S and O assays from Test 2 conducted at 1523 K by blowing pure O <sub>2</sub> at 66 cm <sup>3</sup> /min on the surface of liquid CS alloy.....	62
Table 9.	Tabulated S and O assays from Test 3 conducted at 1523 K by blowing pure O <sub>2</sub> at 75 cm <sup>3</sup> /min on the surface of a CS alloy charge .....	65
Table 10.	Tabulated S, O and Ni assays from Test 4 conducted at 1523 K with CNS alloy initially blown with pure O <sub>2</sub> jet at 75 cm <sup>3</sup> /min and then at 372 cm <sup>3</sup> /min.....	68
Table 11.	Tabulated O assays from Test 6 conducted at 1523 K by blowing a pure O <sub>2</sub> jet at 75 cm <sup>3</sup> /min on the surface of a cathode copper .....	71
Table 12.	S and O determinations for Test 7 and Test 8. The time scale in Test 8 has been adjusted to coincide with the sampling time of Test 7 at t = 61 minutes where the S content of both melts is similar.....	74
Table 13.	Tabulated S, O and Ni assays from Test 9 for CNS alloy melted under air and then blown with pure O <sub>2</sub> at 75 cm <sup>3</sup> /min and finally subjected to submerged N <sub>2</sub> injection at 2000 cm <sup>3</sup> /min .....	78

## Abbreviations

<i>atm</i>	<i>atmospheres (multiply by 101325 to attain value in Pa)</i>
<i>CDN</i>	<i>Canadian</i>
<i>cm<sup>3</sup></i>	<i>cubic centimeters</i>
<i>cm<sup>3</sup>/min</i>	<i>cubic centimeters per minute (divide by 6 × 10<sup>7</sup> to attain value m<sup>3</sup>/s)</i>
<i>g</i>	<i>gram</i>
<i>J</i>	<i>joules</i>
<i>K</i>	<i>degrees Kelvin</i>
<i>kg</i>	<i>kilogram</i>
<i>kg-mole</i>	<i>kilogram-mole</i>
<i>kJ</i>	<i>kilojoules</i>
<i>kPa</i>	<i>kilo-Pascals (multiply by 1000 to attain value in Pa)</i>
<i>m</i>	<i>meters</i>
<i>m<sup>3</sup></i>	<i>cubic meters</i>
<i>min</i>	<i>minutes</i>
<i>MPV</i>	<i>Multi-Purpose Vessel</i>
<i>mt</i>	<i>metric tonne</i>
<i>mtpd</i>	<i>metric tonne per day</i>
<i>N</i>	<i>Newtons</i>
<i>Nm<sup>3</sup></i>	<i>normal cubic meters</i>
<i>Nm<sup>3</sup>/hr</i>	<i>normal cubic metres per hour</i>
<i>OFC</i>	<i>Oxygen Flash Converting</i>
<i>Pa</i>	<i>Pascal</i>
<i>s</i>	<i>seconds</i>
<i>Temp</i>	<i>Temperature</i>
<i>vol %</i>	<i>composition in volume percent</i>
<i>wt %</i>	<i>composition in weight percent</i>
<i>X</i>	<i>mole fraction</i>
<i>yr</i>	<i>year</i>

## Chemical Symbols

<i>Al<sub>2</sub>O<sub>3</sub></i>	<i>alumina (aluminum oxide)</i>
<i>CH<sub>4</sub></i>	<i>methane (natural gas)</i>
<i>Co</i>	<i>cobalt</i>
<i>Cu</i>	<i>copper</i>
<i>CuO</i>	<i>copper (II) oxide</i>
<i>Cu<sub>2</sub>O</i>	<i>copper (I) oxide</i>
<i>Cu<sub>2</sub>S</i>	<i>chalcocite</i>
<i>Fe</i>	<i>iron</i>
<i>Ni</i>	<i>nickel</i>
<i>NiO</i>	<i>nickel oxide</i>
<i>N<sub>2</sub></i>	<i>diatomic nitrogen</i>
<i>O, O<sub>2</sub></i>	<i>monatomic oxygen and diatomic oxygen respectively</i>
<i>Si</i>	<i>silicon</i>
<i>SO<sub>2</sub></i>	<i>sulfur dioxide</i>

## Dimensionless Numbers

<i>Fr</i>	<i>Froude</i>
<i>Ma</i>	<i>Marangoni</i>
<i>Re</i>	<i>Reynolds</i>
<i>Sc</i>	<i>Schmidt</i>
<i>Sh</i>	<i>Sherwood</i>

## Superscripts

<i>b</i>	<i>bulk phase</i>
<i>I</i>	<i>interface</i>

## Subscripts

( <i>g</i> )	<i>gas</i>
( <i>l</i> )	<i>liquid</i>
( <i>s</i> )	<i>solid</i>
<i>I, S</i>	<i>reactants I or S</i>

## Symbol

<b>Symbol</b>		<b>S.I. Units</b>	<b>Typical Units</b>
$\alpha$	<i>negative slope of surface tension-solute concentration plot</i>	$(N/m)/(kg\text{-mole}/m^3)$	
$\beta$	<i>negative of gradient of solute concentration across liquid film</i>	$kg\text{-mole}/m^3$	
$\gamma'$	<i>surface activity coefficient</i>	<i>unitless</i>	
$\Delta$	<i>change in quantity</i>	<i>unit dependent</i>	
$\Gamma_i$	<i>surface concentration or adsorption</i>	$kg\text{-mole}/m^2$	
$\theta$	<i>fractional surface coverage by solute</i>	<i>unitless</i>	
$\mu$	<i>gas or liquid viscosity</i>	$kg/m\cdot s$	<i>poise (g/cm/s)</i>
$\mu_B$	<i>chemical potential of reactant B</i>	<i>V</i>	
$\sigma$	<i>surface tension</i>	$N/m$	<i>dyne/cm</i>
$\psi$	<i>electrical potential</i>	<i>V</i>	
<i>a</i>	<i>activity of solute or species</i>	<i>unitless</i>	
$C_r, C_s$	<i>concentration of reactants</i>	$kg\text{-mole}/m^3$	
$\Delta C$	<i>concentration gradient</i>	$kg\text{-mole}/m^3$	
$d_o$	<i>inner diameter of lance</i>	<i>m</i>	<i>mm</i>
$d_c$	<i>diameter of cavity</i>	<i>m</i>	<i>mm</i>
<i>D</i>	<i>diffusivity of solute</i>	$m^2/s$	
$\Delta G^\circ$	<i>standard free energy of formation</i>	$J/kg\text{-mole}$	$kJ/g\text{-mole}, kJ$
<i>g</i>	<i>gravitational constant (9.81 m/s<sup>2</sup>)</i>	$m/s^2$	
$h_b$	<i>depth of bath</i>	<i>m</i>	<i>mm</i>
$H_c$	<i>depth of cavity</i>	<i>m</i>	<i>mm</i>
$H_o$	<i>lance height</i>	<i>m</i>	<i>mm</i>
<i>ID</i>	<i>inner diameter</i>	<i>m</i>	<i>mm</i>
$k_a$	<i>apparent rate constant</i>	<i>dependent on the order of the reaction</i>	

<b>Symbol</b>		<b>S.I. Units</b>	<b>Typical Units</b>
$k_{ov}$	overall mass transfer coefficient	m/s	
$K$	equilibrium adsorption coefficient	unitless	
$M_j$	momentum of gas jet	N	dyne ( $N \times 10^5$ )
$n''$	flux	kg-mole/m <sup>2</sup> /s	g/m <sup>2</sup> /s
$P$	pressure	Pa	atm, kPa
$\mathcal{P}$	partial pressure	Pa	atm
$R$	universal gas constant (8.314 J/mole/K)	J/kg-mole/K	J/g-mole/K
$r_b$	radius of bath	m	mm
$r_s$	radius of reaction area	m	mm
$S$	spreading coefficient	N/m	dyne/cm
$T$	temperature	K	°C
$u_a$	axial gas velocity	m/s	cm/s
$u_c$	gas flowrate at lance outlet	m <sup>3</sup> /s	cm <sup>3</sup> /s, cm <sup>3</sup> /min
$X$	mole fraction	unitless	
$[X]$	dissolved species	kg-mole/m <sup>3</sup>	
$[X]_{Cu}$	dissolved species in copper	kg-mole/m <sup>3</sup>	
$[X]_{ads}$	adsorbed species on liquid surface	kg-mole/m <sup>3</sup>	

INCO's Copper-Cliff Smelter in Sudbury, Ontario is a leading non-ferrous metals producer with annual yields of 120,000 mt of copper and 115,000 mt of nickel. Over the decades, the production flowsheet at the smelter has been modified continuously in response to technological developments, economic demands and increased environmental awareness<sup>1,2</sup>. These factors combined led to a decrease in sulfur dioxide (SO<sub>2</sub>) emissions at the smelter from 2,000,000 mt/yr to 685,000 mt/yr between 1970 and 1985. In the mid 1980's, the Ontario Ministry of the Environment initiated the "Countdown Acid Rain"<sup>3</sup> program which required INCO to further reduce sulfur dioxide emissions to 265,000 mt/year by 1994. INCO responded to its new environmental obligations at Sudbury with the "SO<sub>2</sub> Abatement Project"<sup>4</sup>. At a capital cost of CDN\$540,000,000, the project was designed to lower SO<sub>2</sub> emissions by the target date, increase the efficiency of INCO's manpower and energy resources, reduce smelter operating costs, improve the converter workplace environment and affect these changes without diminishing productivity<sup>5,6</sup>. Meeting these goals involved substantial changes to the smelting and copper production circuits. Smelting practice was improved with existing INCO flash furnace technology and through consolidation of INCO's mill resources while copper smelting and converting was enhanced with technology borrowed from the ferrous industry i.e., melt stirring via bottom injection of inert gas through porous plugs.

The purpose of this study is to examine copper converting practice at the Copper Cliff Smelter and investigate the factors affecting the kinetics of desulfurization in the finishing stages of blister copper production. To better understand the metallurgy of INCO's converting practice, it is instructive to examine the smelter circuit in some detail and the major changes to the flowsheet between 1992 and 1993<sup>†</sup>.

### ***1.1 The Smelter Flowsheet in 1992***

In 1992, the smelter complex operated individual nickel (Ni) and copper (Cu) circuits (see Figure 1) which processed 2800 mtpd of nickel concentrate at 11-12 wt% Ni, 2-3 wt% Cu, and 1000 mtpd of copper concentrate at 28-30 wt% Cu, 0.8-1.0 wt% Ni<sup>1,2</sup>. Nickel

---

<sup>†</sup> The evolution of the smelter flowsheet prior to the period 1992-1993 is documented in the references cited<sup>1,2</sup>.

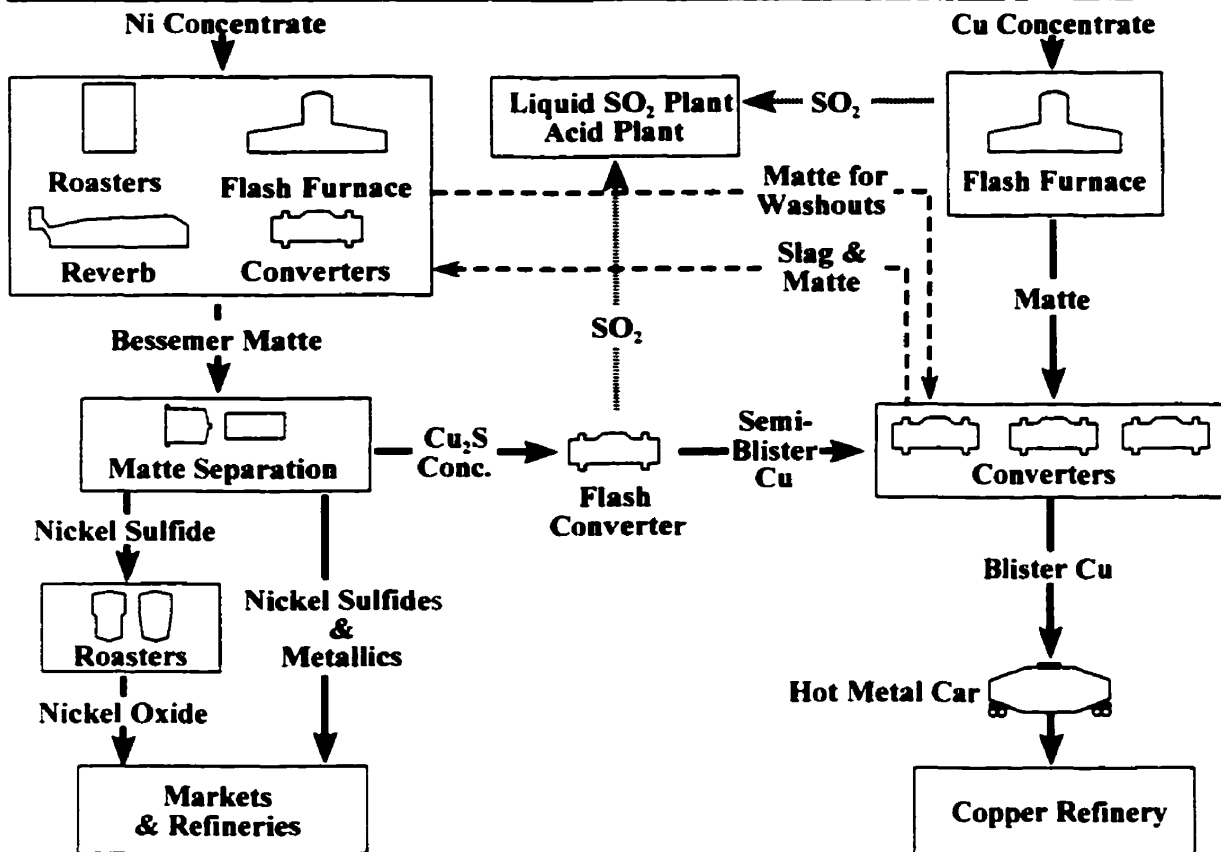


Figure 1. The Copper Cliff Smelter flowsheet in 1992 operating separate nickel and copper production circuits<sup>2</sup>.

concentrate was either flash smelted in the INCO flash furnace or was partially oxidized in multiple hearth roasters and then smelted in oxygen-fuel fired reverberatory furnaces to produce a matte of 30-35 wt% CuNiCo<sup>+</sup>. Furnace mattes were blown with air in Pierce Smith (PS) converters for partial sulfur elimination and almost complete iron removal, through oxidation and slagging, producing a sulfur deficient nickel-copper white metal, or “Bessemer matte”, containing 75 wt% Cu-Ni and 22 wt% S. Converter slags were reverted to the reverberatory furnaces for cleaning and disposal while the Bessemer matte was sent for further processing.

Cu-Ni matte was cast into molds in the matte processing plant and slow cooled to promote the segregation of its constituent phases into grains of copper sulfide and Cu-Ni alloy within a matrix of nickel sulfide<sup>7</sup>. Solidification of the matte into physically and chemically distinct phases allowed for its crushing, grinding and separation into concentrates

<sup>+</sup> Prior to 1992 nickel concentrate was processed solely by reverberatory smelting<sup>1,2</sup>

of nickel sulfide, copper sulfide and a Ni-Cu alloy containing precious metals. The nickel products underwent further roasting/refining procedures while the copper fraction, a nickel bearing chalcocite (6-7 wt% Ni), was sent to the copper smelter for oxygen flash converting to semi-blister copper.

In the copper production circuit, concentrate from ore flotation was oxygen flash smelted to matte at 45-50 wt% CuNiCo. Both matte and semi-blister were blown to blister copper in PS converters and then transferred via hot metal cars to the copper refinery where the metal was cast, solidified and subsequently electro-refined to cathode copper.

INCO strategy's to meet production and environmental goals called for fewer SO<sub>2</sub> emission sources, elimination of process redundancy and inefficiency, intensification of process rates and improvements in copper smelting and converting practice<sup>1,2,4,5,6</sup>. Sulfur containment in 1992 was achieved principally through the rejection of pyrrhotite to the mill tailings during mineral processing of the mined ore. At the nickel smelter, large volumes of weak SO<sub>2</sub> gas streams were generated by the Herreshoff roasters, reverberatory furnaces and nickel converters. Process redundancy was identified in the practice of separating copper and nickel during ore beneficiation and at the matte separation stage while production limits were imposed on both metals production circuits due to the processing of nickel in the copper circuit. The presence of nickel in copper matte from flash smelting and in semi-blister copper from flash converting introduced a number of metallurgical challenges to converting practice<sup>8</sup>. During the finishing blows to blister, excessive oxidation of nickel and copper near the tuyere line of the PS converters resulted in the formation of a solid oxide or 'mush' that separated by gravity to the melt surface. Accumulation of 'mush' between successive converter cycles reduced the production capacity of the converters while accretions of the refractory oxides on the tuyere line interfered with punching procedures and air flow as shown by Bustos et al<sup>9</sup>. Matte from the nickel smelter was periodically transferred to the copper converters to 'washout' i.e. reduce the accrued oxides of nickel and iron, into a Cu-Ni matte and a fluid slag which were recycled to the nickel smelter. Ferro-silicon additions were made to every third or fourth washout to create stronger reducing conditions and affect a more thorough removal of the oxides.

Washout procedures highlighted important deficiencies in smelter practice. Reduction of the slag by the iron sulfide in the matte released sulfur dioxide into the workplace environment while asynchronous production schedules in copper converting and nickel smelting delayed transfers of nickel matte to the copper converters and recycling of washout products to the nickel furnaces and converters. These recycles were an encumbrance to the nickel circuit because the large transfers of copper upset the metallurgical chemistry of nickel production.

**1.2 The Smelter Flowsheet in 1993**

The process and equipment modifications made by 1993 resulted in the smelter flowsheet shown in Figure 2<sup>1,2,10,11</sup>. Implementation of new production methods has allowed INCO to maintain production levels of copper and nickel, resolve its metallurgical problems in copper production and meet target SO<sub>2</sub> emissions.

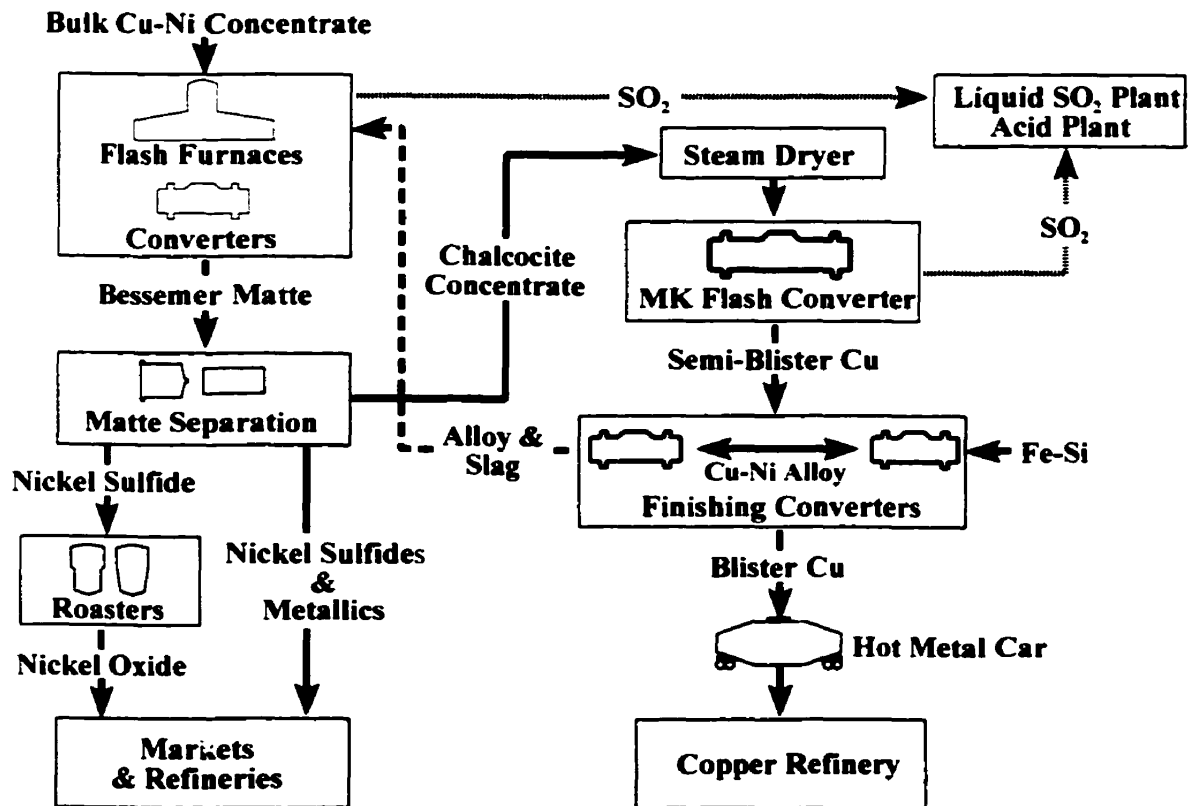


**Figure 2. The current Copper Cliff Smelter flowsheet after implementation of process and equipment modifications in 1993<sup>2</sup>.**

Rationalization of INCO's mill resources under the "SO<sub>2</sub> Abatement Project" has simplified ore processing to produce a bulk copper-nickel concentrate. Oxygen flash smelting of the mill concentrate yields a matte at 45-50 wt% CuNiCo which is transferred to PS converters and blown with air to a Bessemer matte. Preliminary cooling of the Bessemer matte is conducted in the converters with nitrogen injected through the tuyere line. Cooled matte is transferred to the matte processing plant where all Cu-Ni separation takes place after matte solidification and segregation into its constituent phases via comminution, magnetic separation and column flotation. The products of matte separation are metallic Cu-Ni alloy, and concentrates of nickel sulfide and copper sulfide. Nickel products are sent for further refining whereas the chalcocite (MK) concentrate, now the sole feed for copper production, is steam dried and then flash converted to semi-blister copper in the recently developed MK flash reactor. The use of column flotation during matte separation has decreased the nickel content in the MK concentrate from 6-7 wt % Ni to 3-4 wt% Ni and consequently has reduced the amount of metals recycle to the smelter furnaces. Finishing of semi-blister to blister is performed, in modified PS converters, by oxygen top-blowing and enhanced by bottom stirring of the melt with nitrogen. The high strength, low volume, SO<sub>2</sub> gas streams from the flash furnace and flash converter are directed to the SO<sub>2</sub> plant for sulfur fixation while the development of sulfur-free washouts using Cu-Ni alloy and ferrosilicon have largely eliminated fugitive SO<sub>2</sub> emissions from the finishing stages. The new washout procedures have the added benefits of not being dependent on matte from the smelting furnaces and the recycled washout products are more amenable to processing in the bulk smelting and Bessemer converting units.

### ***1.3 Blister Copper Production from MK Concentrate***

#### ***1.3.1 Oxygen Flash Converting of MK Concentrate to Semi-Blister***

INCO's experimentation with oxygen flash converting (OFC) began in 1947 as an extension to its flash furnace research program for primary smelting of sulfides<sup>12</sup>. Initial OFC trials on comminuted MK concentrate without flux additives produced molten copper

in addition to various oxides of nickel, copper and iron. Significant nickel oxidation observed in these experiments presented a metallurgical barrier against commercial application of OFC to MK concentrate at the time. OFC testwork renewed at INCO's research facilities in the late 1970's and early 1980's successfully smelted concentrates with mineralogical and chemical compositions ranging from pure chalcopyrite to chalcocite<sup>12,13,14</sup>. An important result of these experiments was that nickel oxidation could be minimized by practicing OFC at high temperature and recovering all the nickel in sulfur saturated copper or semi-blister.

Commercial scale OFC of MK concentrate was implemented at Copper Cliff in 1985 using modified PS converters to process 250 mtpd of wet chalcocite cakes, at 74 wt% Cu, 4.2 wt% Ni, and 21 wt% S into semi-blister copper at 2-3 wt% S and 4-6% Ni. NiO formation and large temperature fluctuations were controlled by maintaining 8% moisture in the filter cakes and adjusting the oxygen/filter cake ratio accordingly. Desulfurization of semi-blister to blister in PS converters by submerged air injection via tuyeres yielded blister copper at 100 ppm S and < 1% Ni.

The desire to increase energy efficiency and intensify process rates under the "SO<sub>2</sub> Abatement Project" resulted in a new drying procedure for the MK concentrate and the development of a new flash procedure and a flash reactor with a greater production capacity<sup>10,14</sup>. Current practice is to dry 725 mtpd of fine nickel containing chalcocite to < 0.2% moisture in a Myren multi-coil stream dryer operated at 483 K. The dried concentrate is fed through two burners near each endwall of the MK flash reactor, a cylindrical vessel 18 m in length by 4.5 m in diameter, and flash converted to produce semi-blister and a high strength SO<sub>2</sub> gas stream. Nitrogen sparging of the melt, via porous plugs on the reactor bottom, enhances mixing conditions and allows for oxygen utilization efficiencies of up to 90%. The semi-blister, a mixture of white metal and metallic copper, with an aggregated S content of 2-3 wt% S and 3-5 wt% Ni, is transferred to the Multi-Purpose Vessel (MPV) for further desulfurization to blister while the SO<sub>2</sub> gas stream is directed to the acid plant for fixation to sulfuric acid.

### ***1.3.2 Finishing of Semi-Blister to Blister***

Although nickel oxidation was controlled during OFC it persisted in the finishing procedures of 1992. Oxide production and accumulation in the converters were attributed to the variable mixing conditions generated in the melt from submerged air injection via tuyeres<sup>11</sup>. In the vicinity of the tuyere line the injected air oxidized substantial quantities of nickel and copper and only provided adequate agitation of the melt in this region<sup>15,16,17,18</sup>. Under these mixing conditions the oxides could not be redigested sufficiently into the melt and either separated out to the melt surface due to density differences or accreted on the tuyeres and other converter surfaces. The use of air as the oxidizing gas also limited the amount of sensible heat available for melting anode scrap.

Thermodynamic analyses of the ternary Cu-Ni-S and Cu-Ni-O systems by INCO<sup>19</sup> indicated that under equilibrium conditions it was possible to selectively remove sulfur as SO<sub>2</sub> with minimal nickel oxidation and subsequently separate nickel from the melt as NiO without significant copper oxidation<sup>11</sup>. INCO's pilot testwork on semi-blister melts top-blown with oxygen and bottom stirred with nitrogen via a porous plug produced blister copper at near chemical equilibrium<sup>11</sup>. Concurrent washout experiments developed a new procedure using a Cu-Ni-Fe-Si alloy, with a Cu:Ni weight ratio of 3-4, to reduce oxide accretions into a Cu-Ni alloy of the same Cu:Ni ratio as the washout medium, and a fayalite slag containing 1 wt% Ni and 0.5 wt% Cu.

Industrial application of these procedures depended on vessels that could provide uniform agitation of the melt and uninterrupted oxygen delivery. These requirements were satisfied by the INCO MPV (see Figure 3), a tuyereless PS converter, 10.7 m in length by 4 m in diameter, retrofitted with an oxygen lance in each endwall and five porous plugs\* with a preset permeability to nitrogen in the reactor bottom. Natural gas burners coupled to the oxygen lances are fired during washouts to create reducing conditions and sustain the reaction temperature at 1573 K. Two MPVs are operated at all times and alternate between processing semi-blister or holding Cu-Ni alloy at temperature in preparation for later use in washouts.

---

\* A later modification to the MPV increased the number of porous plugs from five to six<sup>12</sup>.

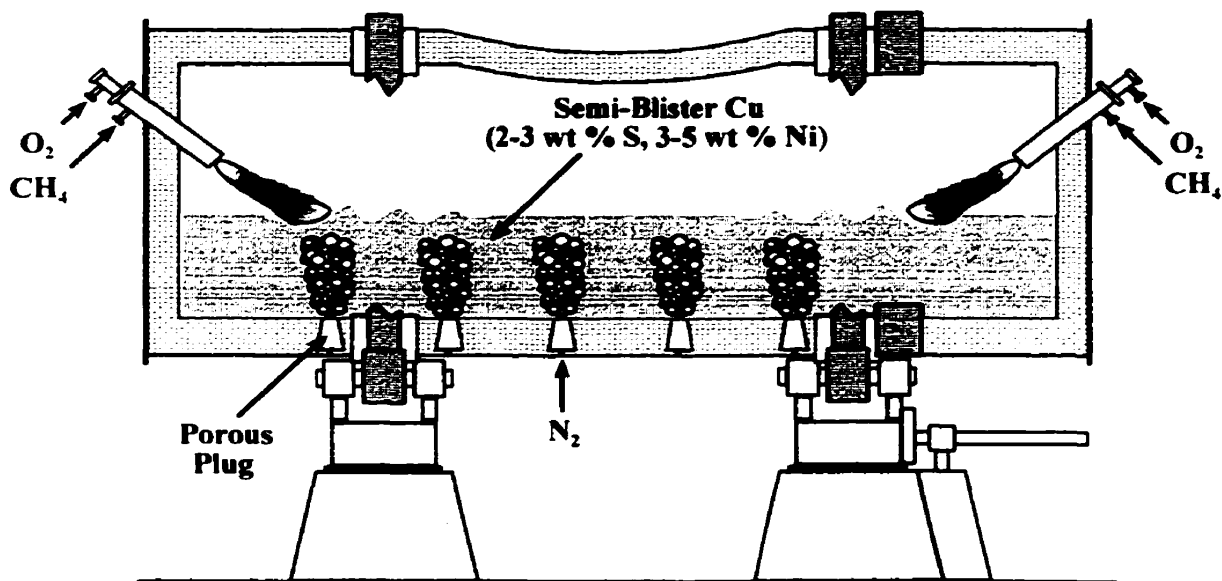


Figure 3. The INCO Multi-purpose vessel (MPV) for finishing of semi-blister to blister<sup>1</sup>.

Desulfurization is performed by top-blowing oxygen at  $5300 \text{ Nm}^3/\text{hr}$  while the melt is stirred with nitrogen injected at a rate of  $14 \text{ Nm}^3/\text{hr}/\text{plug}$ . Tonnage oxygen, utilized near 85% efficiency, also provides excess heat for melting cold anode scrap. Disposable oxygen probes monitor the oxidation state of the melt to determine the endpoint of blowing and prevent overoxidation of the molten copper charge. Bottom stirring with nitrogen enhances the process kinetics by providing uniform mixing conditions in the bath. This method of agitation was borrowed from the ferrous industry where it is applied to ladle refining procedures to accelerate thermal and chemical homogenization of the melt and the kinetics of the refining reactions<sup>11</sup>. INCO's adaptation of bottom stirring to copper smelting and converting represents the first application of this technology to commercial copper production<sup>10,11</sup>.

The MPV converts 135 mt of semi-blister at 2-3 wt% S, 3-5 wt% Ni into blister at 0.6 wt% Ni, 70 ppm S, and 1 wt% O at temperatures between 1493 K and 1573 K. About 25 mt of copper scrap is also added into the reactor during the converting procedure. Sulfur

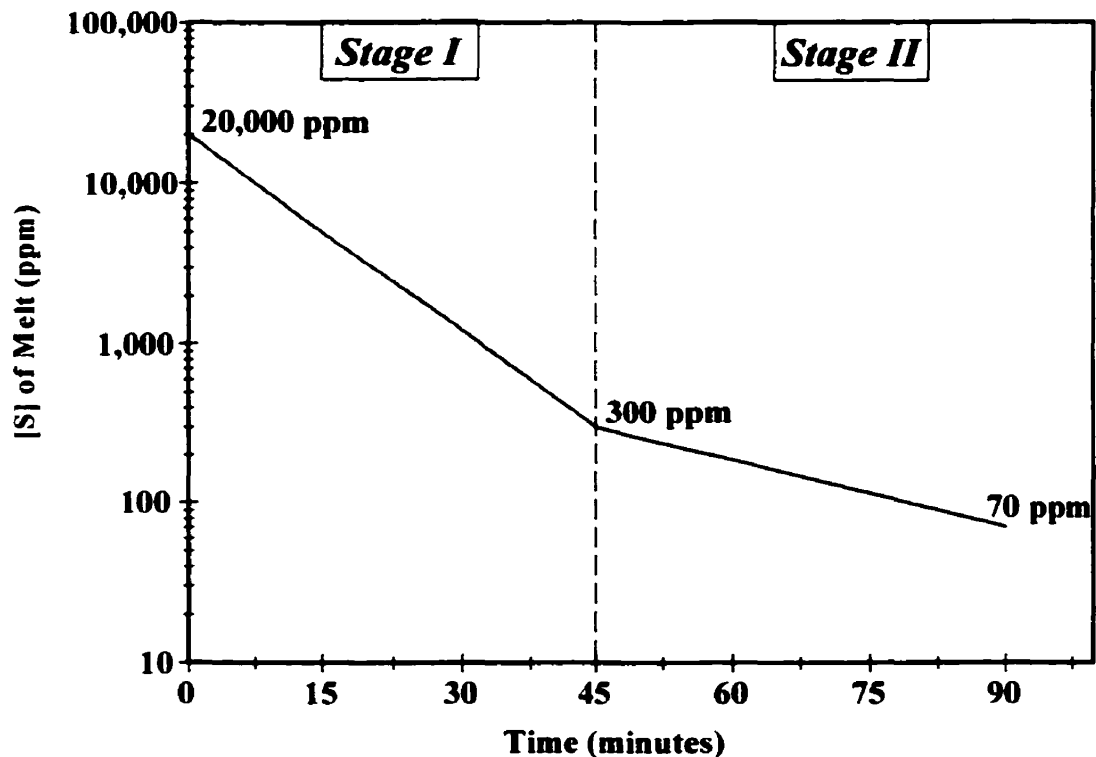


Figure 4. Process curve of sulfur for the INCO MPV<sup>19,20</sup>. Stage I sulfur elimination is performed by oxygen top-blowing and enhanced by nitrogen stirring. In Stage II, oxygen injection is terminated while nitrogen agitation of the melt is continued.

elimination from roughly 2 wt% S to 70 ppm S, occurs in two stages (see Figure 4) of approximately equal process time; the second stage having a lower rate of desulfurization<sup>19,20</sup>. A change in the rate of sulfur elimination is observed to occur at a sulfur content of 300 ppm which corresponds to oxygen saturation (roughly 1 wt% O) and partial oxidation of the nickel values in the melt. Industrial practice is to terminate the oxygen top blowing at 300 ppm S in the belief that the oxygen dissolved in the melt is more than sufficient to oxidize the remaining sulfur. Nitrogen bottom blowing through porous plugs is continued at that same rate during the second stage of finishing. At the end of two finishing cycles, 150 t of washout alloy with a Cu:Ni ratio of 3 is transferred from the holding MPV to the finishing MPV along with 15 mt of 15 wt% Si ferro-silicon. The oxy-fuel burners are fired at 70%

stoichiometric oxygen to maintain the process temperature at 1573K and create a reducing atmosphere that minimizes alloy oxidation. The reduction process is assisted by nitrogen injection into the bath and produces slag and excess alloy which are bled to the bulk smelting circuit.

### ***1.4 Research Objectives***

A project was commissioned at McGill University in 1993 by INCO as part of an effort to improve the process kinetics in second stage converting. Its purpose was to determine if sulfur elimination is impeded by the formation of oxide impurities such as NiO since this species is thermodynamically stable at oxygen saturation and at the concentration of the impurity encountered industrially. The role of surface phenomena, such as the Marangoni effect, during desulfurization was also to be examined given the presence of two surface active agents i.e. S and O in the melt.

The influence of nickel on desulfurization kinetics was to be evaluated by comparing the rates of sulfur elimination in copper-sulfur melts both in the presence and absence of Ni in the bath. Surface phenomena were to be examined under quiescent melt conditions in order to facilitate their observation and also provide an indirect evaluation of bath mixing to desulfurization kinetics.

Copper extraction from sulfide concentrates encompasses pyrometallurgical procedures such as reverberatory smelting, INCO and Outokumpu flash smelting, the Isasmelt top-blown process, the Vanyukov bath smelting process and the Noranda and Mitsubishi continuous processes. These production methods are differentiated by the shape and size of the reactors, the delivery mechanism of concentrate, flux, reverts, recycle slag and of air/oxygen mixtures to the melt during smelting and converting, the ancillary operations applied after each process stage to recover valuable by-products, and in copper refining procedures. Continuous copper production is further distinguished by the combination of several process stages into one.

In spite of the number of production routes copper pyrometallurgy is basically separated into three process stages: smelting, converting and refining. Industrial interest to optimize these stages has generated studies regarding the kinetics, thermodynamics and thermochemistry of copper extraction. Kinetic studies relevant to the present investigation are those involving the oxidation of copper matte and copper-sulfur alloys by top-blowing of oxygen-inert gas mixtures while submerged gas injection and vacuum refining procedures are also considered here. The role of surface active elements and other surface phenomena on reaction rates are also examined from the perspective of the Cu-S-O, Cu-Ni-S and Cu-Ni-O systems.

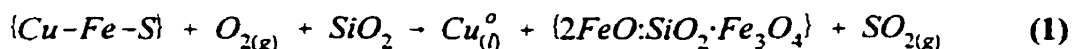
## ***2.1 Thermodynamics and Thermochemistry of Copper Converting***

INCO's finishing procedure resembles the final part of the copper making stage of most converting operations and therefore a brief review of conventional copper converting is presented below to highlight the thermochemical considerations of the INCO process.

### ***2.1.1 Conventional Copper Converting***

Copper converting is usually regarded as the production of impure metallic or 'blister' copper by the sequential oxidation of iron sulfide and copper sulfide in smelter matte. This procedure is most often performed in a Pierce-Smith converter (4 m ID × 9-11

m length) by submerged injection of air or oxygen-enriched air (23-26 vol. % O<sub>2</sub>) into the melt at 500-700 Nm<sup>3</sup>/minute through water cooled tuyeres spanning the inner length of the reactor. A typical converter cycle processes 200-500 mt of matte at 1473 K and produces 100-200 mt of blister copper with by-products of iron-silicate slag and effluent gas bearing sulfur dioxide as summarized by the unbalanced reaction<sup>21</sup>:



The matte is converted in two distinct stages made autogenous by the exothermic oxidation of its sulfide components of which the thermodynamics and phase relationships have been detailed elsewhere<sup>22-30</sup>. In the initial *slag-forming* stage iron sulfides are oxidized to FeO, Fe<sub>3</sub>O<sub>4</sub> and SO<sub>2</sub> while silica flux is added in with the iron oxides to increase their fluidity and hence facilitate their removal during slag tapping procedures. The impure Cu<sub>2</sub>S or ‘white metal’ end product is subsequently oxidized in the *copper-making* stage to blister copper by the overall reaction<sup>21</sup>:



The phase relations of copper-making are described by the ternary Cu-S-O system yet a simplified representation of Cu<sub>2</sub>S oxidation to blister copper can be made with the binary Cu-S phase diagram (Figure 5). The initial oxidation of Cu<sub>2</sub>S (Point A) produces SO<sub>2</sub> and a sulfur deficient white metal containing 19.7 wt% S by the reaction<sup>21</sup>:



When the melt composition reaches the Cu-Cu<sub>2</sub>S miscibility gap (Point B) a blister copper phase containing 1 wt% S is produced which increases in proportion to the white metal with continued melt oxidation. Beyond this immiscibility region (Point C) sulfur exists only as a dissolved species in blister copper and its continued removal takes place by its reaction with dissolved oxygen (Equation (4))<sup>31</sup>. The relationship between the activity of sulfur and

---

<sup>31</sup>ΔG° for Cu<sub>2</sub>S oxidation was derived from a linear regression of the thermodynamic values obtained between 1403 K and 2000 K using Outokumpu’s HSC Chemistry Version 1.10 thermodynamic software.

oxygen is one that is mutually inversed and therefore at the endpoint of converting (Point D) the blister copper contains 0.001-0.03 wt% S and 0.1-0.8 wt %O. Although further desulfurization may take place with continued blowing the procedure is terminated to prevent copper oxide formation by Equation (5)<sup>31</sup>.

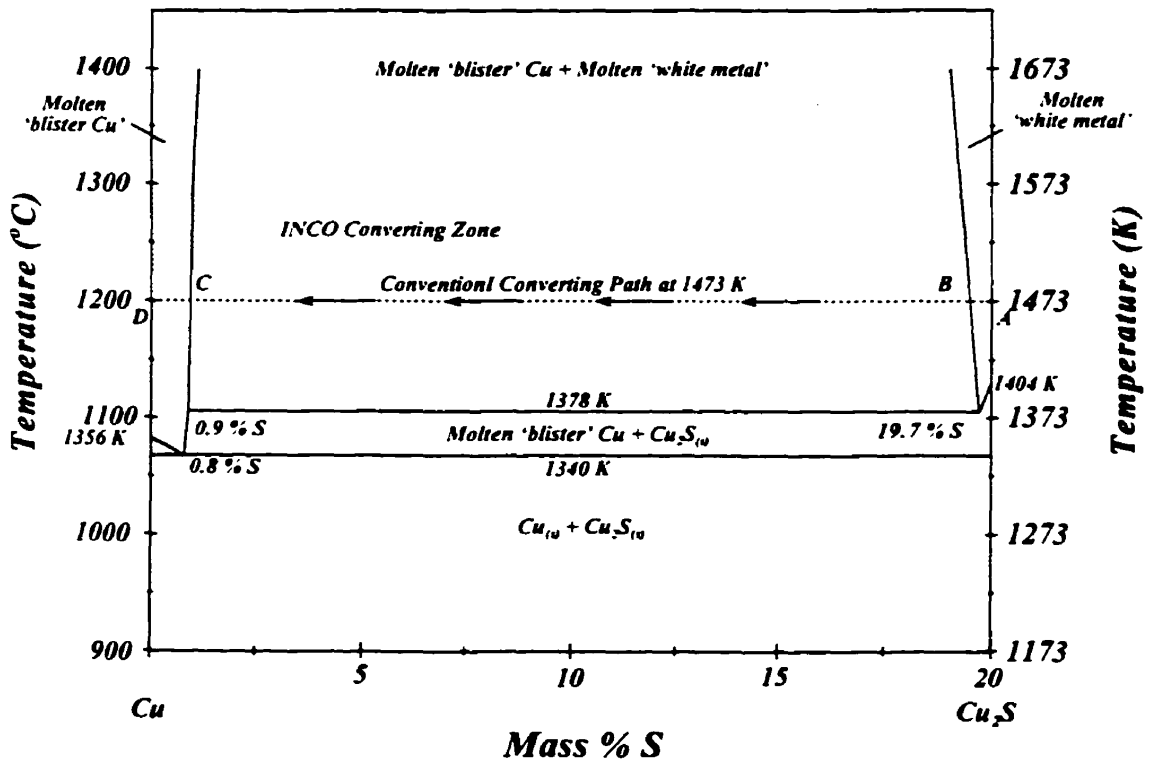
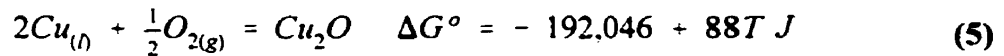
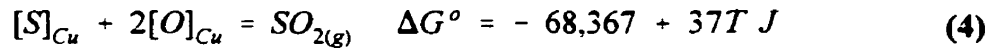


Figure 5. The Cu-S phase diagram showing the oxidation path of Cu<sub>2</sub>S to blister Cu during conventional converting according to Biswas and Davenport<sup>31</sup>. The shaded region depicts the operating zone of the INCO finishing procedure.

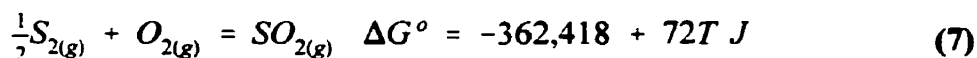
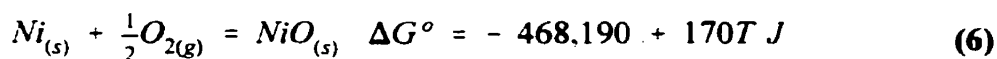
### 2.1.2 Copper Converting at INCO

As mentioned in Chapter 1, INCO processes a sulfur-saturated copper melt (~ 2 wt% S) or 'semi-blister' containing significant nickel values (~ 4 wt % Ni) into blister copper (100 ppm S, 0.6 wt% Ni) at 1523 K - 1573 K in a two stage procedure in which the first is

operated with oxygen top-blowing and nitrogen stirring of the melt and the second with only stirring of the bath by injected nitrogen. The procedure was developed on the basis of a thermodynamic analysis conducted by INCO<sup>19</sup> which sought to minimize ‘mush’<sup>†</sup> formation and maintain nickel levels in the final blister product within acceptable tolerances for subsequent copper electro-refining. It was found that under equilibrium conditions, sulfur can be removed from semi-blister at elevated temperatures by oxidation to SO<sub>2</sub> with minimal nickel oxidation and significant oxygen dissolution in the melt. Upon cooling, the dissolved oxygen reacts with dissolved nickel to form NiO which separates from the melt with minimal copper oxidation and/or entrainment and thus lowers the nickel concentration of the melt to desirable levels.

The relevant thermodynamic information relating to conversion of semi-blister can be obtained from published literature on the Cu-Ni-S<sup>32-35</sup> and Cu-Ni-O systems<sup>36-38</sup>. Larrain and Lee<sup>32</sup> calculated the phase relationships and isoactivity lines for Ni and S in the Cu-Ni-S system which were largely corroborated by Chuang and Chang<sup>35</sup> and are shown superimposed for the copper-rich region at 1473 K in Figure 6. Taskinen’s<sup>36</sup> compilation of various isotherms in the Cu-Ni-O system in addition to Kuxmann and Riecke’s<sup>38</sup> data are presented in Figure 7 which reveal the strong temperature dependence of O and Ni solubilities in copper.

INCO determined the degree of Ni and S oxidation in the copper rich region of the phase diagram by combining the activity data from the Cu-Ni-S diagram with the free energies of formation<sup>31</sup> of NiO and SO<sub>2</sub>:




---

<sup>†</sup> ‘Mush’ in the INCO vernacular refers to a dry slag layer/dross consisting of copper oxides and nickel oxides that is formed during conversion of semi-blister.

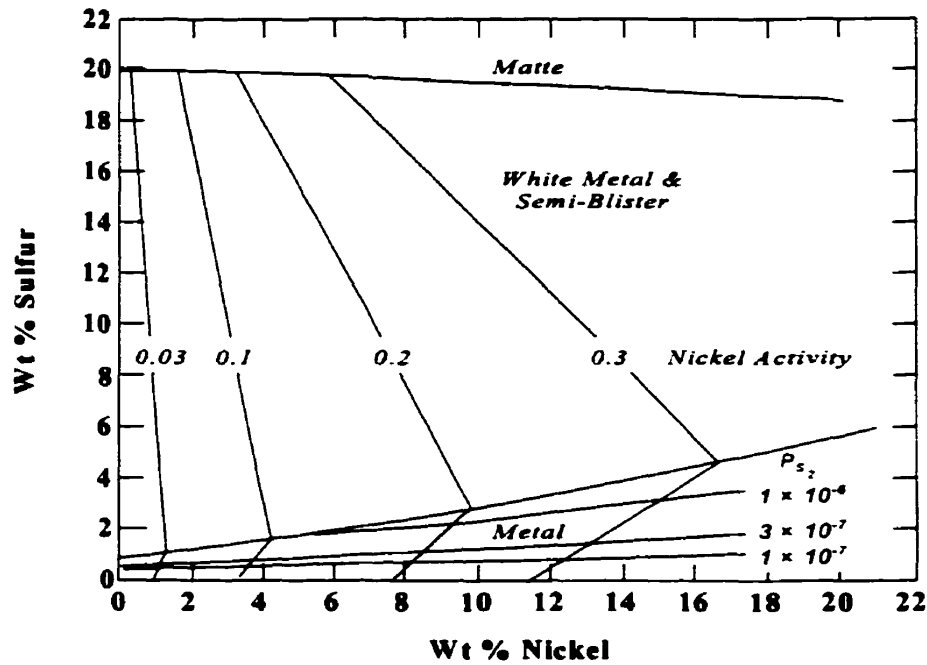


Figure 6. The phase relations of the copper-rich region of the Cu-Ni-S phase diagram at 1473 K shown superimposed on the isoactivity line of Ni and S according to Larrain and Lee<sup>19,32</sup>.

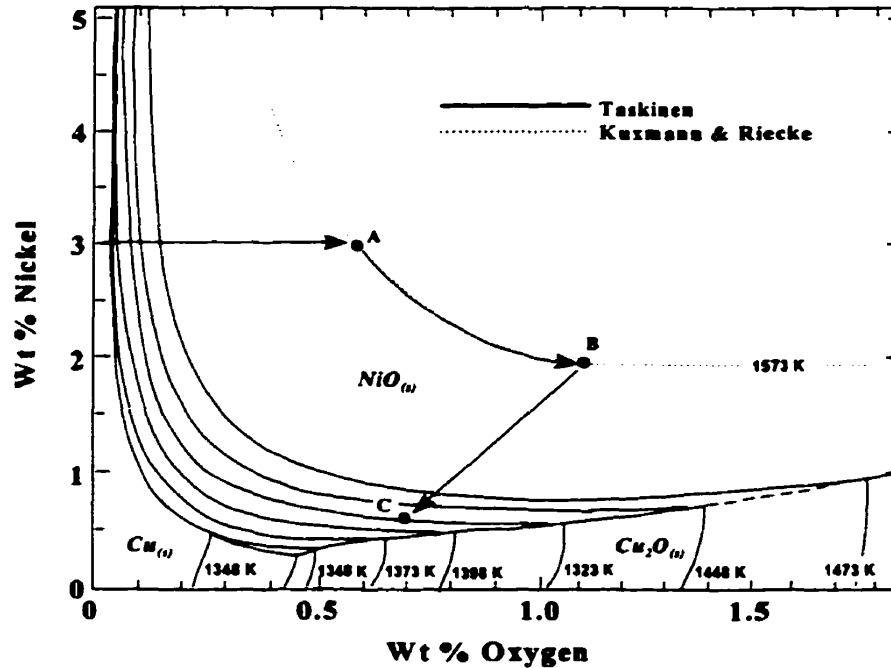


Figure 7. The phase relations and various isotherms of the copper-rich corner of the Cu-Ni-O system according to Taskinen<sup>36</sup> and Kuxmann and Riecke<sup>38</sup>. The arrows trace the oxidation path followed by nickel during the INCO finishing procedure<sup>19</sup>.

If  $P_{\text{SO}_2}$  is assumed to be 0.20 atm ( $2 \times 10^4$  Pa) while  $P_{\text{S}_2}$  and  $P_{\text{O}_2}$  are the equilibrium partial pressures of sulfur and oxygen, then the sulfur content of a semi-blister melt at 1473 K can be reduced to below 0.2 wt % before  $P_{\text{O}_2}$  becomes sufficiently high to cause NiO formation<sup>19</sup>. The Cu-Ni-O diagram shows that sulfur-free copper at 1573 K containing 3 wt % Ni can dissolve upto 0.6 wt % oxygen (Point A) before any nickel oxidation takes place. Continued oxygen dissolution at 1573 K increases the oxygen content and decreases the nickel content of the copper. At point B the dissolved oxygen content of the copper reaches 1.1 wt% which is sufficient to lower the nickel content of the melt to 0.6 wt %, without oxidizing copper, by cooling the melt to the casting temperature of 1423 K<sup>19</sup>.

The composition and temperature profiles of the melt from a pilot plant test of the finishing procedure are shown in Figure 8. A holding period of 30 minutes was incorporated into the INCO conversion technique to approach equilibrium because early test results indicated that some copper had oxidized in spite of vigorous melt stirring with nitrogen. Cooling the charge to the casting temperature of 1423 K was accomplished by adding cold anode scrap to the melt which was found to be more rapid than natural cooling and did not affect the elimination of nickel as NiO.

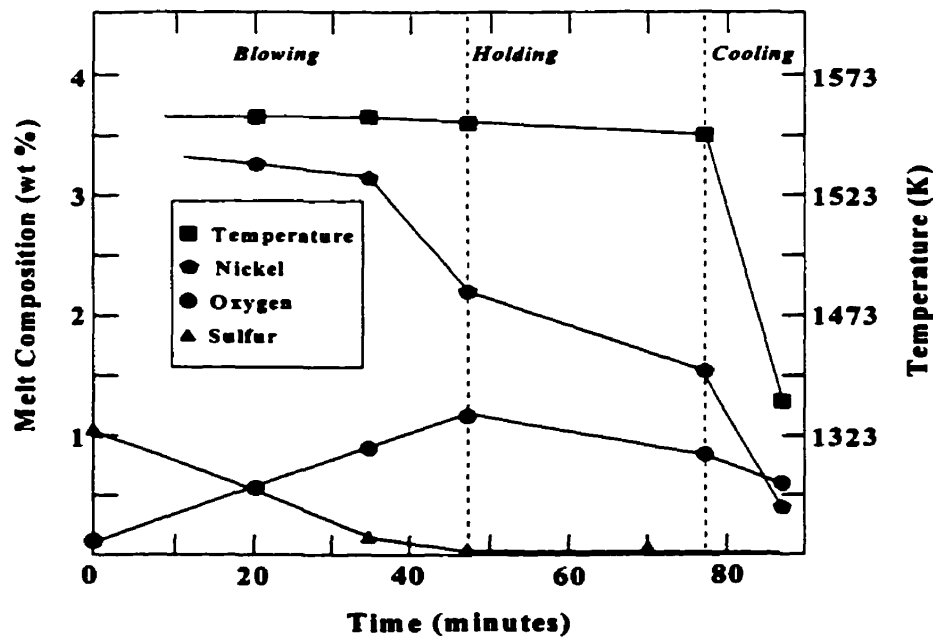


Figure 8. The composition and temperature changes experienced by the copper charge during a pilot plant test of the INCO finishing procedure<sup>19</sup>.

**2.2 Gas-Liquid Interactions**

A rate process involving two immiscible phases which are not in chemical equilibrium with each and are brought into contact can be regarded as the following series of mass transport and chemical reaction steps between the reactant species of each phase<sup>39,40</sup>:

- 1) Diffusion of the reactant species from the bulk of their respective phases and through a boundary layer to a gas-liquid or liquid-liquid interface.
- 2) Chemical reaction at the interface which includes absorption, adsorption, dissociation or activated complex formation.
- 3) Diffusion of the initial reactants and/or reactant products away from the interface.

The sum of the three steps determines the overall rate of reaction while the step providing the most resistance is considered to be rate controlling. In higher temperature processes, where near chemical equilibrium exists at the reaction interface, diffusion of a reactant in the liquid and/or gas phase is often the rate limiting step while in lower temperature systems the chemical reaction may exercise all or joint control over the process rate.

Mass transfer rates between two fluid phases such as in gas-liquid metal systems depends on the physical properties of the phases, on dynamic conditions in the reaction system and on the concentration driving force that is equivalent to the difference between the equilibrium concentration and effective bulk concentration of the bulk liquid<sup>41</sup>. A reactant gas species may contact a liquid metal either by diffusion through a stagnant gas phase or by convection when it is part of a laminar or turbulent gas jet that is either blown onto the liquid metal surface or is injected into the melt.

The mass flux of any system can be related generally to the kinetic and thermodynamic influences of the system according to the following equation:

$$n'' = k_{ov} \Delta C \quad (8)$$

here  $n''$  is the mass or molar flux per unit area,  $k_{ov}$  is the overall mass transfer coefficient and

$\Delta C$  is the concentration driving force in the liquid phase. Although useful kinetic data can be derived from diffusion controlled studies, industrial pyrometallurgical procedures usually involve convective contact between the gas phase and the melt. Ferrous and non-ferrous processes both make use of submerged injection and top-blown procedures of which the physical behaviour of the injected gas and the flow regimes established in these reactors have been modelled at low temperature<sup>42-55</sup>. Combining this information with available thermochemical data can yield mass transport relationships defined in terms of dimensionless groups which consider the transport, dynamic and geometric properties of the system<sup>41,57-64</sup>.

In top-blown systems the gas jet impinging on the liquid may experience starvation of its reactant species. When this condition arises the mean gas pressure in the bulk gas above the liquid surface is reduced to a value less than the pressure in the jet. Therefore, analysis of kinetic data must recognize whether starvation has occurred otherwise mass transfer coefficients may become unreliable<sup>57</sup>.

### **2.2.1 Top Blown Gas Injection with High Momentum Jets**

Gas impingement on a liquid can generate several modes of flow between the phases depending on the gas velocity and the angle and position of the lance above the liquid surface. Molloy<sup>43</sup> identified three main modes according to the observed surface effects: dimpling, splashing and penetrating which are depicted in Figure 9 and show the change in shape of the surface depression from a parabola or semi-circle to a U-shape with increasing jet momentum<sup>42</sup>. A low jet velocity or large lance height between the liquid and impinging gas creates a *dimple* or slight depression on the liquid surface (Figure 9(a)). Increasing the gas momentum by reducing the lance height or increasing the gas velocity leads to a critical depth of depression which if exceeded results in the entrainment of liquid in the surface indent followed by its outward ejection signalling the start of *splashing* (Figure 9(b)). Further increases in gas momentum eventually results in deeper *penetration* of the liquid phase by the gas stream which is accompanied by a reduction in the volume of ejected material (Figure 9(c)). Two consequences of increased jet momentum account for this

behaviour: an increased proportion of the gas jet is reflected back into itself while the remaining portion of the reflected gas not entrained in the incoming jet follows a longer trajectory along the periphery or lip of the depression<sup>42</sup>.

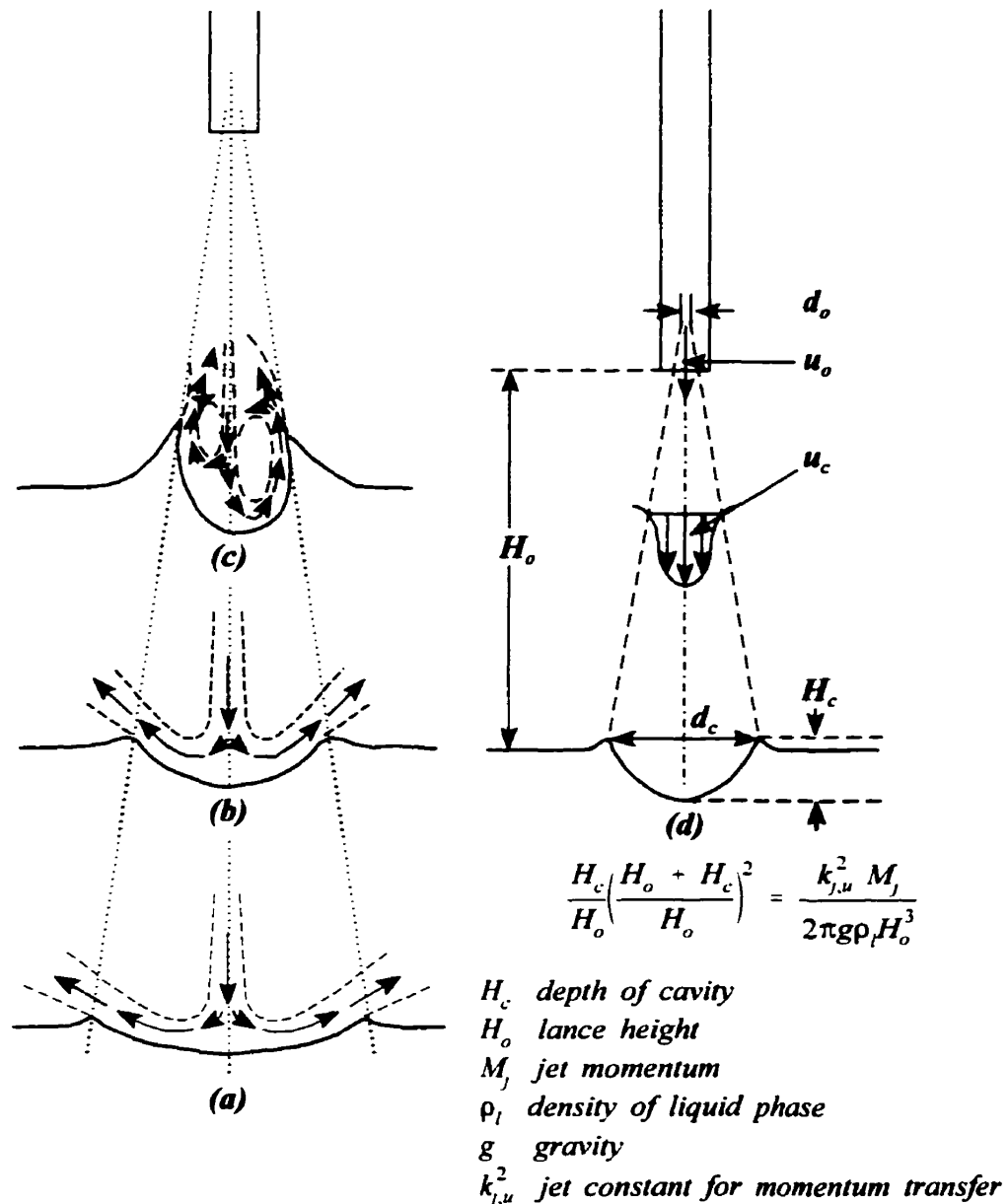


Figure 9. (a) Dimpling of a liquid surface by a low momentum gas jet. (b) Increasing the jet momentum beyond a critical value results in splashing i.e. ejection of material from the impingement area. (c) At high jet momentum the gas penetrates the liquid resulting in a lower volume of ejected material. (d) Schematic depiction of the geometric model developed by Wakelin and the ensuing dimensionless relationship<sup>65</sup>.

Although most industrial top-jetting processes operate in the splash or the penetration regime investigators modelling these procedures at high temperature have operated under the critical zone because flow patterns and interfacial areas can be described by reaction models such as Higbie's Penetration Theory<sup>41</sup>. In top blown batch processes such as iron decarburization and copper desulfurization by oxygen, mass transport control alternates between the gas phase when the impurity level in the liquid phase is high and the liquid phase when the concentration driving force in the bulk liquid drops to a small value. Wakelin<sup>60</sup> and Lohe<sup>64</sup> provided the basis for determining the gas-phase mass transfer coefficient from low temperature models in which jets of air or CO<sub>2</sub> with a momentum of 0.08 N were blown on the surfaces of mercury and water. The Wakelin model<sup>65</sup> depicting the geometry of the impingement area shown Figure 9(d) was used to correlate the measured Sherwood number (*Sh*) to the Reynolds number (*Re*) and Froude number (*Fr*) as<sup>66</sup>:

$$Sh = a[Re(1 + Fr)]^n \quad (9)$$

where  $a = 6.57$  and  $n = 0.43$  for air impinging on water. Schmitt and Wuth<sup>41</sup> also developed an empirical mass transport relationship with the Sherwood number for top-blown systems at high temperature when the jet momentum was 0.3 N and mass changes occurred only in the liquid phase:

$$Sh = K' Sc^{1.75} [Re(1 + K'')]^{1.09} Fr^{0.67} (r_b/h_b)^{0.29} \quad (10)$$

In the above equation  $K'$  and  $K''$  are dimensionless constants, and  $r_b/h_b$  is the ratio of the bath's radius to its depth. The authors expressed the dimensionless groups in order of decreasing importance and found that the Schmidt number,  $Sc$ , containing only the transport properties of the metallurgical system, had the strongest effect on mass transport while the dynamic and geometric factors were less influential.

### **2.2.2. Top Blown Gas Injection with Low Momentum Jets**

Rate measurement relationships developed for high momentum gas jets cannot be extrapolated to low momentum jets without incurring significant error. Alyaser<sup>66</sup> reviewed

mass transfer studies by Kikuchi et al.<sup>67-70</sup> in which low momentum gas impingement in low and high temperature systems was investigated; in both cases the correlation of  $Sh$  to the dimensionless groups were similar for the system parameters defined in Table 1.

**Table 1. Parameters of the experimental system used by Kikuchi<sup>67-70</sup> et al. according to Alyaser<sup>66</sup>.**

Systems Investigated	$Re$	$Sc$	$H/d_o$	$r_s/d_o$	$d_o$ ( $\times 10^2$ m)
Low Temperature	13-1500		0.4-30	1.6-5	0.4-126
Napthalene-N <sub>2</sub>					
Toluene-N <sub>2</sub>					
Acetic Acid-N <sub>2</sub>					
Water-N <sub>2</sub> -NH <sub>3</sub>					
High Temperature					
Graphite-CO-CO <sub>2</sub>		0.57-0.93	1.5-6.3	1.4-3.1	0.4-1.3
Liquid Fe-CO-CO <sub>2</sub>		0.57-0.9	0.8-1.5	1.4-2.9	0.66-1.3

At low temperature the effect of nitrogen impingement on the sublimation of napthalene or the evaporation of toluene, water or acetic acid was expressed as<sup>66</sup>:

$$Sh = (0.40 \pm 0.13)(r_s/d_o)^{-1} Re^{0.66} Sc^{0.5} \quad (11)$$

where  $r_s$  is the radius of the reaction area and  $d$  is the inner diameter of the lance. The high temperature oxidation of graphite and decarburization of iron by CO-CO<sub>2</sub> gas mixtures yielded the following respective relationships<sup>66</sup>:

$$Sh = (0.32 \pm 0.06)(r_s/d_o)^{-1.5} Re^{0.66} Sc^{0.5} \quad (12)$$

$$Sh = (0.27 \pm 0.05)(r_s/d_o)^{-1} Re^{0.76} Sc^{0.5} \quad (13)$$

It was concluded that the gas-liquid reaction rate was controlled by resistance in the gas-phase mass when the exponent for the Reynolds number was between 0.66 and 0.76<sup>66</sup>.

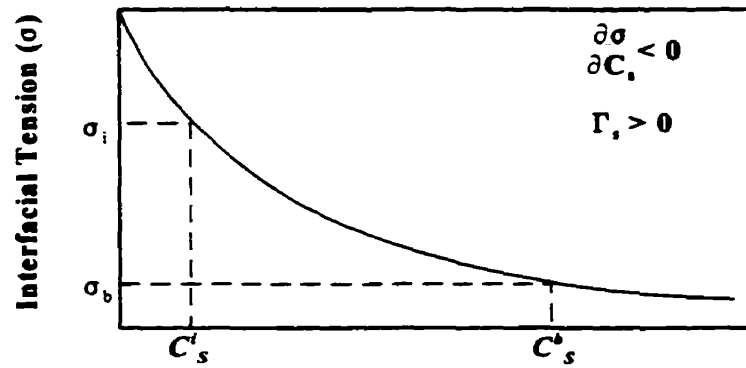
### **2.3 Interfacial Phenomena**

#### **2.3.1 Surface Active Solutes and Surface Tension**

Within a liquid, attractive forces are exerted on each molecule by its surrounding neighbours. When the liquid is partitioned to create a gas-liquid interface, the surface atoms lose half their neighbours and there is a tendency towards minimum surface area because of a net inward attraction acting on the surface atoms<sup>71</sup>. The work associated with surface area minimization or the surface tension ( $\sigma$ ) is governed by the strength of intermolecular attractions in the liquid. Strong intermolecular attractions lead to high surface tensions, molar heats of vaporization, boiling points, and viscosities.

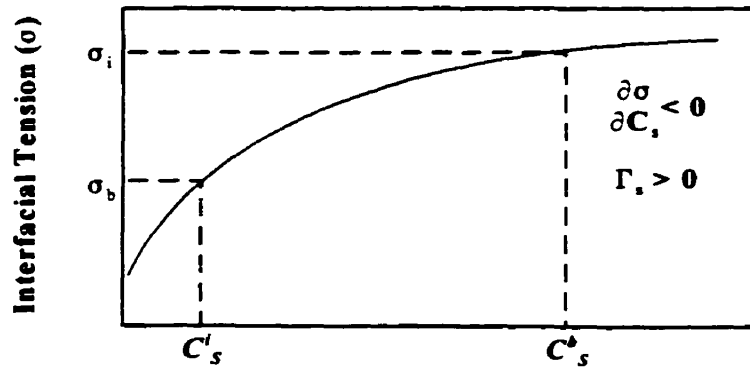
Strongly adsorbed solutes on the liquid surface, an applied potential or changes in temperature can all affect the interactions between surface molecules<sup>72</sup>. A surface active solute can decrease the surface tension of a liquid with increasing solute concentration ( $\partial\sigma/\partial C_s > 0$ ) when it is positively adsorbed ( $\Gamma_s > 0$ ), i.e., when it is in excess on the surface relative to the bulk (see Figure 10(a)) while the converse ( $\partial\sigma/\partial C_s < 0$ ) applies when the solute is negatively adsorbed ( $\Gamma_s < 0$ ) (see Figure 10(b)). Systems which exhibit electrocapillary behaviour such as amalgam-electrolyte and liquid metal - fused salts experience changes in interfacial tension as seen in Figure 10© when a potential is applied at the interface.

Most surface active solutes in liquid metals adsorb positively on the melt surface. The Group VIb elements, i.e. O, S, Se, and Te, are the most commonly encountered solutes lowering interfacial tension in ferrous and non-ferrous pyrometallurgical refining procedures<sup>71</sup>. Elevating the temperature of a liquid metal solution containing a positively adsorbed solute increases its surface tension. These effects are illustrated respectively for oxygen and sulfur dissolved separately in liquid copper at various temperatures in Figure 11(a) and Figure 11(b). Both figures also show that the effect of solute concentration on surface tension becomes less pronounced at higher temperatures.



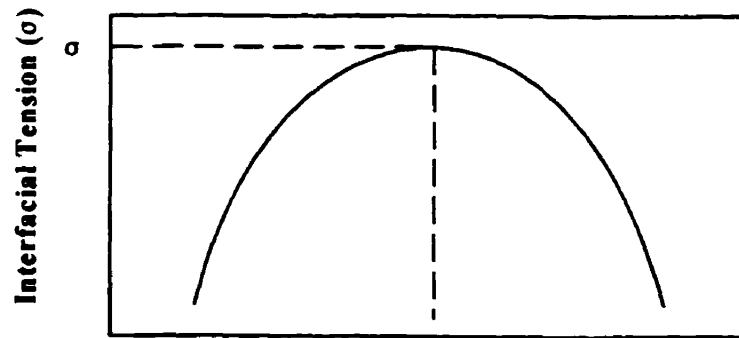
Solute Concentration

(a)



Solute Concentration

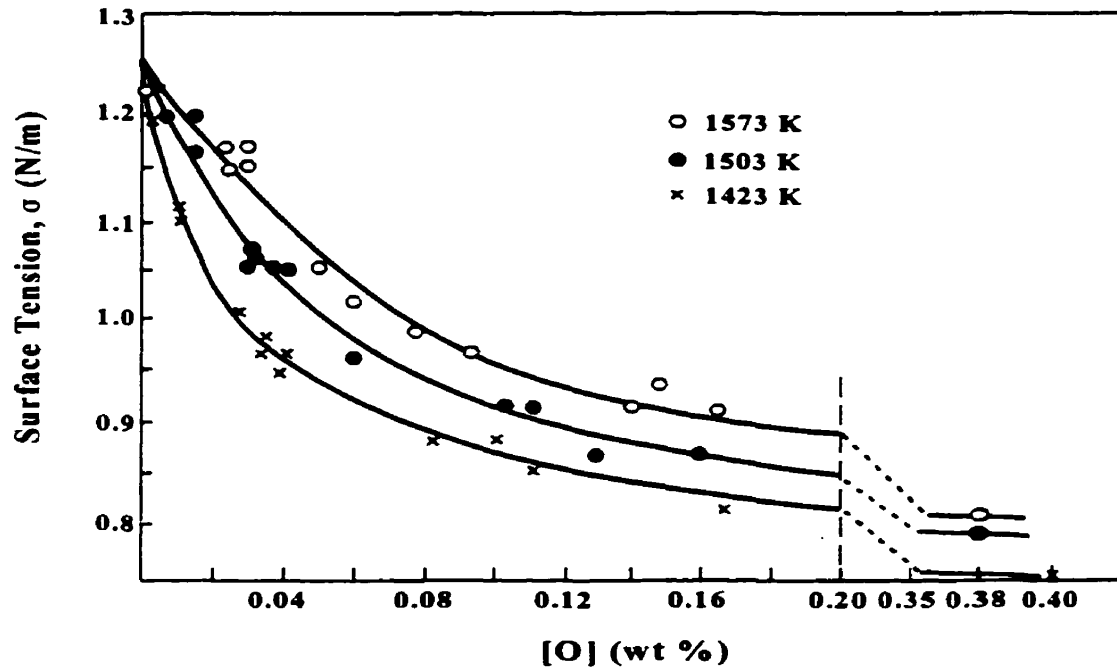
(b)



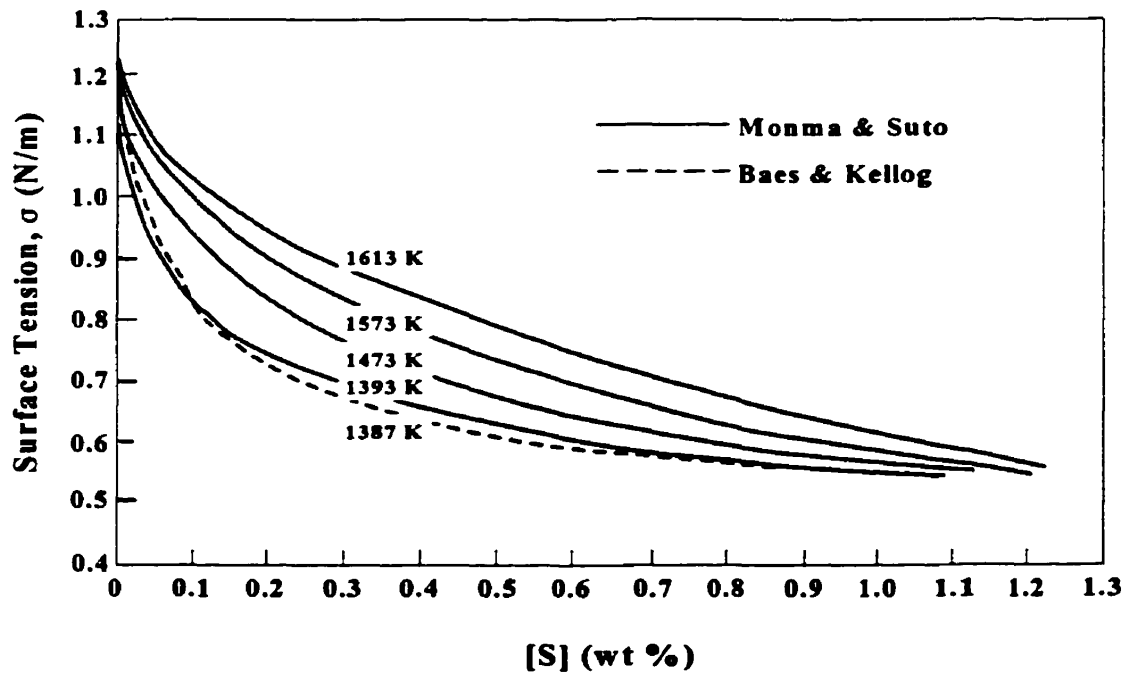
- Potential (+)  $E_m$  (-) Potential -

(c)

Figure 10. Types of adsorption behaviour observed at liquid-metal interfaces (a) positive adsorption (b) negative adsorption (c) electrocapillary behaviour, according to Brimacombe<sup>72</sup>.



(a)



(b)

Figure 11. Effect of (a) dissolved oxygen and (b) dissolved sulphur on the surface tension of liquid copper at various temperatures according to Monma and Suto<sup>73</sup>.

The accumulation of surface tension data for a liquid metal is usually performed by measuring the dimensions of a sessile liquid drop resting on a horizontal surface over a range of solute compositions and temperature. Applying this data to the Langmuir and Gibbs adsorption isotherms yields a relationship between the activity of the solute and the depression in the surface tension of the liquid metal solution. In the simplest case of a single chemisorbed solute,  $I$ , the Langmuir adsorption isotherm describes the fractional coverage  $\theta_i$  of the liquid surface as<sup>74</sup>:

$$\frac{\theta_i}{1 - \theta_i} = K_i a_i \quad (14)$$

where  $a_i$  is the activity of the solute  $I$  and  $K_i$  is a temperature dependent equilibrium or adsorption coefficient. The appropriate form of the Gibbs isotherm providing the surface concentration or adsorption of the solute is<sup>75</sup>:

$$d\sigma = - \left( \Gamma_B - \frac{X_B}{X_A} \Gamma_A \right) d\mu_B \quad (15)$$

where  $\sigma$  is the surface tension,  $\Gamma_A$  and  $\Gamma_B$  are the adsorptions of the bulk phase A and solute B respectively,  $X_i$  represents the atom fraction of the two components in the bulk phase and  $\mu_B$  is the chemical potential of B. Under strong adsorption behaviour Equation (15) can be simplified to<sup>57</sup>:

$$\frac{d\sigma}{d \ln a_i} = -RT\Gamma_i = -RT\theta_i \Gamma_i^\circ \quad (16)$$

where  $\Gamma_i^\circ$  is the temperature independent adsorption at full coverage. Substituting for  $\theta_i$  from Equation (14) and integrating yields in the limiting case of a pure solvent<sup>75</sup>:

$$\sigma^\circ - \sigma = RT\Gamma_i^\circ \ln(1 + K_i a_i) \quad (17)$$

where  $\sigma'$  and  $\sigma$  are the surface tensions of the pure metal and alloy. For a strongly adsorbed solute,  $\Gamma'_s$  can be obtained as the linear slope from a plot of  $\sigma$  vs  $\ln a_s$ .

Equilibrium surface concentrations on liquid metal interfaces can be established almost instantaneously. A simplified form of the diffusion equation:

$$n = 2\left(\frac{D}{\pi}\right)^{1/2} t^{1/2} C \quad (18)$$

where  $n$  is equal to the surface excess,  $C$  is a constant concentration gradient between the interface and bulk liquid and  $D$  is the diffusivity of the solute, was used by Richardson<sup>72</sup> to demonstrate that the equilibrium surface concentration of oxygen in liquid iron is reached within  $10^{-3}$  to  $10^{-5}$  second even when oxygen was present at one-tenth its bulk saturation concentration.

The above treatment considers ideal adsorption of a solute on a liquid metal surface consisting of equivalent sites. Deviations from this behaviour arise when there are attractive or repulsive interactions in the adsorbate or other competitively adsorbed solutes present. Sun and Belton<sup>76</sup> reported that in the liquid Cu-S system repulsive interactions in the adsorbate led to more rapid than expected coverage of the liquid copper surface with increasing sulfur concentration. Negative deviations from ideality observed by Gallois and Lupis<sup>77</sup> in the liquid Cu-O were ascribed to attractive forces acting between the adsorbed oxygen atoms. The contrasting behaviour of various adsorbates may be related to differences in the structure of the surface layer and size of the adsorbed atoms but an adequate model to corroborate these assumptions has yet to be developed. The traditional model describes surface saturation of a liquid metal substrate as close-packed coverage by a monolayer of doubly charged anions (e.g.  $O^{2-}$ ,  $S^{2-}$ ,  $Se^{2-}$ ) however for the Ag-O and Cu-O systems surface saturation by oxygen ions is less than close-packed and more consistent with coverage by a two dimensional ionic compound with the stoichiometry  $M_3O$  (where  $M$  = metal atom)<sup>77,78</sup>.

Surface interactions are further complicated when two or more solutes are present together because the effects are generally not additive and may be influenced unpredictably by other non-active solute elements. Chromium and carbon in liquid iron are two non-active

solutes individually but when present together at low concentrations result in lowered interfacial tension<sup>72</sup>. Belton proposed that the interactions between two competitively adsorbed solutes may be addressed by introducing a coverage dependent surface activity coefficient into Equation (14) leading to a more general form of the Langmuir isotherm<sup>74</sup>:

$$\frac{\theta_i \gamma_i'}{1 - \sum_j \theta_j} = K_i a_i \quad (19)$$

### **2.3.2 The Role of Surface Active Solutes on Reaction Rates**

Interfacial phenomena are not considered to affect thermodynamic equilibria between different phases but are known to influence the rates of interfacial chemical reactions the extent which depends on the nature of the solute, its surface activity and mass transport conditions in the liquid<sup>79</sup>.

Mass transfer in most pyrometallurgical refining procedures takes place under strong mixing conditions and in the absence of surface active elements agitation of the melt produces eddies which transport elements of fluid from the bulk to the interface resulting in constant renewal of the liquid surface<sup>79</sup> (see Figure 12(a)). At the interface, mass transport to and from the fluid element can occur by unsteady-state diffusion until it is displaced by another eddy. Depending on the level of melt agitation the residence time of the eddy at the interface can range from  $10^{-4}$  second for vigorous stirring to approximately 1 second for more quiescent conditions<sup>79</sup>. Non-reactive solutes strongly adsorbed on the liquid surfaces can reduce mass transfer coefficients by blocking reaction sites at the interface and inhibiting chemical reaction of less surface active solutes and by lowering the rate of surface renewal. Under strong mixing conditions, the eddy surface during its lifetime at the interface may remain free of adsorbed material but under gentle stirring it may establish the equilibrium concentration of the adsorbed solute and hence interrupt mass transfer and chemical reaction at the interface. Areas of reduced surface tension created by the adsorbed solute also diminish reaction rates by opposing eddy dispersal at the surface i.e. surface renewal, with a force equal to the difference of the two surface tensions (see Figure 12(b)). At higher solute surface concentrations and under quiescent conditions the number, frequency and area

of surface clearings decreases which can arrest both diffusional and eddy processes.

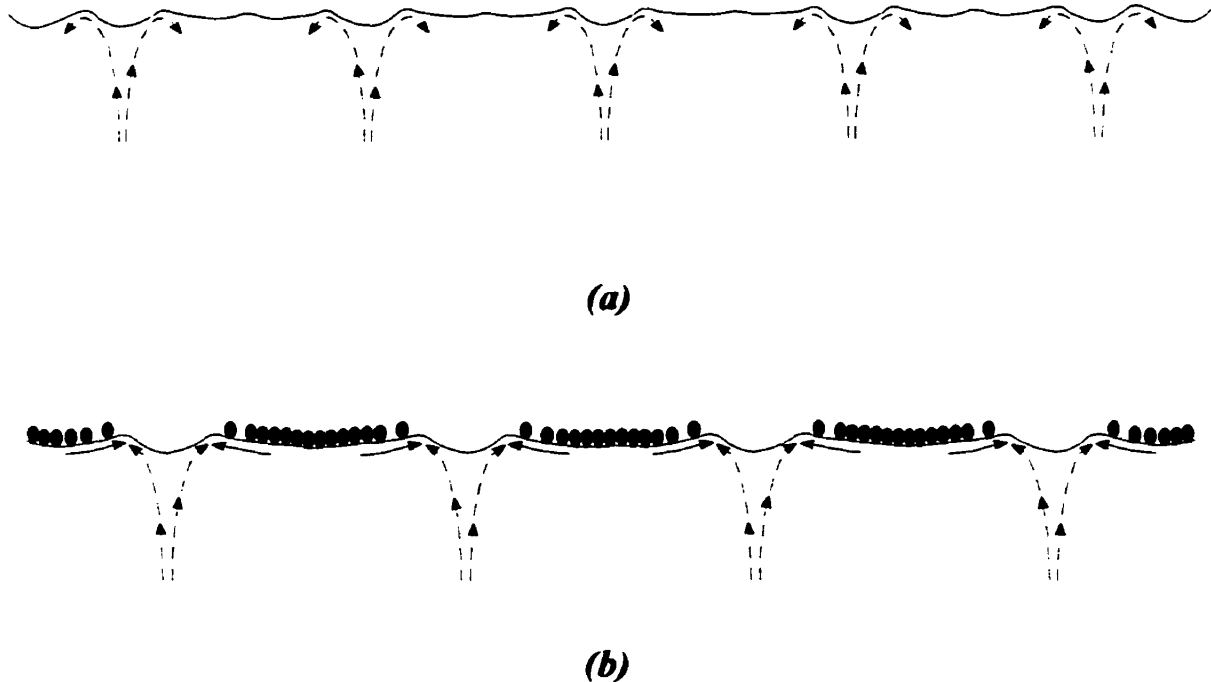


Figure 12. Surface renewal by eddies at interfaces: (a) no surface active material present (b) in the presence of surface active material according to Richardson<sup>79</sup>.

Darken and Turkdogan<sup>80</sup> reviewed a number of gas-liquid systems where there is strong chemisorption and found that the interfacial reaction rate was usually proportional to the reciprocal activity of the interfering solute and that the limiting behaviour was consistent with Langmuir adsorption with interfacial reaction occurring at vacant sites. The apparent rate constant,  $k_a$ , for such an interfacial reaction in the presence of one chemisorbed solute is described by<sup>74</sup>:

$$k_a = k(1 - \theta_i) \quad (20)$$

where at high surface coverage, i.e.  $K_i a_i \gg 1$ , or when the concentration of a surface active solute approaches bulk saturation equation 20 reduces to<sup>74</sup>:

$$k_a = \frac{k}{K_i a_i} \quad (21)$$

In a multicomponent system having a number of interfering solutes with a fraction of sites available only for reaction, Belton proposed a generalized form of the rate equation<sup>74</sup>:

$$k_a = k \left[ (1 - \rho_{(t)}) \left( 1 - \sum_j \theta_j \right) + \rho_{(t)} \right] \quad (22)$$

where  $\rho$  represents the fraction of surface available for reaction. Belton<sup>74</sup> approximated the apparent rate constant for the adsorption of nitrogen in liquid iron in the presence of oxygen and sulfur from Fruehan and Martonik's<sup>81</sup> data by combining equations (19) and (21) yielding under the assumption that  $\gamma_i = 1$ :

$$k_a = \left( \frac{K_S a_S}{k} + \frac{K_O a_O}{k} \right)^{-1} \quad (23)$$

Fruehan and Martonik<sup>82</sup> also found that the kinetics of the same reaction can be increased with the addition of chromium, a non-surface active solute, because of its ability to suppress sulfur activity<sup>74</sup>.

### **2.3.3 Surface Tension Driven Flow**

Surface tension gradients in other instances can lead to surface turbulence which may increase the rate of interfacial reaction kinetics. James Thomson correctly identified this phenomenon in 1855 while investigating the motion of alcohol droplets on the surface of water<sup>83</sup>. Surface tension driven flow or "Marangoni convection" arises when a shear stress develops along a liquid surface and changes the motion of fluid along the interface in the direction of highest interfacial tension resulting in increased heat and mass transport. This shear stress  $\tau_x$ , expressed along a direction  $x$ , as<sup>84</sup>:

$$\tau_s = \frac{d\sigma}{dx} = \frac{\partial\sigma}{\partial T} \cdot \frac{dT}{dx} + \frac{\partial\sigma}{\partial C} \cdot \frac{dC}{dx} + \frac{\partial\sigma}{\partial\psi} \cdot \frac{d\psi}{dx} \quad (24)$$

develops from gradients of temperature  $T$ , concentration of a surface active solute  $C$  in the liquid or electrical potential  $\psi$  between two liquids, however, in many systems the effect of temperature is small unless the temperature gradients at the interface are very large<sup>71</sup>. Following Thomson's early experiments, Marangoni convection has since been recognized to maintain foam film stability against hydrodynamic drainage<sup>85</sup>, influence the size, shape, and properties of welds<sup>86</sup>, enhance the rates of gas-liquid metal reactions that are transport controlled in the liquid phase, i.e., copper desulfurization<sup>66,87</sup>, nitrogen absorption in liquid iron<sup>88</sup>, and cause local refractory corrosion in steelmaking furnaces by slag film motion above the slag level<sup>84</sup>.

Brimacombe and Weinberg<sup>89</sup> first recorded the occurrence of interfacial motion in liquid metals when a low momentum ( $< 6 \times 10^{-5}$  N) oxygen jet was impinged on the surfaces of liquid copper and tin. An oxide patch observed on the melt surface directly beneath the gas lance was seen to move radially outward from the center of the bath to the periphery of the liquid surface at high velocity (see Figure 13). The interfacial motion was attributed to localized surface tension gradients between the oxide and surrounding metal caused by the non-uniform transfer of oxygen at the interface. Similar behaviour has been reported by Lange and Wilken<sup>90</sup> for a number of low and high temperature two phase systems while Barton and Brimacombe's<sup>91</sup> measurements of oxygen absorption in liquid copper credited Marangoni convection with increasing mass transfer coefficients by an order of magnitude.

Other local sources of solutes are capable of invoking surface tension flow on both the micro and macro-scale. In stirred melts, eddies carrying a positively adsorbed surface active solute from the bulk phase to the melt surface can lead to micro-scale interfacial motion due to the lower surface tension of the eddy fluid element relative to the surrounding interface<sup>71</sup> (Figure 14(a)). Convective motion can also occur from the dissolution of a partially immersed solid because of resulting longitudinal surface tension gradients which lead to movement away from the interface if the solute is positively adsorbed ( $\Gamma_s > 0$ ) and towards the interface if the solute is negatively adsorbed ( $\Gamma_s < 0$ )<sup>72</sup> (Figure 14(b)).

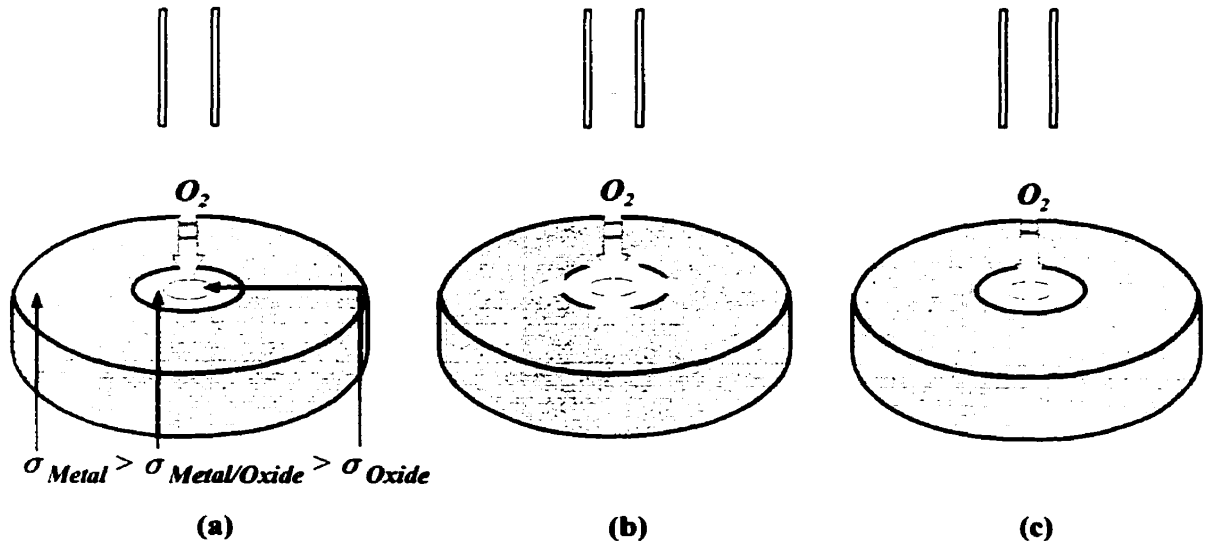


Figure 13. Macro-scale interfacial motion on the surface of liquid copper generated by (a) the impingement of an oxygen jet on the melt surface which leads to (b) radial spreading of the oxide patch at high velocity towards the regions of highest surface tension (c).

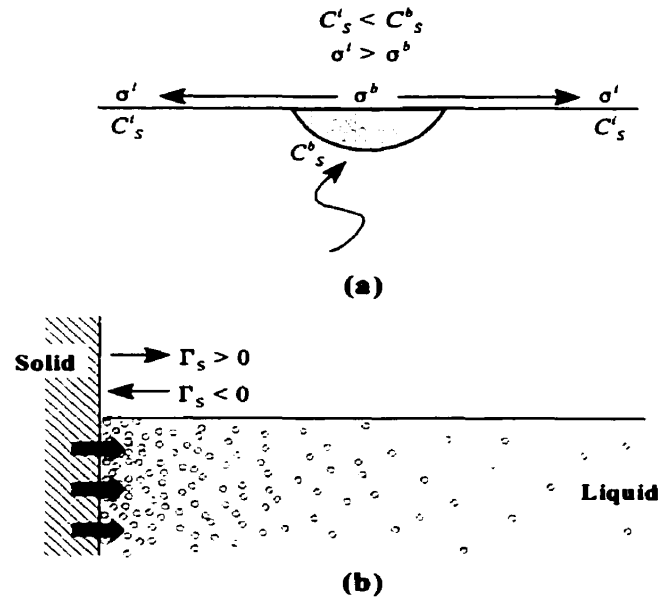


Figure 14. (a) Micro-scale interfacial motion generated by the penetration of eddies at the gas-liquid interface with a solute composition exceeding that of the interface resulting in motion towards regions of higher interfacial tension, according to Brimacombe<sup>72</sup>. (b) Macro-scale interfacial motion generated by the dissolution of a partially immersed solid resulting in liquid motion away from the solid-liquid interface when there is positive adsorption of the solute on the liquid surface and towards the solid-liquid interface when there is negative solute adsorption on the liquid surface according to Brimacombe<sup>72</sup>.

Prediction of the onset of interfacial motion has been attempted with limited success using hydrodynamic stability analysis on gas-liquid systems involving aqueous and organic solutions by examining the ratio of the destabilizing interfacial tension force resulting from mass transfer to viscous forces i.e. the Marangoni number<sup>72</sup>:

$$Ma = \frac{\alpha\beta d^2}{\mu D} \quad (25)$$

In liquid metal systems where interfacial tension, liquid density and adsorption effects are much greater it is more convenient to evaluate interfacial movement in terms of an initial spreading coefficient,  $S$ , which in the case of oxygen blown on a liquid metal surface is expressed as<sup>72</sup>:

$$S = \sigma_{Metal} - (\sigma_{Oxide} + \sigma_{Metal/Oxide}) \quad (26)$$

where  $S$  must be positive for oxide movement to occur.

## **2.4 Oxidation Studies**

Rate determinations for the desulfurization or oxidation of copper-sulfur melts are often performed by thermogravimetry, whereby the mass of the charge is recorded as a function of time, by on-line analyses of the exiting reaction gases, through periodic chemical analyses of the melt or by a combination of these methods. A common observation in many of these studies is the removal of sulfur in two or three distinct stages: a slow and sometimes variable initial desulfurization stage followed by a dominant stage of relatively rapid sulfur elimination and ending with a final stage of decelerated desulfurization.

Ajersch and Toguri<sup>40</sup> measured the oxidation rates of liquid copper sulfide by thermogravimetry under gas diffusion control conditions and saw three distinct regions in the desulfurization curve of  $\text{Cu}_2\text{S}$  as it progressed to liquid Cu. An initial stage of variable weight loss was attributed to the time required for the diffusing oxygen gas to establish steady-state conditions. In the second stage as the melt composition entered the  $\text{Cu}_{(l)} - \text{Cu}_2\text{S}_{(l)}$  miscibility gap region desulfurization (weight loss) proceeded at a constant rate. When the

copper sulfide phase was eliminated the melt continued to lose weight at a slower rate although past a critical point continued oxygen delivery to the melt resulted in a net weight increase due to copper oxide formation. Throughout the desulfurization procedure the composition of both liquid phases was assumed to be invariant and equilibrium conditions maintained through continuous mixing of the sulfide phase by the settling motion of the denser liquid copper droplets. The mass-time curves of iron bearing matte oxidized under similar conditions by Asaki et al.<sup>92</sup> followed a similar path although the initial stage was characterized by a mass gain due to oxidation of the iron to iron oxide.

Fukunaka et al.<sup>93</sup> bubbled Ar-O<sub>2</sub> gas mixtures into molten copper containing 0.74 wt% S and 0.01 wt % O at 1523 K and, as with Ajersch and Toguri<sup>91</sup>, described an initial period of slow sulfur removal, followed by an interval of rapid sulfur elimination that ended with a period of decelerated desulfurization. In both the first and third stages, the slower desulfurization rate coincided with significant oxygen dissolution in the melt. Gas flowrate ( $1 \times 10^{-5} \text{ m}^3/\text{s}$  to  $2 \times 10^{-5} \text{ m}^3/\text{s}$ ), oxygen partial pressure of the gas stream (10 kPa to 30 kPa) and lance immersion depth in the melt (0.018 m to 0.033 m) were all varied to determine their effect on the rate of desulfurization. Higher gas flowrates and oxygen partial pressures in the injected gas increased the rate of the second stage and shortened the duration of the initial stage while changes in the lance immersion depth negligibly affected these rates. In the vicinity of the lance, it was assumed that oxygen was consumed by the two elementary reactions:



and that equilibrium was reached between the sulfur dioxide in the gas bubble and the composition of the melt. A model describing mass transfer around a single gas bubble suggested desulfurization was controlled by mass transfer in the gas boundary layer and therefore the rates of the above reactions were determined by the rate of oxygen supply into the melt. The authors also observed some desulfurization during melting of the copper alloy

which made the starting concentration of sulfur a variable between each test. Ohno<sup>76</sup> confirmed that considerable desulfurization and deoxidation can occur from Cu-S-O alloys during melting or solidification. Alloys of varying O and S concentrations were inductively melted between 1373 K and 1573 K under a vacuum or an argon atmosphere ( $P_{Ar} = 6.5$  kPa to 101.6 kPa) or were solidified and then remelted under argon ( $P_{Ar} = 1.33$  kPa to 102 kPa) and then chemically analyzed for O and S. In all circumstances, the observed weight change ratio between sulfur and oxygen was very close to one indicating sulfur and oxygen were eliminated as  $SO_2$ . Under vacuum melting, the rates of sulfur and oxygen removal could be expressed as a first order rate equation while their rate constants could be determined with respect to the inverse of temperature. However under an inert atmosphere, desulfurization and deoxidation showed a dependence on dissolved S and O concentrations but not on argon pressure. Most S and O elimination was believed to take place during melting or solidification of the alloy when the equilibrium  $SO_2$  pressure becomes much higher than the applied argon pressure. These findings agreed with Floe and Chipman's<sup>95</sup> solubility study of sulfur dioxide in molten copper and Knacke and Probst's<sup>96</sup> work concerning the solidification of copper melts saturated with  $SO_2$ . Floe and Chipman arrived at an expression relating the equilibrium pressure of  $SO_2$  to temperature and the sulfur and oxygen concentration of the melt<sup>93</sup>:

$$\log P_{SO_2}(Pa) = \frac{6700}{T} + \log(wt\% S)(wt\% O)^2 + 2.21 \quad (29)$$

Ohno applied this equation at a number of solute concentrations in the temperature range of 1373 K to 1573 K to demonstrate that  $SO_2$  formation is favourable even at low solute levels.

In Knacke and Probst's<sup>96</sup> experiments, copper melts cooled at various rates (0.2 K/min to 5 K/min) continuously expelled sulfur dioxide until the liquidus temperature (1353K) of copper was reached; further cooling to 100 K below the melting point of copper resulted in a sudden evolution of the remaining gas. Ohno witnessed a similar phenomenon in the form of vigorous boiling during alloy solidification and referred to the equilibrium diagram presented by Knacke and Probst showing the variation of the sulfur dioxide pressure

in equilibrium with solid copper, copper sulfide, copper oxide and the liquidus curve of copper (see Figure 15). During liquefaction of a Cu-S-O alloy, the pressure of sulfur dioxide increases to above 600 kPa and then drops along the liquidus curve of copper with increasing temperature: during solidification the solutes are concentrated in the remaining molten material and the pressure of  $\text{SO}_2$  increases similarly.

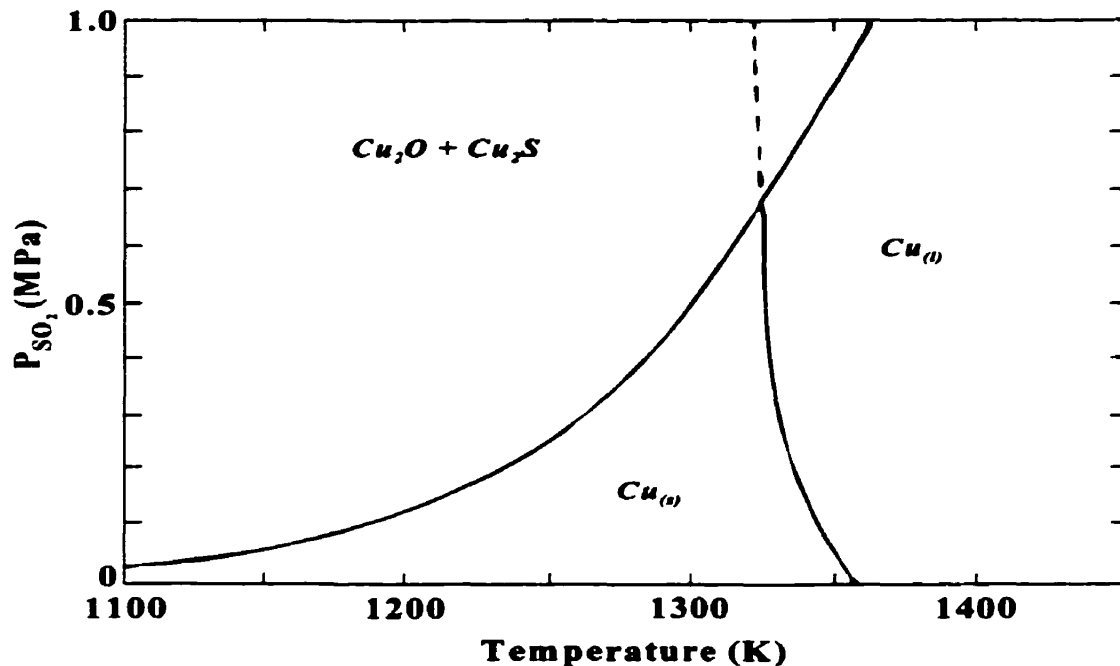


Figure 15. Variation of the sulfur dioxide pressure in equilibrium with  $\text{Cu}_{(l)}$ ,  $\text{Cu}_2\text{S}$ ,  $\text{Cu}_2\text{O}$  and the liquidus curve of copper<sup>96</sup>.

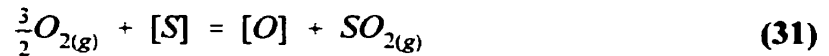
In Rottman and Wuth's<sup>97</sup> top blown conversion experiments, gas jets of varying oxygen composition were delivered through a lance fitted with a laval-type nozzle onto 2kg baths of molten copper matte (65 wt% Cu, 14 wt% Fe and 21 wt% S) at temperatures up to 1873 K. By fixing the lance position at 0.07 m above the unstirred melt the oxidizing gas exited at super-sonic velocities with sufficient momentum to stir the liquid phase without invoking splashing. Under these conditions the authors concluded the rate-controlling step during conversion was diffusion of the reaction gases through the viscous sub-layer of the impinging gas jet. Mass changes in the melt revealed two periods of desulfurization each proceeding at a distinct rate. In the first period constant oxygen dissolution into the melt was

accompanied by simultaneous reaction of oxygen diffusing through the gas boundary layer at the gas-liquid interface. The authors postulated that sulfur was removed by the reaction of the dissolved oxygen with sulfur in the liquid phase in conjunction with the direct reaction of oxygen in the gas phase at the gas-liquid interface. When the melt became saturated with oxygen ( $\sim 0.6$  wt% O), the desulfurization rate increased to roughly twice the rate observed in the first period and was accompanied by slag formation and increased turbulence in the gas phase due to  $\text{SO}_2$  evolution at the melt surface. Although slag coverage reduced the surface area available for reaction, a comparison of the oxidation rates of white metal and iron bearing matte showed no significant difference, indicating mass transfer was taking place primarily in the vicinity of the surface depression caused by the gas jet.

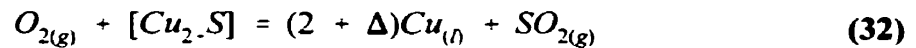
Top-blown conversion experiments were also performed Bryukvin et al.<sup>98</sup> at 1473 K - 1673 K using synthesized  $\text{Cu}_2\text{S}$  melts ( $5 \times 10^{-4}$  -  $2 \times 10^{-3}$  kg), instead of matte, and oxygen-nitrogen gas mixtures (12 - 30 vol.%  $\text{O}_2$ ) blown at a fixed rate of  $1.67 \times 10^{-6}$  m<sup>3</sup>/s. Two distinct regions were observed in the mass-time curve of the melt samples: an initial stage of comparatively low mass loss followed by a secondary stage of accelerated mass loss. Although the desulfurization rate generally increased with reaction zone temperature and oxygen partial pressure, the initial stage was more influenced by temperature whereas the secondary stage was more affected by gas composition. The transition to secondary stage desulfurization occurred, as with Rottman and Wuth, at a certain degree of melt oxidation although this value was not specified. Increased rates of mass loss in the secondary stages were attributed to metallization of the melt and evolution of dissolved oxygen from the bath through the decomposition of oxysulfide phases. The reaction kinetics were found to be zero order with respect to the sulfur concentration of the melt but not to the temperature and oxygen partial pressure of the gas jet. The desulfurization mechanism in both stages was correlated to activation energies calculated for the primary and secondary oxidation stages at different bath temperatures. At 1473 K, the higher activation energy of the first stage was associated with chemisorption of oxygen onto the melt surface whereas the lower activation energy of the second stage was characteristic of diffusion. In experiments performed at 1673K, the difference between the activation energies was less pronounced implying that the

distinction between the two stages is diminished at higher temperatures and mass transfer becomes dependent on the mixing conditions of the melt.

Jalkanen<sup>99</sup> sought to determine the phenomenology of oxidation of molten copper sulfide at 1423 K - 1623 K. Temperature, gas velocity, oxygen partial pressure were varied in addition to the Cu:S molar ratio of  $Cu_2S$  which ranged between 1.875 to 2.30. Gas velocity was maintained at less than 2 m/s to avoid forming a depression on the melt surface. The mass-time curves of the sulfide oxidation indicated two stages of desulfurization; the first was related to oxygen and copper saturation of the melt by the reactions:



Upon saturation of the melt, conversion proceeded to the second stage by the reaction:



which was assumed to occur in several steps: oxygen adsorption (Equation (33)) followed by the formation of an intermediate activated complex as proposed by Byerley et al.<sup>100</sup> (Equation (34)) which then reacted with dissolved oxygen to produce sulfur dioxide (Equation (35)) that was subsequently released into the gas phase.



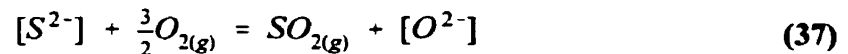
Sulfur removal increased with gas velocity and oxygen partial pressure yet its relation to temperature was less obvious; a positive temperature dependence on the rate of desulfurization was noted during the second stage at zero top blowing velocity but this dependence became negative at a value between 0 and 1 m/s (NTP). It was concluded that the conversion of copper sulfide to metallic copper was controlled jointly by the rate of mass transfer of the oxidizing gas to the melt surface and the kinetics of the chemical reaction.

Radioisotope experiments by Morland, Mathew and Hayes<sup>101</sup> indicated that formation of an activated complex may be rate-controlling only in the chemical reaction sequence of SO<sub>2</sub> generation from a copper sulfide melt. The reaction kinetics were determined by measuring the transfer rate of the radioisotope S<sup>35</sup> from molten copper sulfide to gas mixtures of SO<sub>2</sub>/CO/CO<sub>2</sub> in equilibrium with the melt under conditions that ensured the results would be independent of gas flowrate over the melt surface, melt size, and the isotope concentration in the original melt. The authors concluded that SO<sub>2</sub> generation was controlled by the formation and decomposition of the activated complex SO\* according to the reaction:



However their estimated reaction rate for copper sulfide oxidation in air at 1523 K was relatively high at 1 mol SO<sub>2</sub> m<sup>-2</sup>s<sup>-1</sup> suggesting to the authors that reaction rates in real systems are mass transport controlled.

Contrasting the activated complex hypotheses was an electrochemical model proposed by Alyaser and Brimacombe<sup>66,87</sup>, in due consideration of the ionic nature of the sulfide melt, to describe desulfurization of Cu<sub>2</sub>S baths top-blown with O<sub>2</sub>-N<sub>2</sub> gas mixtures. The experiments consisted of varying oxygen partial pressure (0.2 to 0.78 vol. %), gas flowrate (1.67 × 10<sup>-5</sup> to 6.67 × 10<sup>-5</sup> m<sup>3</sup>/s), bath temperature (1473 K to 1573 K) and mixing conditions in the bath. Desulfurization was reported to occur at two distinct rates that were controlled by the transfer of oxygen in the gas phase to the melt surface. These rates increased with oxygen partial pressure and the rate of gas delivery to the melt surface but were negligibly affected by temperature. In the first stage, oxygen dissolution was accompanied by simultaneous partial desulfurization of the melt according to the reaction:



The transition to the second stage upon oxygen saturation of the melt resulted in a higher rate of sulfur removal than the preceding stage due to the reaction of oxygen at the melt surface in conjunction with the overall bath reaction:



The negligible liquid phase resistance to mass transfer was attributed to the ionic nature of the melt and to agitation provided by Marangoni convection and spontaneous sulfur dioxide eruptions from the melt, the latter phenomenon having also been previously reported by Barton and Brimacombe<sup>102</sup> in surfactant studies involving the dissolution of solid Cu<sub>2</sub>S in copper melts.

### **2.5 Hypothesis**

The review of the relevant literature regarding copper converting and oxidation suggests that surface phenomena may be responsible for decreasing the rate of sulfur removal at the end of oxygen blowing in the INCO finishing procedure. It is hypothesized that upon oxygen saturation of the melt there is a cessation of Marangoni convection at the melt surface and that surface blockage by solid NiO formation or by oxygen and/or sulfur adsorption may be reducing the number of available reaction sites for sulfur elimination.

### **3.1 Experimental Program**

The hypothesis presented in Chapter 2 attributed the reduction in mass transfer rates during second stage converting to blocking of the melt surface through the formation of nickel oxide (NiO) and a decrease in melt agitation from the cessation of surface tension driven flow upon oxygen saturation of the melt. To test this hypothesis the rates of oxygen dissolution/sulfur removal were measured for cathode Cu, Cu - 1 wt % S and Cu- 3 wt % Ni - 1 wt % S melts at 1523 K when top blown with O<sub>2</sub>-N<sub>2</sub> gas mixtures at various oxygen partial pressures and gas flowrates.

Top-blowing of O<sub>2</sub>-N<sub>2</sub> onto molten cathode copper was carried out to observe the occurrence of surface tension driven flow in a quiescent bath when only one surface active agent (oxygen) was present and to provide a comparison to the measured oxygen solubilities of Cu-S and Cu-Ni-S melts tested under similar conditions.

### **3.2 Test Apparatus**

#### **3.2.1 Design Criteria**

Melting of a Cu-S alloy under a vacuum or an inert atmosphere has been shown to result in significant sulfur evolution<sup>94</sup> while surface tension driven flow has been attributed to concentration gradients in addition to thermal and electrical gradients<sup>72</sup>. To minimize premature sulfur losses, melt oxidation, and possible thermal contributions to surface tension driven flow it was desired to rapidly reach the process temperature of 1523 K under an inert atmosphere and maintain good temperature control in the bath at the setpoint temperature. Uncertainty in the observation of any surface phenomenon could be reduced further by visually recording the melt surface under quiescent bath conditions.

#### **3.2.2 Selection of Furnace Technology**

##### ***Parabolic Clamshell Heater***

Induction melting of metallic charges was not considered because electro-magnetic stirring of the bath was believed to mask the occurrence of surface tension driven flow and

also upon INCO's suggestion not to consider desulfurization of inductively stirred melts since it was felt this had been done previously.

Radiative heating of the copper charge was then attempted with a Research Incorporated parabolic clamshell heater model 4068. The furnace consisted of twenty-four, 2000 W, infra-red lamps vertically mounted and assembled in a hexagon comprising of four lamps per side. The lamps, connected in a three-phase, delta-series configuration with a 480V drop across each phase, provided a combined power output of 48,000 W. Infra-red radiation emitted by the lamps was directed to a focal point at the center of the furnace cavity by a parabolic aluminum reflector positioned behind each lamp. These reflectors were cooled with water flowing at  $3 \times 10^{-4} \text{ m}^3/\text{s}$  through a copper tube attached to their anterior surface.

Although the radiation furnace could achieve rapid heating rates, several technical deficiencies rendered its use impractical. To reach the setpoint temperature of 1523 K the furnace was operated at 100% of its rated power which reduced the useful lifetime of the lamps to several hours and made the duration of experiments unpredictable. Under these operating conditions the calculated heat losses from the furnace to the cooling water amounted to about 24,000 W, or half of the power output of the lamps, which consequently limited the charge temperature to 1473 K.

The upper temperature limit was also affected by the surface emissivity of the crucible holding the charge material. An iron block heated in an alumina crucible sheathed in stainless steel reached a temperature 30 K - 40 K higher than what was possible in an unsheathed crucible. This observation stemmed from an increase in the total, normal surface emissivity of the crucible surface from about 0.4 for alumina to 0.8 for the oxidized stainless steel sheath at 1473 K<sup>103</sup> (see Figure 16).

At the elevated test temperatures the alumina fiberboard used to insulate the furnace degraded and released oxide particulates which deposited onto the lamps and reflectors. Disassembly of the heating unit was then required after each experiment to polish the reflectors to a mirror finish so as to maintain maximum heating efficiency in the furnace.

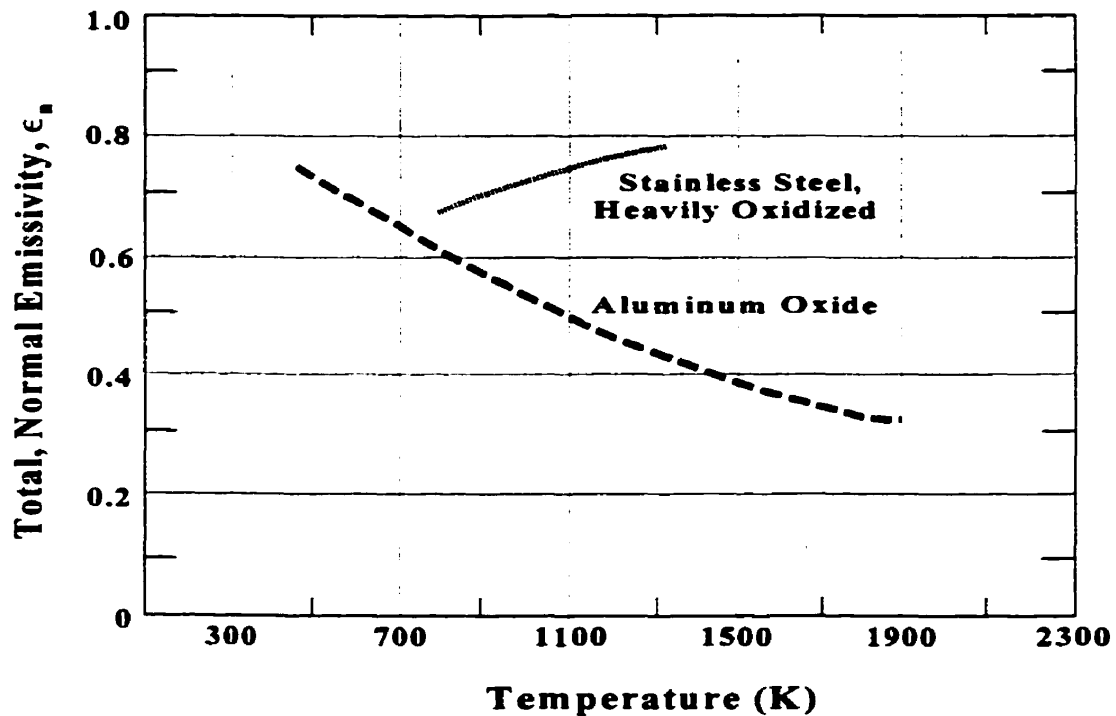


Figure 16. Temperature versus total, normal emissivity of heavily oxidized stainless steel and aluminum oxide<sup>103</sup>.

### *Silicon Carbide Resistance Heating Furnace*

Following a major failure of the clamshell heater, a resistance furnace using silicon carbide (SiC) heating elements was designed and built at McGill University. Six cylindrical SiC elements (OD = 0.0254 m  $\times$  overall length = 0.914 m) each with a heated length of 0.5 m were aligned horizontally in a furnace chamber (inner volume of 0.11 m<sup>3</sup>) which was constructed from silica bricks and insulated on the exterior with alumina-silicate fiberboard followed by a thin layer transite board (see Figure 17). The furnace assembly was enclosed in a cubical frame made of slotted steel angle which was fastened with bolts and reinforced at each corner with gusset plates.

The SiC heating rods were arranged in two opposing sets of three elements to create a heating zone 0.284 m wide and 0.152 m high. Connected in a 3-phase, wye-series configuration with a voltage drop of 208V across each phase, the elements yielded a combined power output of 18,000 W.

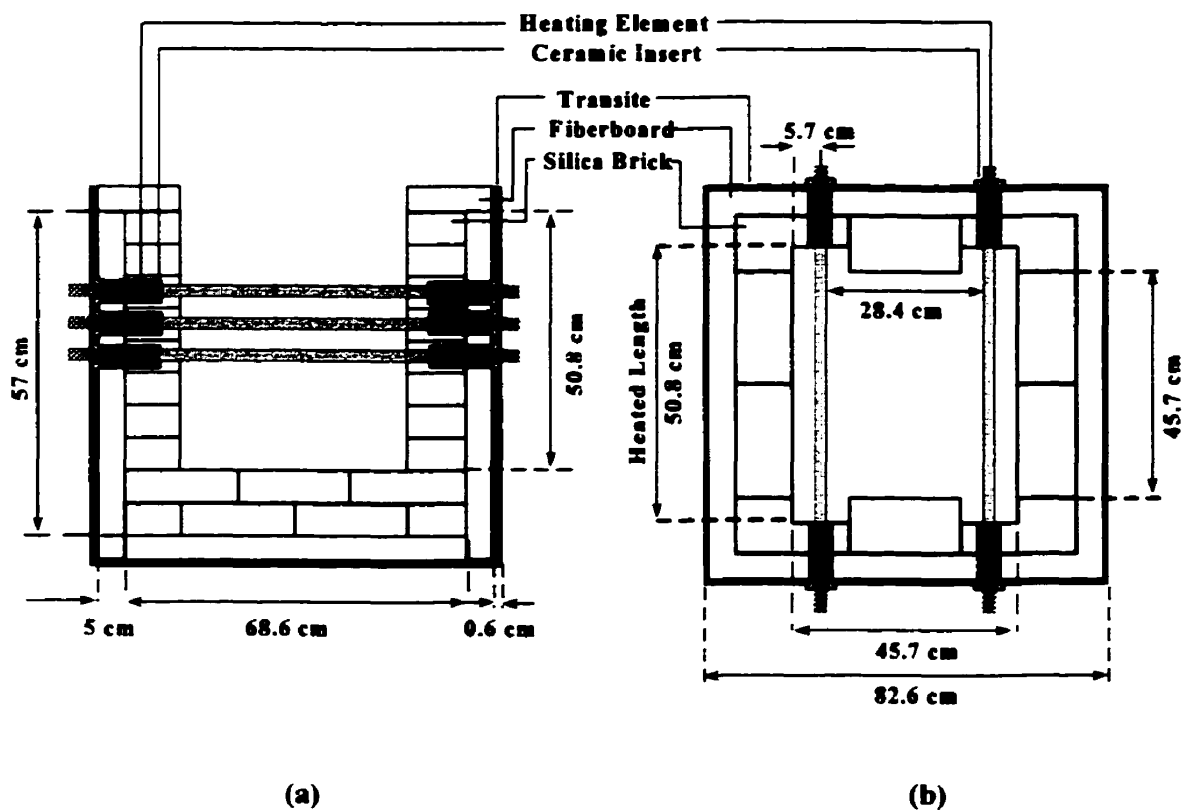
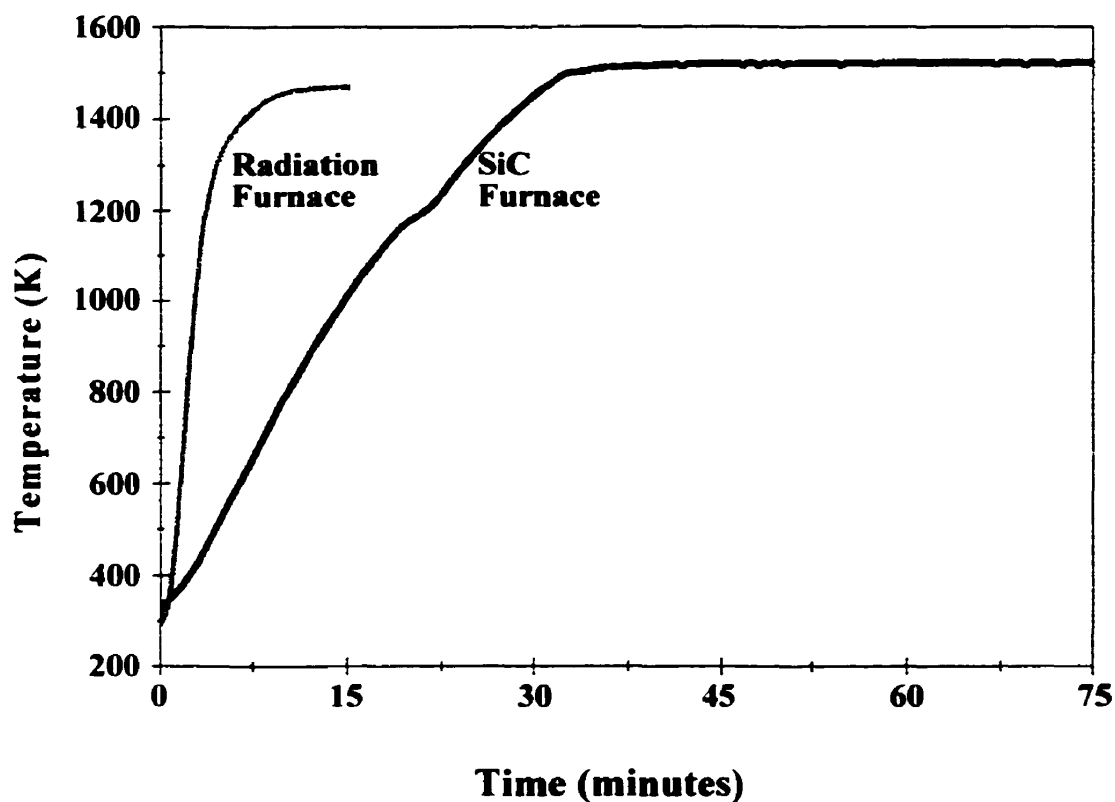


Figure 17. Schematic representation of the (a) profile and (b) plan view of the silicon carbide resistance furnace designed and used in this investigation.

Although heating was less rapid with the SiC furnace than the clamshell furnace this deficiency was compensated by the former's ability to reach a higher melt temperature and maintain it with greater control over a prolonged period (see Figure 18). High temperature stability was accomplished with two Omega model CN9111 controllers connected in series and attached to individual R-type thermocouples immersed in the melt and placed behind a heating element (see Figure 19). With upper limits of the element and bath controllers set respectively at 1623 K and 1523 K, power delivery to the furnace was at first regulated by the element controller but as the melt approached the setpoint temperature this function was assumed by the bath controller.

Due to the modular design of the SiC furnace it was possible to increase the power of the furnace by inserting additional elements into the heating chamber and to replace any failed individual components without any major disassembly of the heating unit.



**Figure 18.** The time-temperature profiles of an iron block heated to 1473 K in the clamshell radiation furnace and to 1523 K in the SiC resistance furnace.

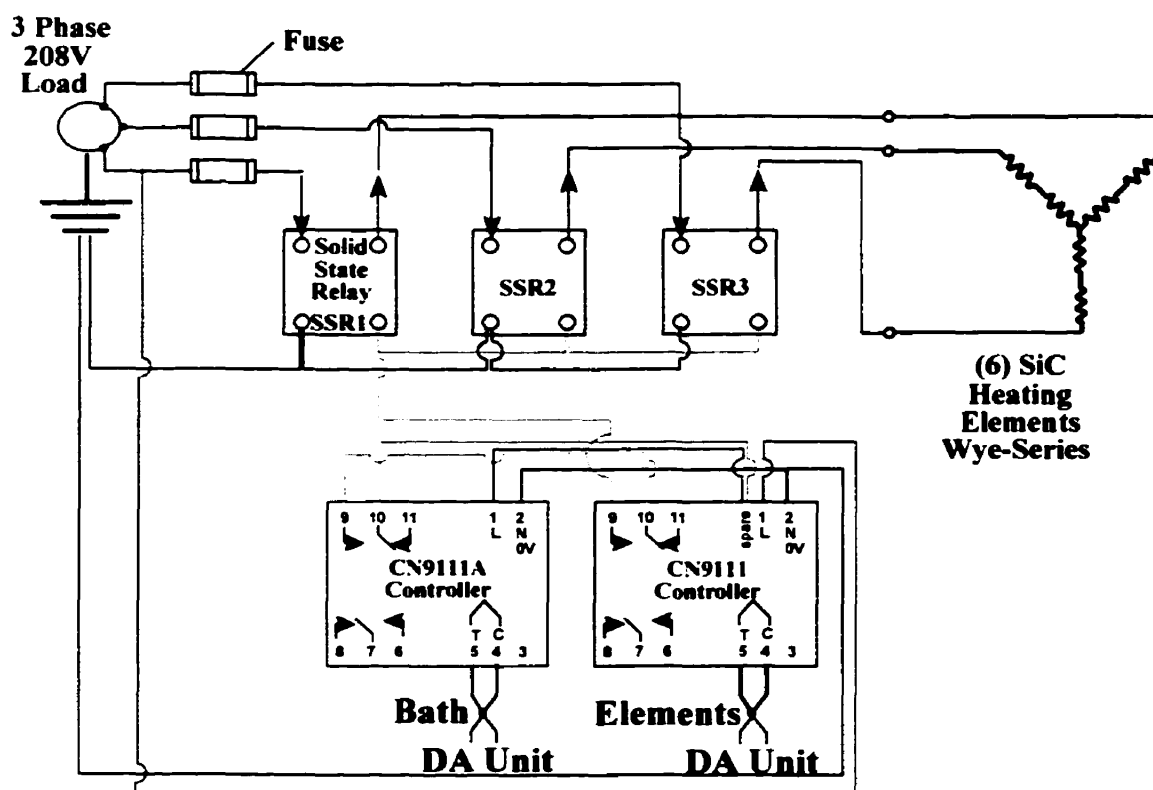


Figure 19. Wiring diagram for the SiC resistance furnace featuring two Omega CN9111 series controller which allowed for high thermal stability in the bath.

### 3.2.3. Reaction Vessel

Cathode copper or copper alloy contained in an alumina crucible was inserted into a transparent, cylindrical quartz tube which was sealed on one end with a full radial bottom. The open end of the tube was made gas-tight with an annular, water-cooled top constructed of aluminum that had viton o-rings embedded in its interior wall (see Figure 20(a)). On the horizontal surface of the cooling jacket (see Figure 20(b)) a number of access ports equipped with swagelok fittings accommodated a gas lance, an exhaust tube, a thermocouple, an oxygen probe, a sampling tube, and a quartz window (see Table 2 for the dimensions of the reaction vessel and its accessories).

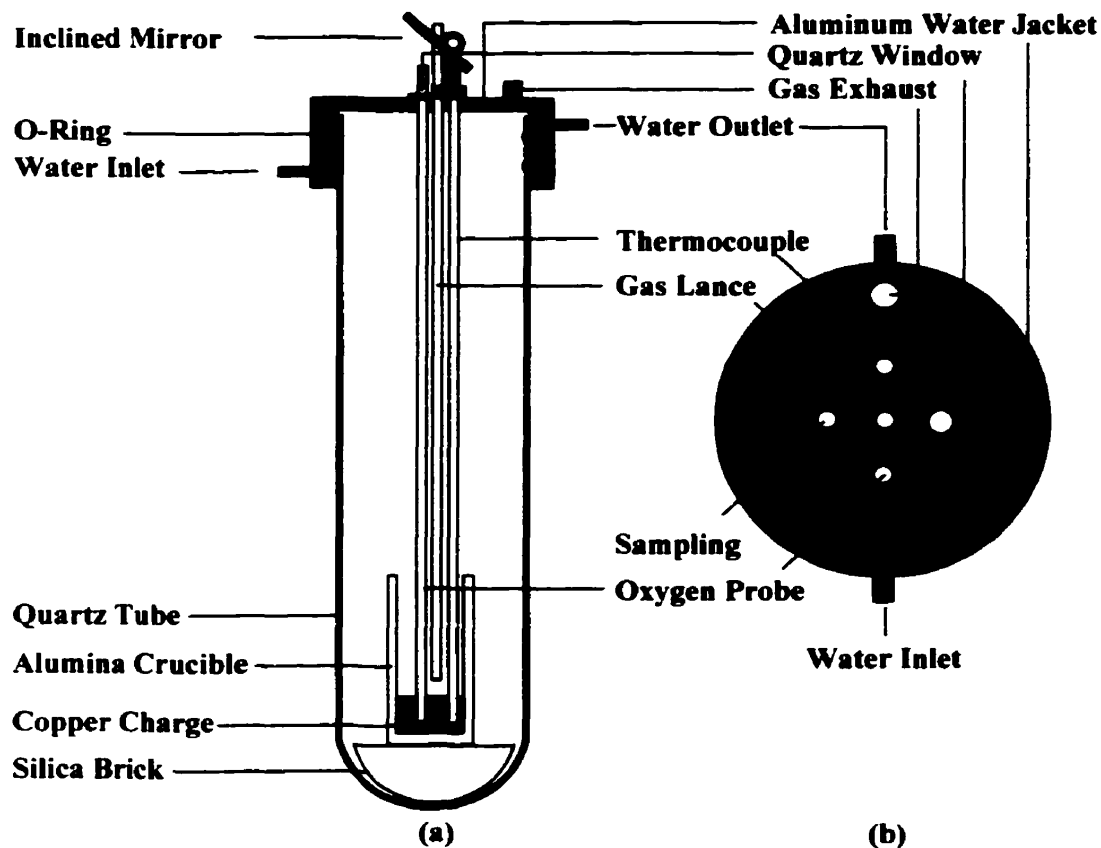
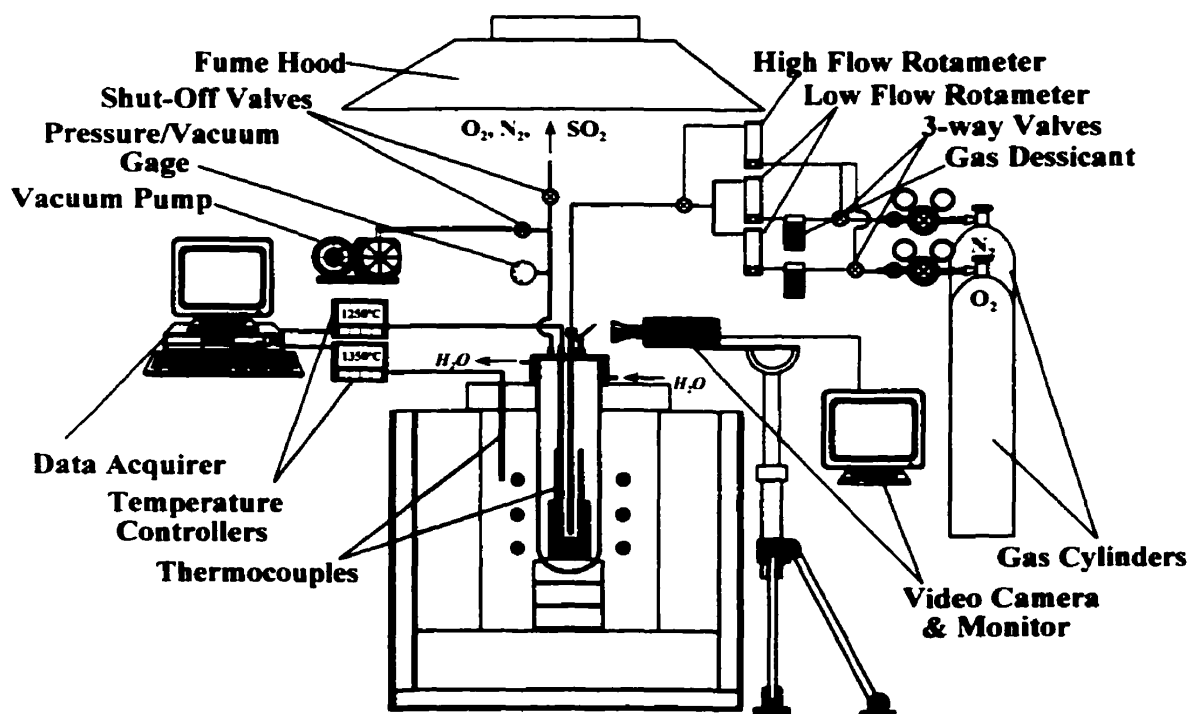


Figure 20. Schematic representation of the (a) cross section of the reaction vessel, crucible and accessories and (b) plan view of the Al water jacket and its access ports.

Table 2. Dimensions of the reaction vessel and its accessories.

Item	ID m (mm)	OD m (mm)	Length/Height m (mm)
Hycor Al <sub>2</sub> O <sub>3</sub> Crucible	0.07 (70)	0.08 (80)	0.15 (152)
High Density Al <sub>2</sub> O <sub>3</sub> Crucible	0.068 (68)	0.072 (72)	0.148 (148)
Quartz Reaction Vessel	0.155 (155)	0.161 (161)	0.61 (610)
Aluminum Water Jacket	0.165 (165)		
Mullite Gas Lance	0.006 (6.4)	0.01 (9.5)	0.61 (6.1)
R-type T/C with Sheath	-	0.01 (9.5)	0.61 (6.1)
Flexible Exhaust Tube	0.008 (7.94)	0.013 (12.7)	variable
Quartz Sampling Tube(s)	0.003 (3)	0.005 (5)	variable
Quartz Window	-	0.013 (12.7)	-

A mullite lance supplied inert gas to the reaction vessel during alloy melting and later introduced O<sub>2</sub>-N<sub>2</sub> gas mixtures onto the melt surface for either oxygen dissolution and/or desulfurization. Prior to melting of the alloy a flexible exhaust tube in conjunction with a vacuum pump evacuated the reaction vessel of air but in the heating stage served to vent the effluent gases. An R-type thermocouple sheathed in alumina was immersed into the melt and regulated the bath temperature while a submerged oxygen probe monitored dissolved oxygen levels in the alloy. Both the thermal and oxygen level readouts of the bath were recorded by a data acquisition unit over the duration of the experiment. Quartz tubes inserted through the sampling port withdrew copper samples from the melt by applying suction at the exposed end with a rubber bulb pump. The quartz window, in addition to the transparent walls of the reaction vessel, permitted visual observation of the melt surface. A mirror positioned above the quartz window at a 45° inclination to the horizontal plane reflected the image of the melt surface into the lens of a video camera that was close-circuited to a television monitor. The complete test apparatus is shown in Figure 21 and Figure 22.



**Figure 21. Schematic representation of the test apparatus when the quartz reaction vessel and graphite receptacle were used.**

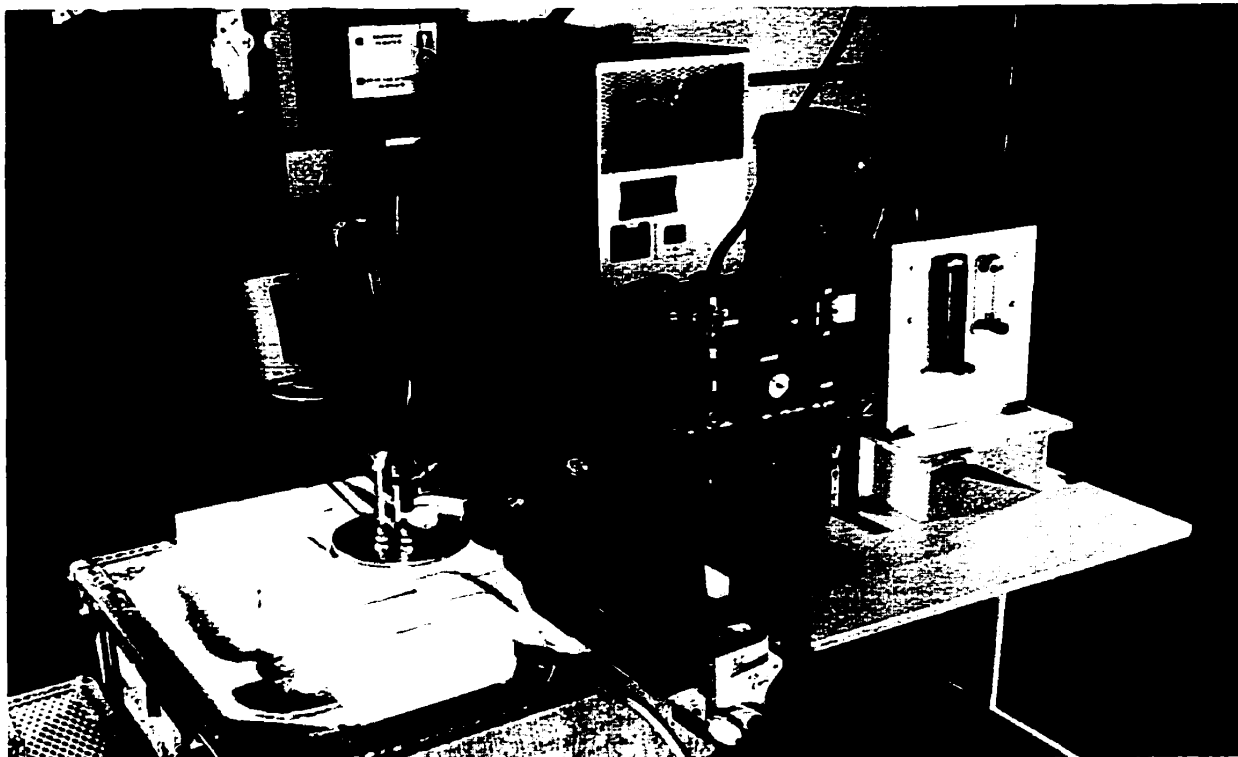


**Figure 22. Photograph of the test apparatus during operation.**

Corrosive attack of the experimental equipment by molten copper oxide precipitated several modifications to the test apparatus. HYCOR alumina crucibles used initially for containing the alloy charge were replaced with high density alumina crucibles due to the permeability of the former to copper oxide. The susceptibility of the high density crucibles to thermal and physical shock required that they be placed in a graphite receptacle (Test 3 to Test 6) in case of failure. Surface eruptions from the melt necessitated an extension to the crucible wall to prevent contact and subsequent reaction of melt droplets with the quartz tube. On-line monitoring of the oxygen levels was abandoned after the second test because of electronic noise in the oxygen readings and the vulnerability of the probes to corrosive attack by the melt.

The test apparatus was again altered in later tests (Test 7 to Test 9) because of the low sulfur elimination observed in preceding experiments. This effect was attributed partly to a reduced oxygen potential in the gas phase resulting from the oxidation of the graphite

crucible to carbon monoxide. The quartz reaction vessel was dropped from use in preference of the charge being melted in the open atmosphere while the aluminum water jacket remained as a support for the gas lance, thermocouple and mirror. The use of HYCOR alumina crucibles was resumed due to their lower cost and greater durability while the graphite receptacle was replaced with a larger HYCOR alumina crucible (ID  $\times$  OD  $\times$  L = 0.14 m  $\times$  0.167 m  $\times$  0.22 m) that was partially filled with silica sand to contain copper spills.

### **3.2.4 Gas Regulation System**

#### **Gas Evacuation/Ventilation**

The exhaust tube of the cooling jacket was connected in parallel to a ventilation hood, a vacuum pump and a pressure gauge as shown in Figure 21 and Figure 22. Air was evacuated from the tube prior to heating by shutting the flow line to the ventilation hood and engaging the rotary vacuum pump until the pressure in the quartz vessel had dropped to  $10^{-4}$  to  $10^{-5}$  atmosphere. The vacuum line was then closed, the pump was disengaged and the evacuated reaction vessel was then backfilled with nitrogen. When the heating cycle was initiated the ventilation line was opened and the heated gases exited into the fume hood.

#### **Gas Delivery**

Gases from the nitrogen and oxygen cylinders were directed by individual two-way valves to either a high flowrate rotameter or to a drying cylinder leading into a low flowrate rotameter. The gases exiting the low flow rotameters were regulated with precision metering valves and then mixed in the desired proportions upon exiting the flowtubes before being channelled into the gas lance above the melt.

## **3.3 Experimental procedure**

### **Test 1 - Test 6**

Prior to melting of the charge, water flow to the cooling jacket was set at 125-160 cm<sup>3</sup>/s and the reaction vessel was either evacuated and backfilled with ultra-high purity N<sub>2</sub> five times or continuously flushed with nitrogen until seven reactor vessel volumes were displaced. Upon completion of this cycle the data acquirer was activated and power was

delivered to the furnace. As the charge was heated, the reaction vessel was continuously supplied with nitrogen at a rate of 50-80 cm<sup>3</sup>/s while the exhaust port was left open to accommodate for the expansion of the heated gas. At the setpoint temperature of 1523 K, two or three samples were extracted from the melt to provide a reference composition for O, S and Ni at the start of the experiment. After the initial samples were taken, top-blowing with an O<sub>2</sub>-N<sub>2</sub> gas mixture and video recording of the melt surface was initiated. The melt was then sampled at intervals of 10 to 15 minutes for the duration of the test (90 to 240 minutes).

### ***Test 7 - Test 9***

The charge was melted in the furnace chamber under a fumehood and exposed to the open atmosphere. When the alloy had liquified samples were extracted for a period of 160 minutes in Test 7, 135 minutes in Test 8 and 90 minutes in Test 9 while the charge was exposed to air. In each test oxygen was top-blown onto the melt at 75 cm<sup>3</sup>/min for approximately 50 minutes with continued sampling of the melt. In Test 9 the melt was subjected to a stage of submerged nitrogen injection at 2000 cm<sup>3</sup>/min.

### ***3.4 Elemental Analyses***

Elemental analysis for sulfur and oxygen in the copper alloys and test samples were conducted by the Technical Services department at INCO's Copper Cliff Smelter while nickel determinations were performed at the Department of Mining and Metallurgical Engineering of McGill University.

Sulfur analysis was determined with a Leco IR 332 combustion analyzer in which a copper sample weighing 0.1g to 1 g was induction melted in a red heat environment in the presence of oxygen and an iron accelerator. The resulting oxygen and sulfur dioxide stream was delivered to an infra-red detector that quantified the sulfur content of the copper sample. The accuracy of the detector under normal operating conditions was stated to be  $\pm 2\%$ , or 1 standard deviation. The unit was calibrated twice with an iron standard of known sulfur composition prior to the commencement of analysis and was recalibrated after 10 to 20 analyses had been performed.

Oxygen analysis of the copper samples was performed with a Leco RO 116 analyzer in which a copper sample of mass 0.1 g to 1.0 g was placed in a graphite crucible and combusted in an electrode furnace in the presence of nitrogen. The oxygen in the copper after having reacted with the carbon in the crucible to produce carbon monoxide gas ( $\text{CO}_{(g)}$ ) was carried by the nitrogen stream to an infra-red cell which quantified the oxygen level of the copper sample through an evaluation of the  $\text{CO}_{(g)}$  concentration in the gas stream. The accuracy of the analyzer was similarly rated at  $\pm 2\%$ , or 1 standard deviation, and calibration was carried out at the same frequency as with the S analyzer.

The quantification of nickel levels in the copper samples was evaluated with an Elmer Atomic Absorption Spectrometer Model 3110. A copper sample of approximately 0.1 g was dissolved in an acid solution consisting of 10  $\text{cm}^3$  of hydrochloric acid and 5  $\text{cm}^3$  of nitric acid. The copper-acid solution was diluted in a 500  $\text{cm}^3$  flask with distilled water which was then aspirated into the AA unit and burned in the presence of an acetylene/air flame. The nickel composition of the copper was then correlated to the absorbance of the flame as established through a series of standard solutions of known nickel compositions.

### **3.5 Charge Preparation**

INCO semi-blister copper from the MK flash reactor analyzes at 2-3 wt % S and 3-5 wt % Ni. To reduce the time of the laboratory-scale experiments, the initial sulfur content of the Cu-S and Cu-Ni-S alloys was lowered to 1 wt % and the nickel content in the Cu-Ni-S alloy was reduced to 3 wt %. Thus, while oxidation experiments were performed on cathode copper, desulfurization tests were carried out on two copper alloys: Cu - 1 wt% S and Cu-3 wt % Ni - 1 wt% S which were respectively designated CS and CNS alloys.

Experimental alloy charges were prepared from cathode copper sheet (0.70 m  $\times$  0.80m  $\times$  0.01m) supplied by INCO in addition to -100 mesh nickel (Ni) powder (99.99 wt % purity) and -325 mesh copper(I) sulfide ( $\text{Cu}_2\text{S}$ ) powder (99+ wt % purity) purchased from Sigma-Aldrich. The  $\text{Cu}_2\text{S}$  powder analyzed by Sigma-Aldrich at 76.2 wt % Cu and 23.4 wt % S indicated an excess of sulfur with respect to the stoichiometric compound. The

composition of the cathode copper (see Table 3) was determined by emission spectroscopy and was performed on 10 regions selected randomly across the cathode sheet (see Figure 23). Each elemental assay was derived from 30 determinations i.e. 3 assays from each of the 10 surveyed areas.

**Table 3. Average elemental composition of INCO cathode copper sheet.**

Element	Composition <sup>*</sup> (wt %)	Element	Composition <sup>*</sup> (wt %)
Ni	0.04795 ± 0.0153	Sn	0.0037 ± 0.0018
Co	0.01903 ± 0.0033	Mn	<0.0040
Si	0.0126 ± 0.00047	Cd	<0.0017
P	0.0122 ± 0.00084	Al	<0.0008
Mg	0.00833 ± 0.0025	Bi	<0.0008
Fe	0.0079 ± 0.0018	S	<0.0004

<sup>\*</sup>Standard deviation calculated on the basis of the population.

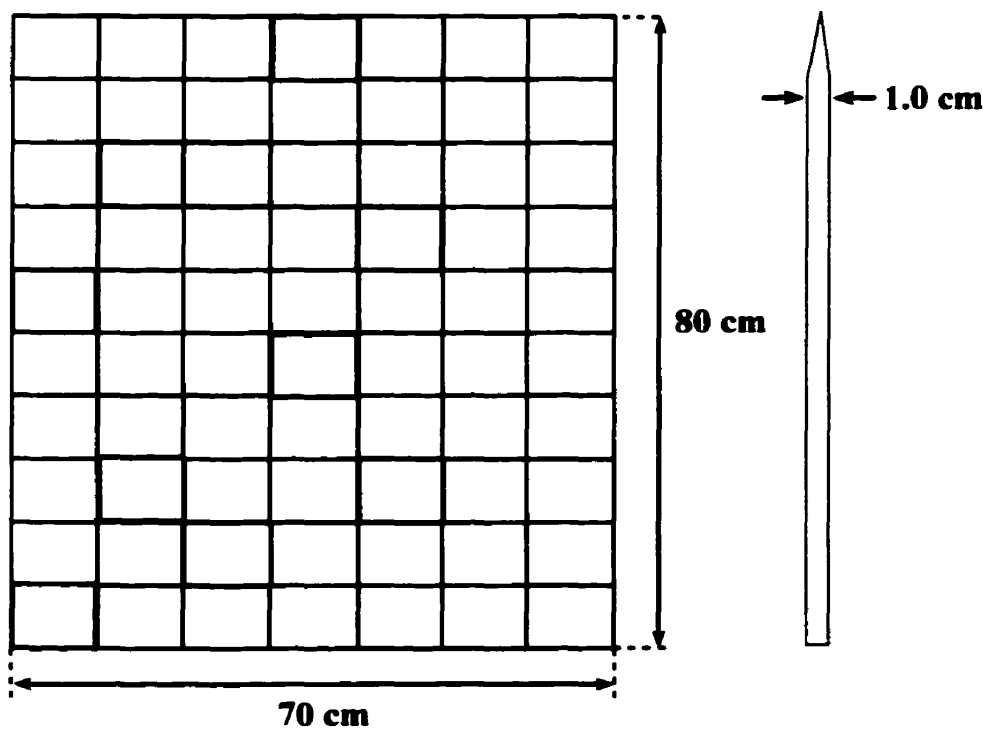


**Figure 23. Broadside and cross section of the cathode copper sheet. Elemental analyses were performed on the shaded regions.**

### 3.5.1 In Situ Alloy Preparation

Preparation of a Cu-3 wt % S alloy was first attempted in a HYCOR alumina crucible by heating measured amounts of cathode copper and  $\text{Cu}_2\text{S}$  powder under U.H.P.  $\text{N}_2$  prior to desulfurization of the melt. In this experiment significant evolution of sulfur dioxide ( $\text{SO}_2$ ) gas occurred during the alloy preparatory stage while the formation of a viscous secondary phase was observed on the melt surface after oxygen blowing had commenced. The measured sulfur content in the melt at the start of oxygen blowing had dropped to approximately 1 wt% as a result of the initial  $\text{SO}_2$  evolution while the frozen slag layer, at 1.5 cm thickness (see Figure 24) was considered to be the reaction product of the molten charge with components or impurities of the crucible. The crucible composition (see Table 4) consisted predominantly of alumina at 88.3 wt % followed by silica at 11.2 wt % and minor amounts of other oxides. However a qualitative analysis of the slag phase by X-ray diffraction (see Appendix A) detected the presence of amorphous copper oxides ( $\text{CuO}$  and



Figure 24. Cross section of crucible and solidified slag layer from Test 1.

Cu<sub>2</sub>O) and some Cu<sub>2</sub>S but not of any crucible compounds. From these analytical results the slag layer was believed to have formed by the oxidation of the Cu<sub>2</sub>S powder and therefore in situ alloy preparation was abandoned after the first desulfurization test. Alloy charges used in subsequent tests were taken from master alloys that had been prepared in advance.

**Table 4. Composition of HYCOR alumina crucible according to the manufacturer..**

Compound	Composition (wt %)	Compound (As Impurity)	Composition (wt %)
Al <sub>2</sub> O <sub>3</sub>	88.3	TiO <sub>2</sub>	0.10
SiO <sub>2</sub>	11.2	K <sub>2</sub> O	0.03
Fe <sub>2</sub> O <sub>3</sub>	0.15	MgO	0.03
NaO <sub>2</sub>	0.12	CaO	0.02

### **3.5.2 Master Alloy Preparation**

Two copper alloys at 1 wt% S (CS alloy) and 3 wt % Ni - 1 wt % S (CNS alloy) were prepared through induction melting of cathode copper and Cu<sub>2</sub>S powder, and Ni powder (for the CNS alloy) in a sealed, cylindrical graphite crucible (OD x ID x Height = 9.2 cm x 7.7 cm x 19.1 cm). The proportions of the alloy feed materials were determined by a mass balance of the elements where it was assumed that metallic losses were negligible and sulfur recovery was 90 wt %.

The sealed crucible was inserted into the induction furnace chamber and packed with coarse silica granules to minimize oxidation of the graphite with the outside atmosphere. A removable centerpiece on the lid of the crucible allowed the charge to be monitored periodically as it was heated. Upon liquefaction, the charge was kept molten for roughly 40 minutes to allow adequate time for dissolution of the powdered material and homogenization of the melt. Power delivery to the induction coils was then suspended and the alloy was left to cool and solidify in the crucible. The resulting cylindrical ingot was removed, massed and then sandblasted to remove any foreign and oxide particulates from its exterior surfaces. The ingot was sectioned along its vertical axis and drill samples were extracted from four regions (see Figure 25) for O, S and Ni determinations (see Table 5).

Table 5. Elemental determinations for CS and CNS alloys.

Sampled Region	CS Alloy		CNS Alloy		
	O (wt %)	S (wt %)	O (wt %)	S (wt %)	Ni (wt %)
1	0.001	0.82 ± 0.01	0.046	1.23	2.86 ± 0.162
2	0.006	0.838	0.023	1.11	2.85 ± 0.085
3	0.024	0.80 ± 0.015	0.011	1.08	3.22 ± 0.106
4	0.024	0.80 ± 0.011	0.017	1.24	3.14 ± 0.240
<b>Average</b>	<b>0.014 ± 0.010*</b>	<b>0.81 ± 0.012*</b>	<b>0.024 ± 0.013*</b>	<b>1.17 ± 0.071*</b>	<b>3.02 ± 0.20*</b>

\*Standard deviation calculated on the basis of the sample population

\*Standard deviation calculated on the pooled average from the deviation of each analysis which is based on two determinations per region

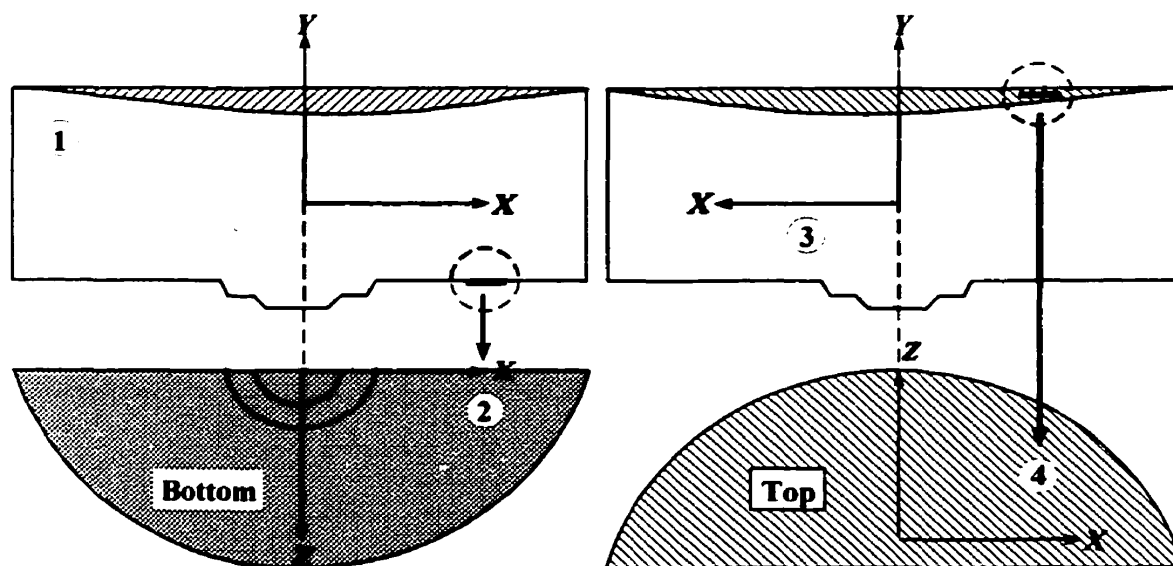


Figure 25. Regions of alloy ingot sampled for elemental determinations.

### ***3.6 Selection of Experimental Conditions***

Nine experiments were performed at 1523 K<sup>+</sup> to investigate the effect of gas flowrate,  $P_{O_2}$  of the gas stream and the presence of nickel in the melt on desulfurization (see Table 6). The test conditions were selected on the basis of prior works and from the observations made in each test.

The gas flowrates used in the testwork were initially selected to result in low momentum gas streams, which, upon impingement on the melt surface, would not appreciably stir the bath or influence the occurrence of surface tension driven flow. Due to the similarity in the kinematic viscosities of water and liquid copper it was assumed that a water model of the system could provide a reasonable assessment of the level of stirring attributed to the momentum of the gas stream. Water soluble food dye was introduced under the gas stream and its dispersion was observed under the various gas flowrates. It was found that at an air flowrate of 100-200 cm<sup>3</sup>/min no appreciable mixing of the food dye occurred.

Tests 1 through 3 were performed using the copper-sulfur alloy under different gas flowrates and compositions in order to determine the effect of these variables on the rate of desulfurization. Tests 3 through 6 were conducted under similar conditions with different alloy charges although the gas flowrate was increased in the later stages of Tests 4, 5 and 6.

a comparison was drawn between the desulfurization rates of the copper-sulfur (CS) alloy used in Test 3 and the copper-nickel-sulfur (CNS) alloy used in Test 4. a further evaluation was made of the dissolved oxygen levels in these alloys which were contrasted against that for cathode copper (Test 5 and Test 6).

The samples of Test 5 were not assayed on account of the failure of the crucible containing the copper charge. The final tests in the experimental program (Tests 7 through 9) were designed to assess desulfurization under conditions where the two alloy charges were melted under air. Reproducibility of the testwork was also verified through Test 7 and Test 8 which were carried out with a CS alloy charge under the same experimental conditions.

---

<sup>+</sup>The setpoint temperature in Test 1 was lowered to 1498 K because the melt temperature according to the data acquirer readings had exceeded 1550 K.

**Table 6. Experimental conditions used for desulfurization and oxidation tests.**

Test	Melt Temp. K	Alloy/ Charge	Charge Mass (g)	Stage	Gas Flowrate (cm <sup>3</sup> /min)	Lance Position <sup>♦</sup> (cm)	$\mathcal{P}_{O_2}$ (atm)	$\mathcal{P}_{N_2}$ (atm)
1 <sup>†</sup>	1498	CS	1998	I	169.4	1.5	0.62	0.38
2	1573	CS	1014.5	I	131	1.5	0.50	0.50
3 <sup>*</sup>	1573	CS	1009.4	I	75	1.5	1	-
4 <sup>*</sup>	1573	CNS	1092.9	I	75	1.5	1	-
				II	372		1	-
5 <sup>*</sup>	1573	C.Cu	1011.3	I	75	1.5	1	-
				II	372		1	-
6 <sup>*</sup>	1573	C.Cu	1068.2	I	75	1.5	1	-
				II	372		1	-
7 <sup>**</sup>	1573	CS	830.7	I	Air		0.21	0.79
				II	75	1	1	-
8 <sup>**</sup>	1573	CS	891.0	I	Air		0.21	0.79
				II	75	1	1	-
9 <sup>**</sup>	1573	CNS	1035.0	I	Air		0.21	0.79
				II	75	1	1	-
				III	2000	-1	-	1

<sup>†</sup>In situ alloy preparation of a Cu - 3 wt% S alloy  
<sup>††</sup>Graphite receptacle used as spill container  
<sup>†††</sup>Charges melted under an open atmosphere and consequently no flowrate is stated in Stage I.  
<sup>♦</sup>Distance of the lance tip from the melt surface.

### 4.1 Experimental Results

#### Test 1: Desulfurization of a Cu - 3 wt% S Alloy

The first test of the experimental program attempted to produce a copper alloy of 3 wt % S, in situ, by melting 0.3 kg (302.0 g) of Cu<sub>2</sub>S powder and 1.7 kg (1696.0 g) of cathode copper in a HYCOR alumina crucible under nitrogen gas and subsequently desulfurize this alloy at 1523 K<sup>‡</sup> with an O<sub>2</sub>-N<sub>2</sub> gas mixture. During liquefaction of the alloy components, much sulfur was evolved from the melt as was evident by a strong odour of SO<sub>2</sub> in the off-gas from the reaction vessel and this was confirmed by the initial melt analysis of 1.21 wt % S. Oxygen-nitrogen gas injection for 71.5 minutes at 170.6 cm<sup>3</sup>/min and  $\mathcal{F}_{O_2} = 0.62$  decreased the sulfur content of the melt by a further 10 % to 1.07 wt % S while the dissolved oxygen concentration increased by an order of magnitude from 0.02 wt % to 0.11 wt % (see Table 7 and Figure 26).

Table 7. Tabulated S and O assays from Test 1 conducted at 1498 K by blowing an O<sub>2</sub>-N<sub>2</sub> gas mixture with  $\mathcal{F}_{O_2} = 0.62$  at 170.6 cm<sup>3</sup>/min on liquid Cu - 3 wt% S alloy.

Sampling Time minutes	[S] wt %	[O] <sup>M</sup> wt %	Experimental Condition
0.00	1.21 ± 5 e-5	0.020 ± 0.005	Melt Homogenization
10.5	--	--	O <sub>2</sub> introduced at 105.6 cm <sup>3</sup> /min
22.3	1.17 ± 0.0121	0.050 ± 0.009	O <sub>2</sub> blown at 105.6 cm <sup>3</sup> /min
38.6	0.975 ± 5 e-3	0.085 ± 0.012	O <sub>2</sub> blown at 105.6 cm <sup>3</sup> /min
55.3	1.12	0.126 ± 0.009	O <sub>2</sub> blown at 105.6 cm <sup>3</sup> /min
71.7	1.09	0.0941	O <sub>2</sub> blown at 105.6 cm <sup>3</sup> /min
81.0	1.07	0.11 ± 0.027	O <sub>2</sub> blown at 105.6 cm <sup>3</sup> /min
Pooled Std. Deviations	9.3 e-3	7.5 e-3	

<sup>M</sup>Oxygen assays performed at McGill University

Visual recording of the melt surface was terminated less than 10 seconds after the start of oxygen blowing due to the failure of the heat shield in front of the video camera. This brief record of the melt surface showed a luminescent patch beneath the tip of the gas lance (see Figure 27) but contrary to reports of Marangoni convection in copper melts<sup>72,89,91</sup>,

<sup>‡</sup> The bath controller setpoint was lowered to 1498 K because the output temperature from the data acquirer was often in excess of 1550 K (see Figure 29).

it did not spread radially outwards at high velocity; instead some material was ejected from this region. Inspection of the quartz reaction vessel at experiment's end revealed fine particles uniformly distributed in a circular band (see Figure 28) near the sealed radial bottom of the quartz tube; along the horizontal tube length the distribution pattern and size of the particles was more randomized. In some regions large droplets of ejected material ( $\sim 0.5$  cm) caused fractures along the vertical length of the quartz tube.

Following several minutes of  $O_2-N_2$  gas blowing a slag layer formed on the melt surface which thickened over time and eventually enveloped the tip of the gas lance. Upon melt solidification this layer measured 1.5 cm in thickness (Figure 24 in Chapter 3) while X-ray diffraction determined that it consisted mostly of  $Cu_2O$ ,  $CuO$  and some  $Cu_2S$ . Penetration of the crucible wall by copper oxide resulted in contact between the melt and the radial bottom of the reaction tube leading to its failure and termination of the experiment.

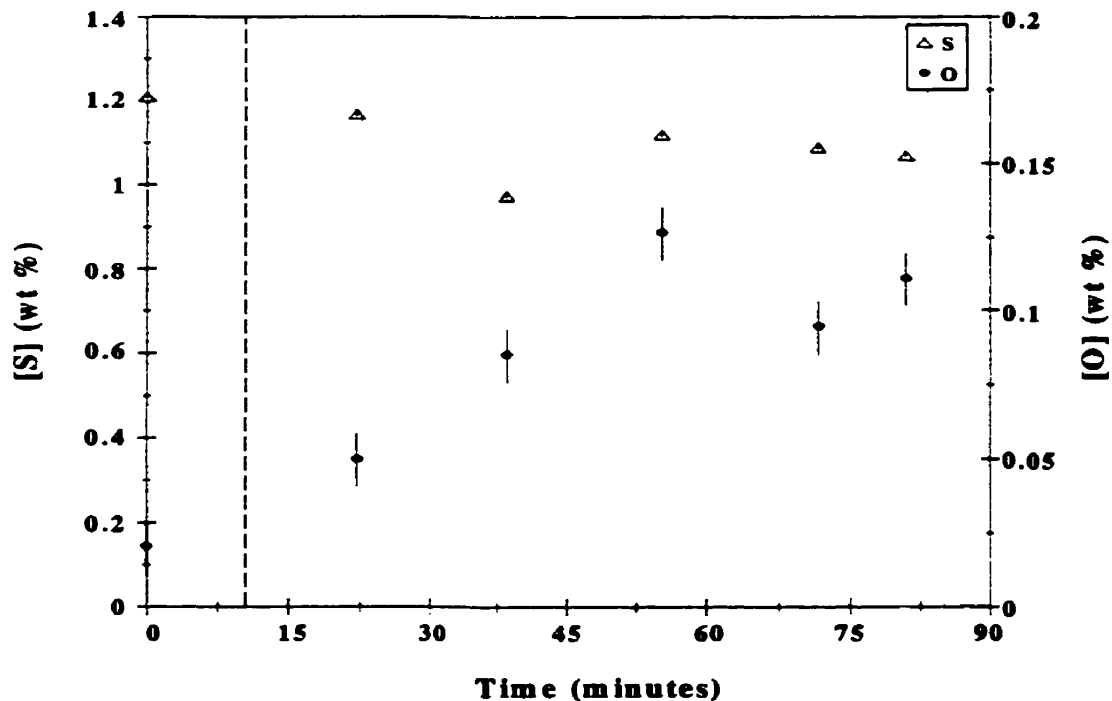


Figure 26. The dissolved S and O concentration profile over time in Test 1. The vertical line coincides with the introduction of the  $O_2-N_2$  gas mixture onto the melt surface at  $170.6 \text{ cm}^3/\text{min}$  and  $\mathcal{P}_{O_2} = 0.62$ .



Figure 27. Photograph of the luminescent patch beneath the tip of the gas lance in Test 1 at the start of  $O_2$ - $N_2$  gas blowing. The dark spot on tube is a large droplet of material that had been ejected from the bath.

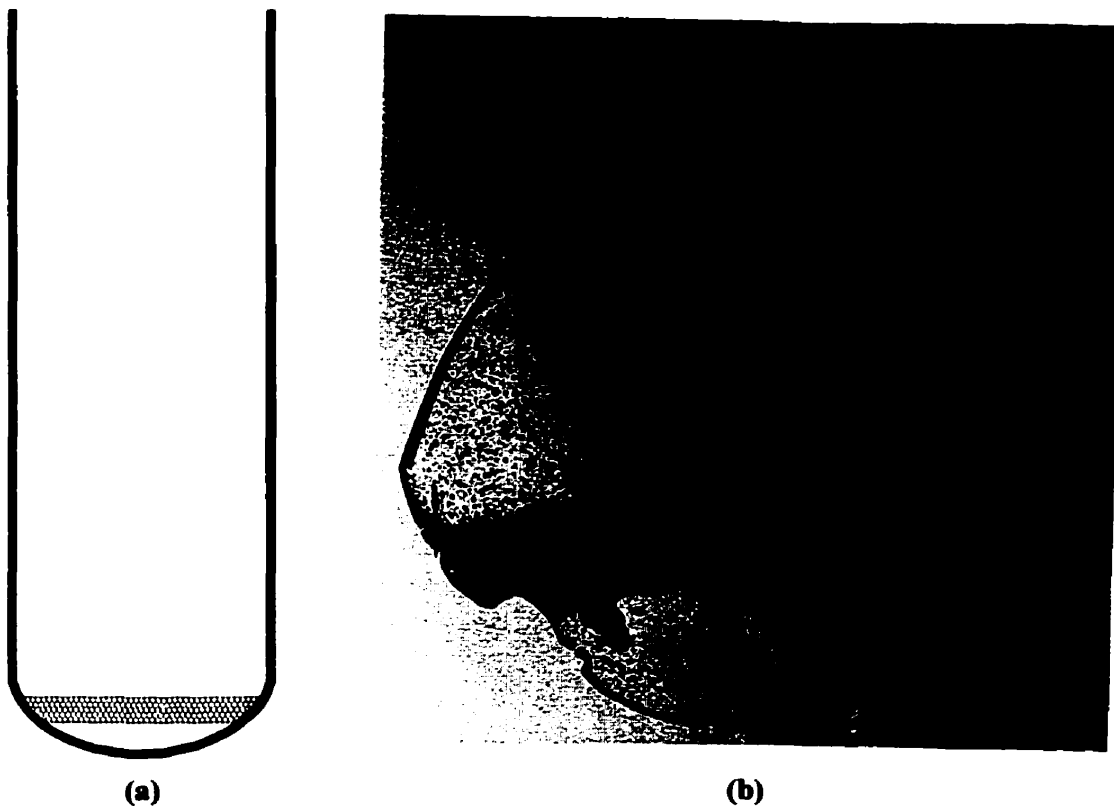


Figure 28. (a) Schematic of the region on the quartz tube most affected by the melt ejections. (b) Photograph of the fractured reaction vessel near its radial bottom ringed with droplets of copper/copper oxide.

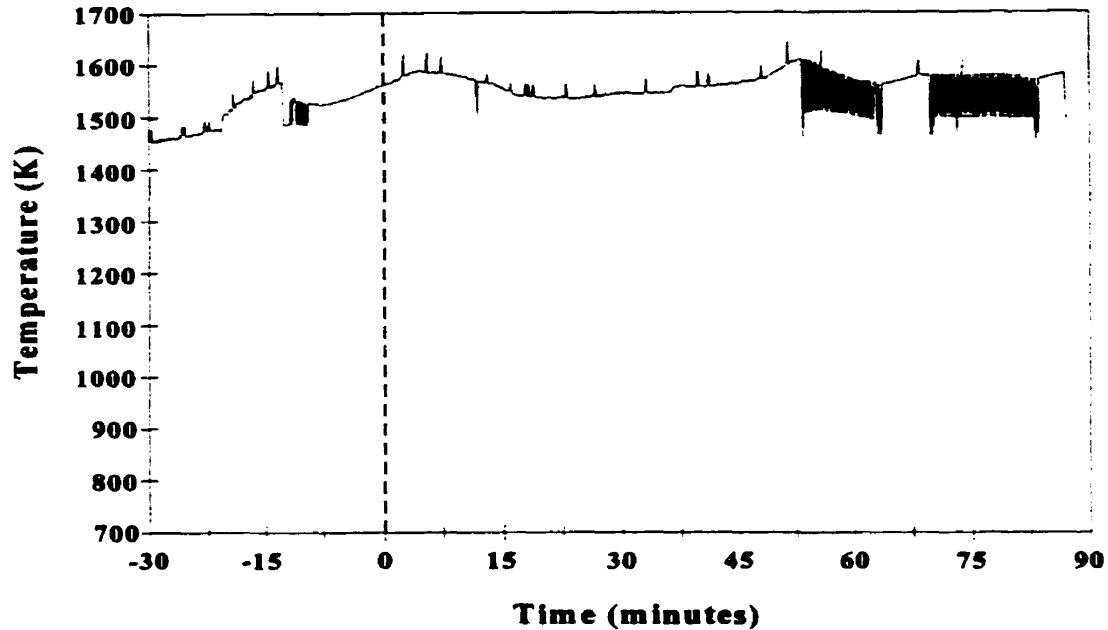


Figure 29. The time-temperature profile of the alloy melt in Test 1 relative to the sampling time. The horizontal line marks the bath setpoint temperature of 1498K. The data during melting of the alloy charge could not be retrieved from the DA unit.

### ***Test 2: Desulfurization of Cu - 1 wt % S Alloy with 66 cm<sup>3</sup> O<sub>2</sub>/min***

Slag formation in Test 1 was initially attributed to the reaction of the melt with the porous crucible and to an excessive rate of oxygen delivery. Therefore in Test 2, a 1 kg (1014.5 g) section of CS master alloy was melted under nitrogen in a high density alumina crucible and the oxygen flowrate was reduced to 66 cm<sup>3</sup>/min while  $\mathcal{P}_{O_2}$  was increased to 1. At 1523 K pure oxygen was introduced onto the liquid alloy surface for 156 minutes. Under these blowing conditions the sulfur content of the bath was reduced to 0.62 wt % or by about 40 % (see Table 8 and Figure 30). The dissolved oxygen content increased from 0.23 - 0.47 wt % to a maximum level of 0.16 - 0.165 wt % (see Table 8 and Figure 30). An attempt to monitor the oxygen level in the bath with a submerged oxygen probe failed because the tip of the probe was consumed by the melt. Although the temperature readings from the data acquirer were often in excess of 1523 K (see Figure 31), the bath temperature controller consistently displayed 1523 K and therefore no changes were made to the setpoint temperature in the controller.

Throughout the experiment the melt surface remained free of the type of slag coverage observed in Test 1 and the characteristic dark surface of the liquid copper was clearly visible; however a thin, emissive, oxide film collected near the crucible wall (see Figure 32a) which after melt solidification appeared as darkened regions on the blistered copper surface (see Figure 32b). Some limited swirling motion of this film did take place but the flow pattern and velocity were not characteristic of Marangoni convection. The only surface phenomenon observed was some intermittent bubbling on the melt surface. As in Test 1, there was evidence of material ejection from the melt which appeared as finely dispersed droplets along the vertical length of the cooled reaction tube (see Figure 33). Despite using a high density alumina crucible, the container failed and its contents seeped onto the quartz reaction vessel resulting in irreparable damage to the tube.

**Table 8. Tabulated S and O assays from Test 2 conducted at 1523 K by blowing pure O<sub>2</sub> at 66 cm<sup>3</sup>/min on the surface of liquid CS alloy.**

Sampling Time minutes	[S] wt %	[O] wt %	Experimental Stage
0.00	1.03 ± 0.18	0.047 ± 0.024	Melt Homogenization
3.30	1.07 ± 0.19	0.023 ± 0.011	Melt Homogenization
6.77	--	--	O <sub>2</sub> introduced at 66 cm <sup>3</sup> /min
15.63	1.06 ± 0.014	0.05	O <sub>2</sub> blown at 66 cm <sup>3</sup> /min
29.73	0.99	0.11	O <sub>2</sub> blown at 66 cm <sup>3</sup> /min
41.40	0.97	0.1	O <sub>2</sub> blown at 66 cm <sup>3</sup> /min
45.57	0.92	0.064	O <sub>2</sub> blown at 66 cm <sup>3</sup> /min
71.40	0.93	0.068	O <sub>2</sub> blown at 66 cm <sup>3</sup> /min
86.82	0.87 ± 0.014	0.133 ± 0.04	O <sub>2</sub> blown at 66 cm <sup>3</sup> /min
89.45	0.87 ± 0	0.134 ± 0.008	O <sub>2</sub> blown at 66 cm <sup>3</sup> /min
99.72	0.79	--	O <sub>2</sub> blown at 66 cm <sup>3</sup> /min
101.48	0.835 ± 0.007	0.139 ± 0.01	O <sub>2</sub> blown at 66 cm <sup>3</sup> /min
114.82	0.79	0.144 ± 0.018	O <sub>2</sub> blown at 66 cm <sup>3</sup> /min
132.98	0.715 ± 0.007	0.139	O <sub>2</sub> blown at 66 cm <sup>3</sup> /min
144.73	0.68	0.165	O <sub>2</sub> blown at 66 cm <sup>3</sup> /min
162.48	0.62 ± 0.014	0.158 ± 0.004	O <sub>2</sub> blown at 66 cm <sup>3</sup> /min
Pooled Std. Deviation	0.087	0.020	

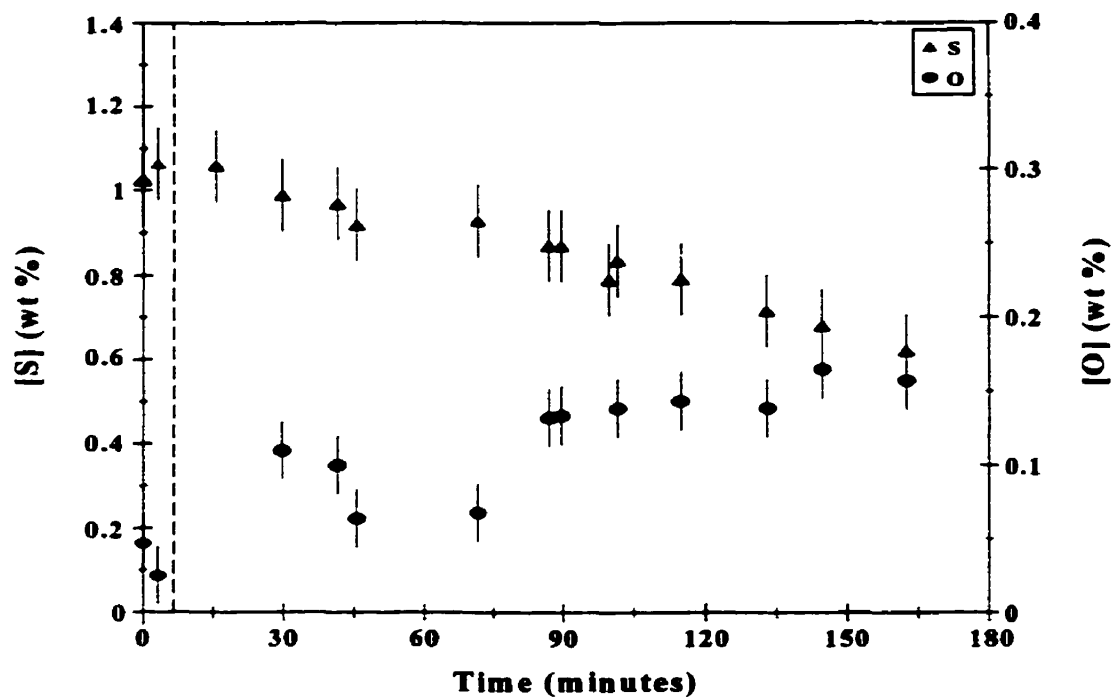


Figure 30. The dissolved S and O concentration profiles over time in Test 2. The vertical line coincides with the introduction of pure O<sub>2</sub> onto the melt surface at 66 cm<sup>3</sup>/min.

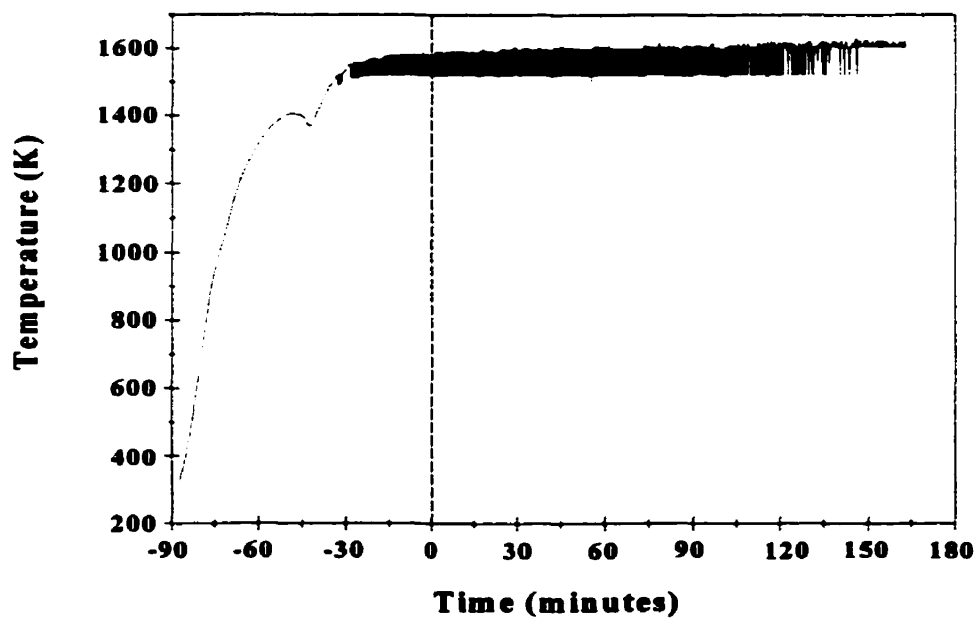
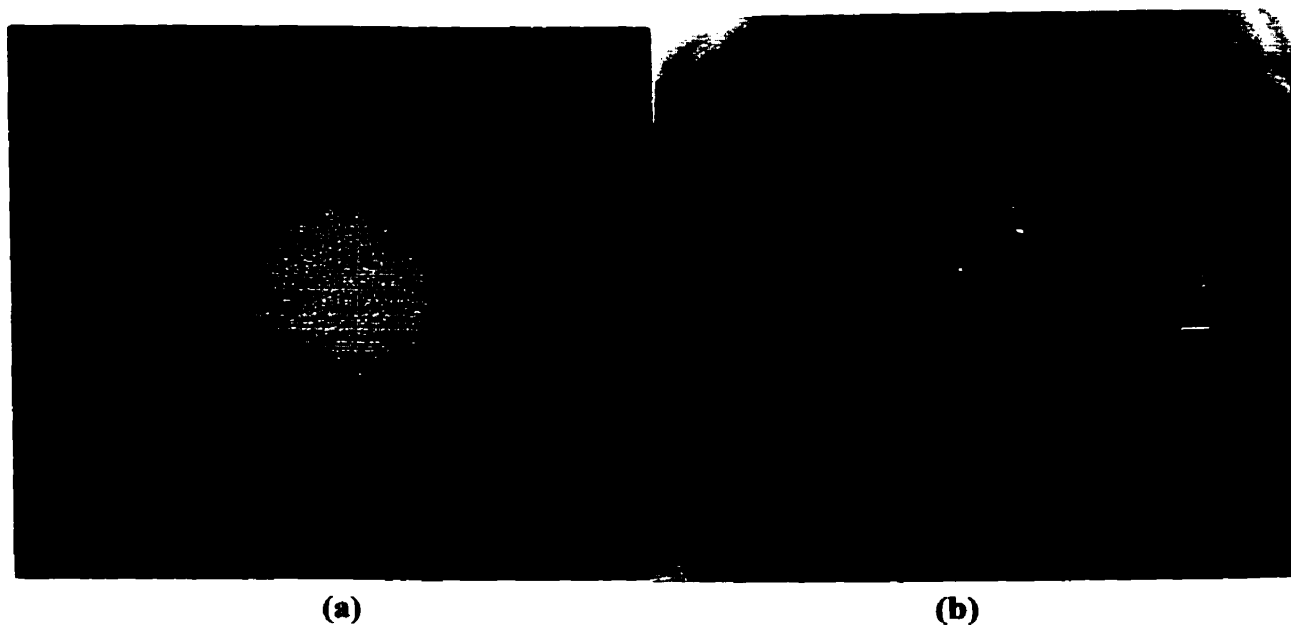


Figure 31. The time temperature profile of the melt in Test 2 relative to the sampling time  $t = 0$ ; the depression in the curve near 1400 K indicates liquefaction of the alloy charge while the horizontal line marks the bath setpoint temperature of 1523K.



**Figure 32.** Photographs of the alloy surface and oxide film from Test 2 at (a) 1523 K and  $t = 70$  minutes; a highly emissive solid or liquid oxide near the crucible wall is surrounded by the darker liquid alloy and (b) room temperature where the blistered alloy surface is partially covered by dark regions of oxidized copper.



**Figure 33.** Photograph of the quartz reaction vessel, from Test 2, along its vertical length showing solidified droplets of ejected material.

**Test 3: Desulfurization of Cu - 1 wt % S Alloy with 75 cm<sup>3</sup> O<sub>2</sub>/min**

Due to the loss of two quartz reaction vessels by contact with the melts in Test 1 and Test 2, the high density alumina crucible used to contain the copper alloy charge was placed within a graphite spill receptacle (see Figure 21 Chapter 3) while a 15 cm alumina wall extension was added to the lip of the alumina crucible to shield the quartz tube from melt ejections. As in Test 2, a 1 kg (1009 g) section of CS master alloy was melted to a setpoint temperature of 1523 K under nitrogen . The liquid alloy was sampled three times over a period of 21 minutes while still under nitrogen and then impinged with pure oxygen at 75 cm<sup>3</sup>/min for approximately 205 minutes. After 130 minutes of oxygen blowing there was no discernable change in the sulfur content of the bath however the oxygen content increased to about 0.8 - 0.9 wt % (see Table 9 and Figure 34). An additional 75 minutes of oxygen blowing reduced the sulfur content to 0.84 wt % while the dissolved oxygen level increased to 0.12 wt %.

**Table 9. Tabulated S and O assays from Test 3 conducted at 1523 K by blowing pure O<sub>2</sub> at 75 cm<sup>3</sup>/min on the surface of a CS alloy charge.**

<b>Sampling Time minutes</b>	<b>[S] Wt %</b>	<b>[O] Wt %</b>	<b>Experimental Condition</b>
0.00	0.953	0.005	Melt Homogenization
5.17	0.963	0.024	Melt Homogenization
21.17	0.939	--	Melt Homogenization
22.58	--	--	O <sub>2</sub> introduced at 75 cm <sup>3</sup> /min
32.00	0.956	0.006	O <sub>2</sub> blown at 75 cm <sup>3</sup> /min
46.15	1.01	0.028	O <sub>2</sub> blown at 75 cm <sup>3</sup> /min
52.92	1.06	--	O <sub>2</sub> blown at 75 cm <sup>3</sup> /min
66.12	1	0.012	O <sub>2</sub> blown at 75 cm <sup>3</sup> /min
68.00	1.04	0.022	O <sub>2</sub> blown at 75 cm <sup>3</sup> /min
77.50	1.06	0.019	O <sub>2</sub> blown at 75 cm <sup>3</sup> /min
88.33	0.993	0.022	O <sub>2</sub> blown at 75 cm <sup>3</sup> /min
91.10	1.04	--	O <sub>2</sub> blown at 75 cm <sup>3</sup> /min
103.78	1.05	0.039	O <sub>2</sub> blown at 75 cm <sup>3</sup> /min
115.83	1.05	0.093	O <sub>2</sub> blown at 75 cm <sup>3</sup> /min
126.33	1.06	--	O <sub>2</sub> blown at 75 cm <sup>3</sup> /min
147.17	1.08	--	O <sub>2</sub> blown at 75 cm <sup>3</sup> /min
159.33	1.06	0.082	O <sub>2</sub> blown at 75 cm <sup>3</sup> /min

Table 9. Continued

Sampling Time minutes	[S] wt %	[O] wt %	Experimental Conditions
169.33	1	--	O <sub>2</sub> blown at 75 cm <sup>3</sup> /min
182.08	0.985	--	O <sub>2</sub> blown at 75 cm <sup>3</sup> /min
197.67	0.97	--	O <sub>2</sub> blown at 75 cm <sup>3</sup> /min
206.70	0.819	--	O <sub>2</sub> blown at 75 cm <sup>3</sup> /min
209.75	0.889	--	O <sub>2</sub> blown at 75 cm <sup>3</sup> /min
220.42	0.945	0.119	O <sub>2</sub> blown at 75 cm <sup>3</sup> /min
228.00	0.841	--	O <sub>2</sub> blown at 75 cm <sup>3</sup> /min

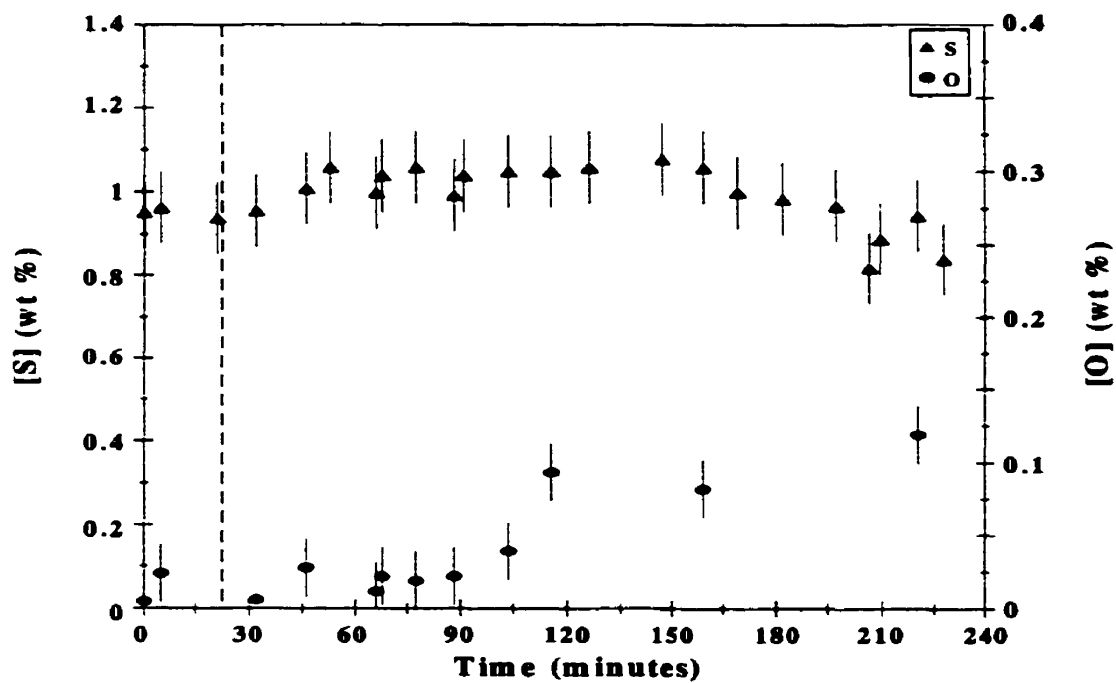
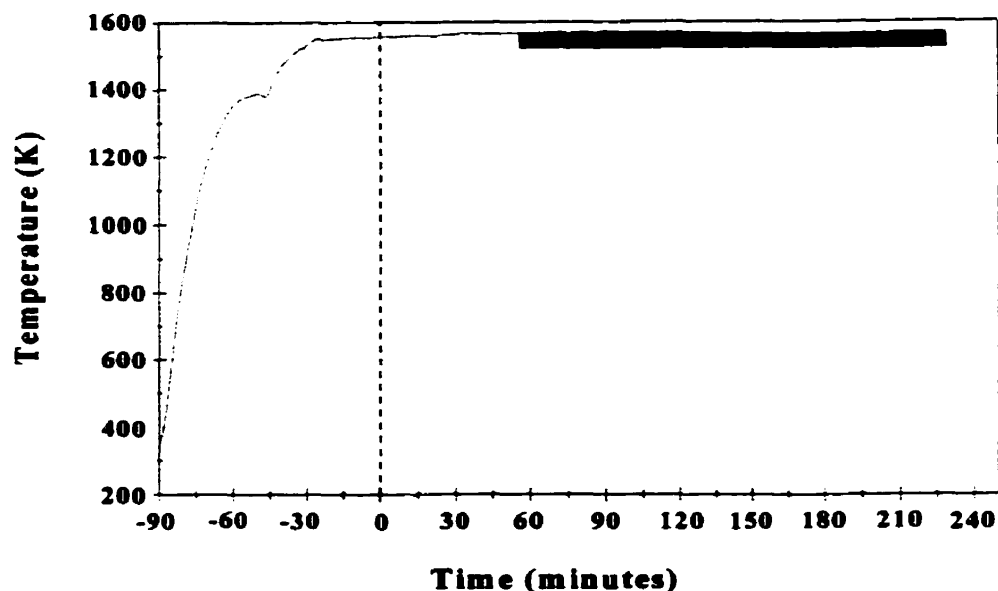


Figure 34. The dissolved S and O concentration profile over time for Test 3 at 1523 K. The vertical line coincides with the introduction of pure O<sub>2</sub> onto the melt surface at 75 cm<sup>3</sup>/min.

Although observation of the bath did not reveal any high speed motion of oxide away from the region below the lance tip, within 15 minutes of oxygen injection, the melt surface was covered by an emissive, oxide layer. Neither the melt nor the oxide penetrated the crucible.

As in previous tests the bath temperature indicated by the data acquirer usually exceeded the setpoint temperature of 1523 K displayed by the bath temperature controller (see Figure 35).



**Figure 35.** The time temperature profile of the melt in Test 3 relative to the sampling time  $t = 0$ ; the depression in the curve near 1400 K indicates liquefaction of the alloy charge while the horizontal line marks the bath setpoint temperature of 1523K.

#### ***Test 4: Desulfurization of Cu - 3 wt % Ni - 1 wt % S Alloy with 75 cm<sup>3</sup> O<sub>2</sub>/min***

In Test 4, a 1.1 kg (1093 g) charge of CNS master alloy was melted under nitrogen in the crucible configuration used in Test 3. Upon reaching 1523 K the melt was top-blown with oxygen at 75 cm<sup>3</sup>/min over a period of 210 minutes and at 372 cm<sup>3</sup>/min for 33 minutes. The elemental assays for this test are presented in Table 10 and Figure 36. The concentration profile of the copper alloy over time remained almost constant with respect to sulfur while the scatter in the oxygen measurements precludes any assessment in the change of the oxygen concentration below the level 0.01 wt %. Nickel determinations appear constant at 3 wt % - 3.5 wt % for most of the duration of oxygen blowing at 75 cm<sup>3</sup>/min; the values decrease near the end of this period and again after the oxygen flowrate was increased to 372 cm<sup>3</sup>/min. Dissolved oxygen levels also dropped with increased oxygen delivery to the melt while sulfur levels remained constant.

No evidence of Marangoni convection appeared in the visual record of the experiment and as in Test 3 the liquid surface had become almost completely covered by an emissive oxide layer within 15 minutes of oxygen injection (see Figure 37). As in previous

tests, the temperature from the data acquirer consistently exceeded the setpoint value of 1523 K displayed by the bath controller (see Figure 38).

**Table 10. Tabulated S, O and Ni assays from Test 4 conducted at 1523 K with CNS alloy initially blown with pure O<sub>2</sub> jet at 75 cm<sup>3</sup>/min and then at 372 cm<sup>3</sup>/min.**

Sampling Time minutes	[S] Wt %	[O] Wt %	[Ni] Wt %	Experimental Stage
0.00	1.13	0.004 ± 0.004		Melt Homogenization
26.17	1.16		3.18	Melt Homogenization
28.33				O <sub>2</sub> introduced at 75 cc/min
37.67	1.1	--	--	O <sub>2</sub> blown at 75 cm <sup>3</sup> /min
49.67	1.13	0.052	3.48	O <sub>2</sub> blown at 75 cm <sup>3</sup> /min
60.17	1.09	--	--	O <sub>2</sub> blown at 75 cm <sup>3</sup> /min
66.50	1.11	--	--	O <sub>2</sub> blown at 75 cm <sup>3</sup> /min
70.17	1.12	0.003	3	O <sub>2</sub> blown at 75 cm <sup>3</sup> /min
86.33	1.14	--	--	O <sub>2</sub> blown at 75 cm <sup>3</sup> /min
101.00	1.12	<0.001*	3.36	O <sub>2</sub> blown at 75 cm <sup>3</sup> /min
115.67	1.04	--	--	O <sub>2</sub> blown at 75 cm <sup>3</sup> /min
121.67	1.17	0.006	--	O <sub>2</sub> blown at 75 cm <sup>3</sup> /min
131.00	1.15	0.01	3.06	O <sub>2</sub> blown at 75 cm <sup>3</sup> /min
141.17	1.13	<0.001	--	O <sub>2</sub> blown at 75 cm <sup>3</sup> /min
152.67	1.16	0.003	--	O <sub>2</sub> blown at 75 cm <sup>3</sup> /min
161.83	1.13	0.01	3.22	O <sub>2</sub> blown at 75 cm <sup>3</sup> /min
174.33	1.16	0.006	--	O <sub>2</sub> blown at 75 cm <sup>3</sup> /min
185.17	1.15	0.008	3.39	O <sub>2</sub> blown at 75 cm <sup>3</sup> /min
195.17	1.16	0.002	--	O <sub>2</sub> blown at 75 cm <sup>3</sup> /min
205.17	1.19	0.003	1.51	O <sub>2</sub> blown at 75 cm <sup>3</sup> /min
215.33	1.1	0.004	--	O <sub>2</sub> blown at 75 cm <sup>3</sup> /min
221.83	1.14	--	--	O <sub>2</sub> blown at 75 cm <sup>3</sup> /min
232.42	1.13	<0.001	2.64	O <sub>2</sub> blown at 75 cm <sup>3</sup> /min
236.62	1.13	0.009	--	O <sub>2</sub> blown at 75 cm <sup>3</sup> /min
238.80	--	--	--	O <sub>2</sub> introduced at 372 cm <sup>3</sup> /min
246.00	1.13	0.006	2.59	O <sub>2</sub> blown at 372 cm <sup>3</sup> /min
255.17	1.11	--	--	O <sub>2</sub> blown at 372 cm <sup>3</sup> /min
261.57	1.12	<0.001	2.61	O <sub>2</sub> blown at 372 cm <sup>3</sup> /min
267.50	1.15	<0.001	--	O <sub>2</sub> blown at 372 cm <sup>3</sup> /min
272.17	1.15	<0.001	3.39	O <sub>2</sub> blown at 372 cm <sup>3</sup> /min

\*Oxygen determinations <0.001 wt % were plotted as zero on subsequent plots of the melt concentration profile versus time.

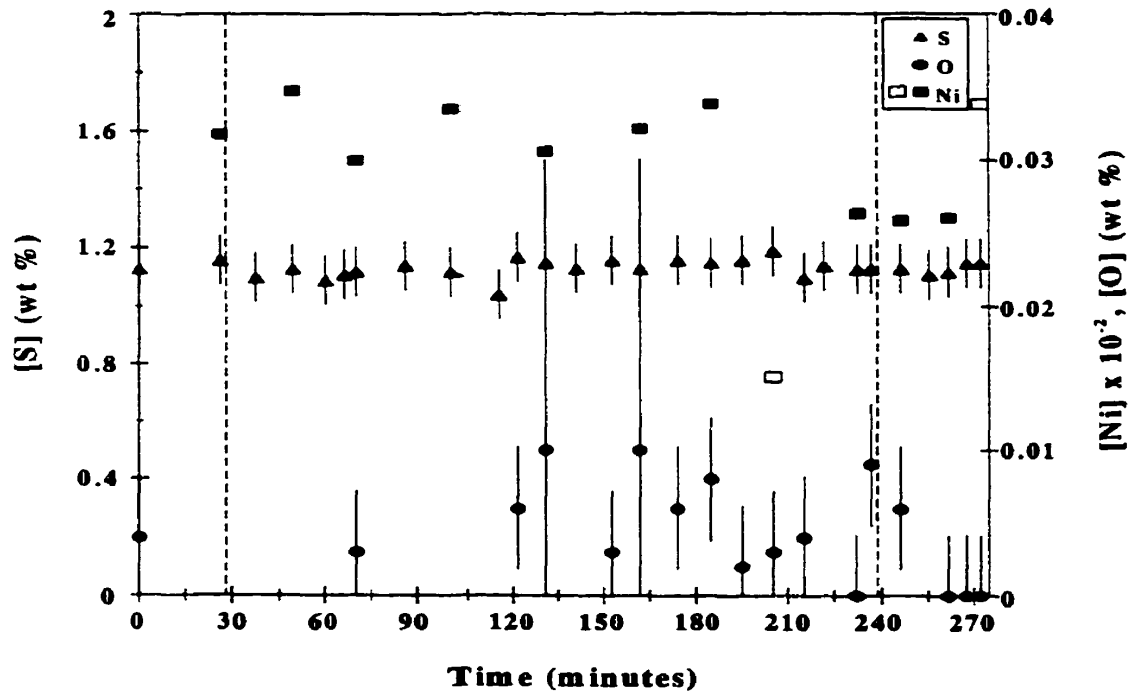


Figure 36. The dissolved S, O and Ni concentration profile over time in Test 4. The first and second vertical lines coincide respectively with the introduction of pure O<sub>2</sub> onto the melt surface at 75 cm<sup>3</sup>/min and then at 372 cm<sup>3</sup>/min.

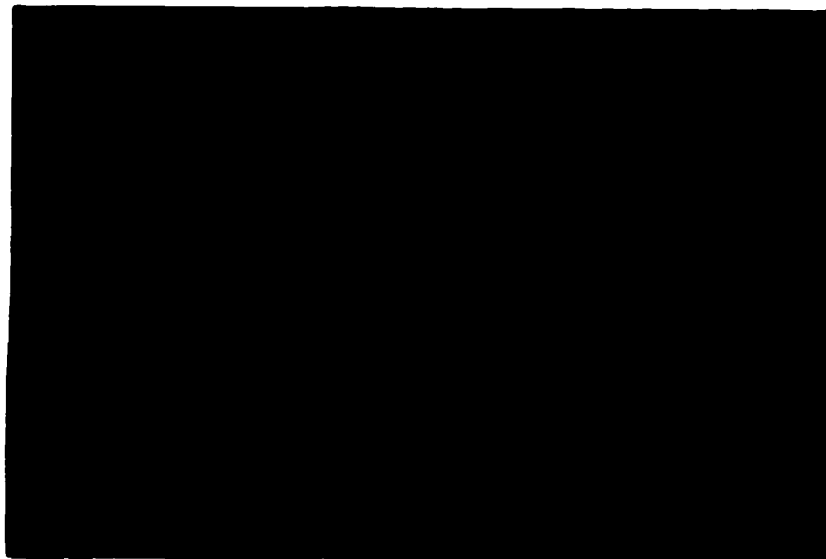


Figure 37. Photograph of the melt surface in Test 4 covered by an emissive oxide film at 1523 K and t = 40 minutes. The dark region is the liquid metal surface that was exposed after a sample had been extracted from the melt.

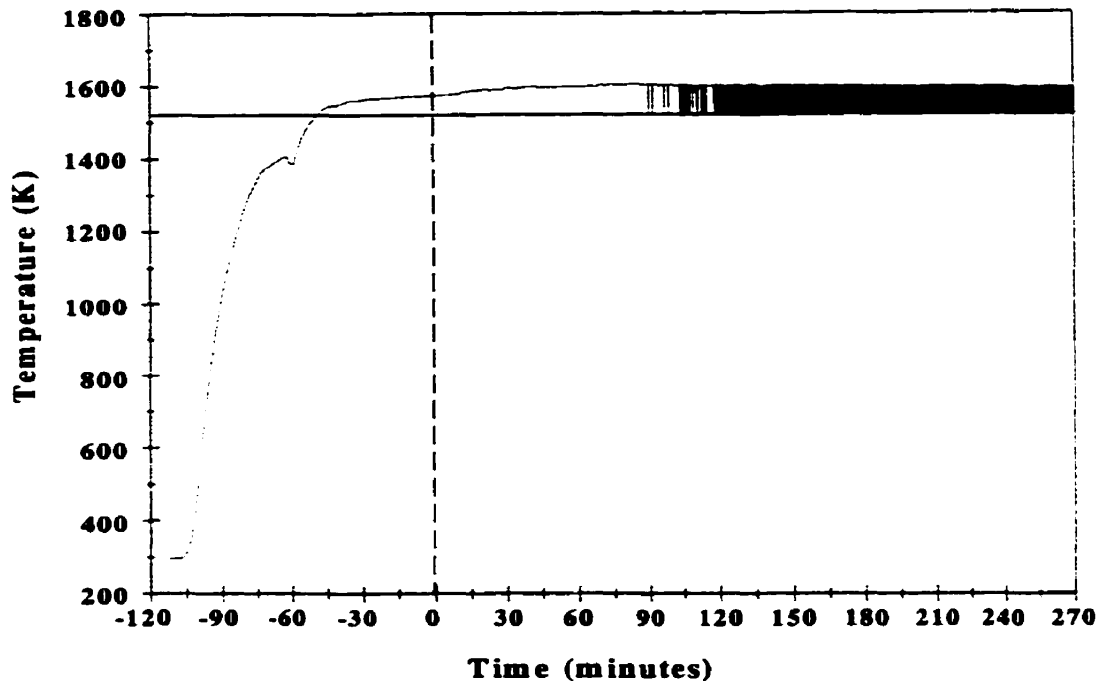


Figure 38. The time temperature profile of the melt in Test 4 relative to the sampling time  $t = 0$ ; the depression in the curve near 1400 K indicates liquefaction of the alloy charge while the horizontal line marks the bath setpoint temperature of 1523K.

#### *Test 5, Test 6: Oxidation of Cathode Copper with 75 and 372 cm<sup>3</sup> O<sub>2</sub>/min*

In Test 5 and Test 6 cathode copper was melted under nitrogen in the same crucible configuration used in Test 3 and Test 4 and subsequently impinged with pure oxygen at a flowrate of 75 cm<sup>3</sup>/min for 191 minutes and at 372 cm<sup>3</sup>/min for 20 minutes at 1523 K. The objectives were to compare the level of oxygen dissolution in cathode copper versus measurements made for the CS and CNS alloys and observe whether Marangoni convection would occur more readily under the influence of only one surface active agent i.e. oxygen. The crucible in Test 5 failed at the start of the experiment which resulted in contact of the melt with the graphite spill receptacle and hence deoxidation of the copper. This was evident by a dark and highly reflective melt surface observed for the duration of the experiment (see Figure 40b). As a result of this event the samples from Test 5 were not analyzed and the experiment was repeated as Test 6 with a copper charge weighing 1 kg (1068 g).

The oxygen concentration profile of the copper melt over time in Test 6 is tabulated in Table 11 and graphically depicted in Figure 39. During oxygen blowing at 75 cm<sup>3</sup>/min, the oxygen determinations were widely scattered between 0.001 wt % and 0.01 wt %; at the higher oxygen flowrate of 372 cm<sup>3</sup>/min the dissolved oxygen level increased to between 0.285 wt % and 0.373 wt % after 20 minutes of blowing.

**Table 11. Tabulated O assays from Test 6 conducted at 1523 K by blowing a pure O<sub>2</sub> jet at 75 cm<sup>3</sup>/min on the surface of a cathode copper.**

Sampling Time minutes	[O] Wt %	Experimental Condition
0.00	0.009	Melt Homogenization
7.12	0.031	Melt Homogenization
8.78		O <sub>2</sub> introduced at 75 cc/min
17.95	0.006	O <sub>2</sub> blown at 75 cm <sup>3</sup> /min
28.22	0.005	O <sub>2</sub> blown at 75 cm <sup>3</sup> /min
37.48	0.093	O <sub>2</sub> blown at 75 cm <sup>3</sup> /min
49.12	0.0008	O <sub>2</sub> blown at 75 cm <sup>3</sup> /min
57.95	0.0015	O <sub>2</sub> blown at 75 cm <sup>3</sup> /min
67.85	0.0036	O <sub>2</sub> blown at 75 cm <sup>3</sup> /min
78.03	0.018	O <sub>2</sub> blown at 75 cm <sup>3</sup> /min
87.63	0.0018	O <sub>2</sub> blown at 75 cm <sup>3</sup> /min
97.95	0.0088	O <sub>2</sub> blown at 75 cm <sup>3</sup> /min
107.78	0.0019	O <sub>2</sub> blown at 75 cm <sup>3</sup> /min
117.53	0.0036	O <sub>2</sub> blown at 75 cm <sup>3</sup> /min
128.20	0.003	O <sub>2</sub> blown at 75 cm <sup>3</sup> /min
137.53	0.0032	O <sub>2</sub> blown at 75 cm <sup>3</sup> /min
147.95	0.0026	O <sub>2</sub> blown at 75 cm <sup>3</sup> /min
157.57	0.0033	O <sub>2</sub> blown at 75 cm <sup>3</sup> /min
167.37	0.0089	O <sub>2</sub> blown at 75 cm <sup>3</sup> /min
177.37	0.0039	O <sub>2</sub> blown at 75 cm <sup>3</sup> /min
187.37	0.028	O <sub>2</sub> blown at 75 cm <sup>3</sup> /min
197.37	0.002	O <sub>2</sub> blown at 75 cm <sup>3</sup> /min
199.95		O <sub>2</sub> introduced at 372 cm <sup>3</sup> /min
207.45	0.373	O <sub>2</sub> blown at 372 cm <sup>3</sup> /min
213.38	0.289	O <sub>2</sub> blown at 372 cm <sup>3</sup> /min
220.62	0.309	O <sub>2</sub> blown at 372 cm <sup>3</sup> /min
227.28	0.392	O <sub>2</sub> blown at 372 cm <sup>3</sup> /min
234.35	0.285	O <sub>2</sub> blown at 372 cm <sup>3</sup> /min
239.42	0.316	O <sub>2</sub> blown at 372 cm <sup>3</sup> /min

In contrast to Test 5, the surface of Test 6 became covered by an emissive, oxide layer within 10 minutes of oxygen injection (see Figure 40a). Marangoni convection was not observed in either of these experiments and as in previous tests the melt temperature values from the data acquirer and the bath controller display often differed (see Figure 41).

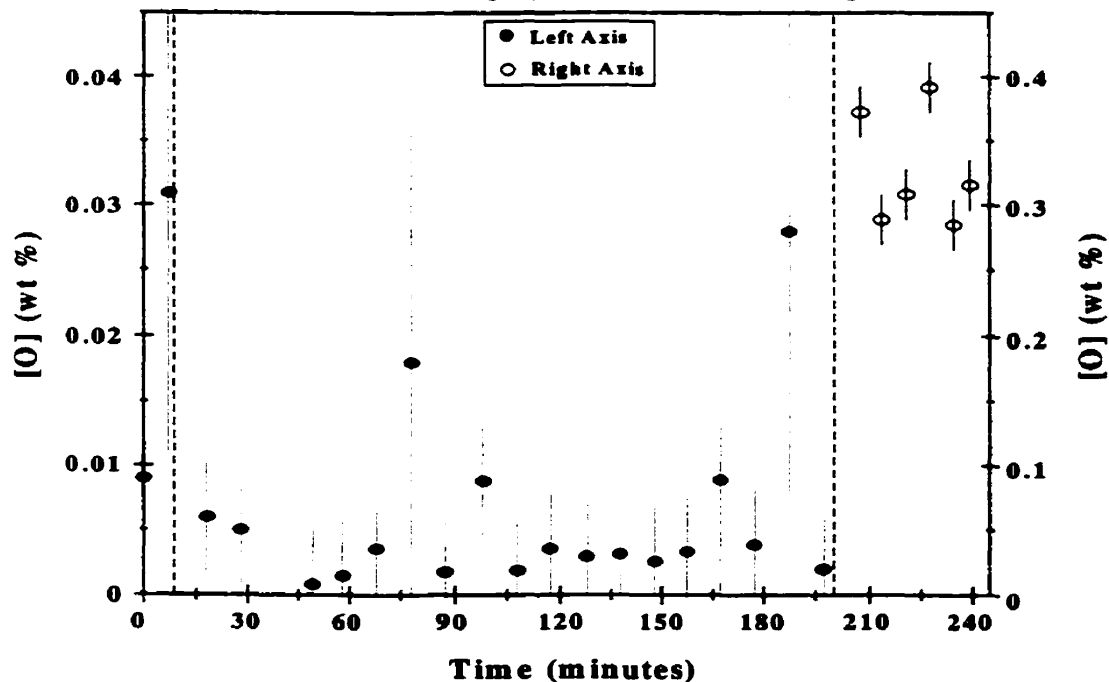


Figure 39. The dissolved O concentration profile over time in Test 6. The first and second vertical lines coincide respectively with the introduction of pure  $O_2$  onto the melt surface at  $75 \text{ cm}^3/\text{min}$  and then at  $372 \text{ cm}^3/\text{min}$ .

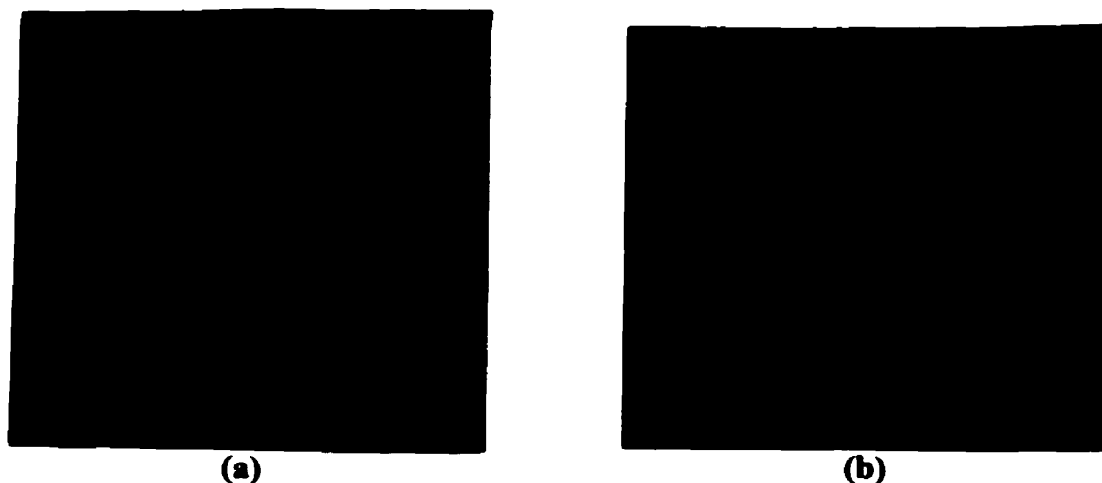


Figure 40. Photographs of the melt surface at 1523 K in (a) Test 6 covered by an emissive oxide layer after 22 minutes of  $O_2$  blowing (i.e.  $t_{\text{blowing}} = 32$  minutes) and (b) Test 5 after 35 minutes of  $O_2$  blowing at  $75 \text{ cm}^3/\text{min}$ ; note the mirror image of the gas lance on the dark but reflective melt surface.

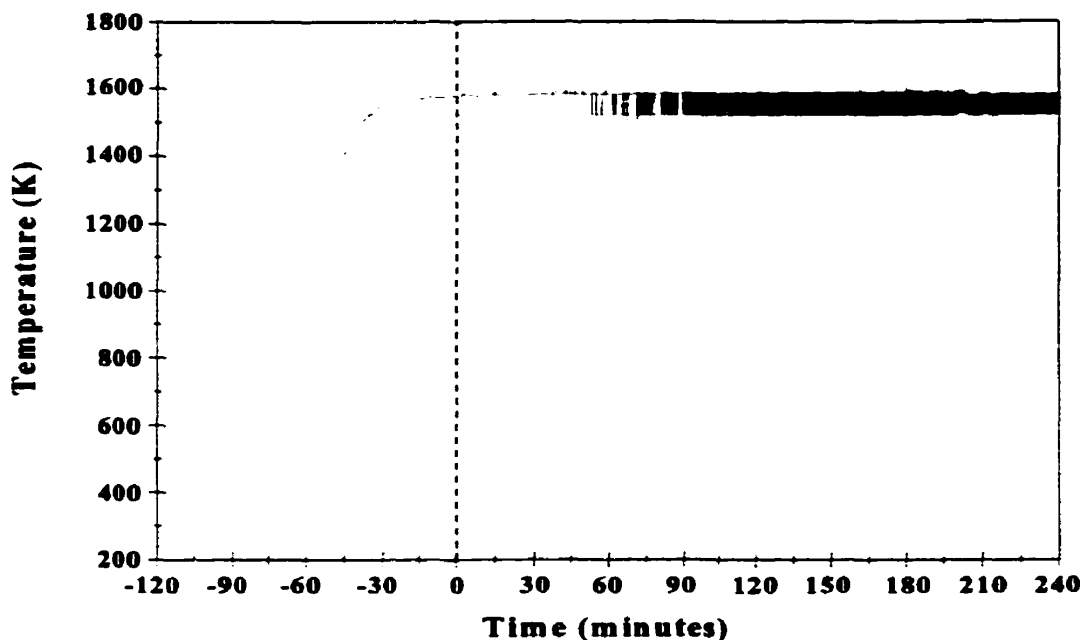


Figure 41. The time temperature profile of the melt in Test 6 relative to the sampling time  $t = 0$ ; the depression in the curve near 1400 K indicates liquefaction of the alloy charge while the horizontal line marks the bath setpoint temperature of 1523K.

### ***Test 7, Test 8: Desulfurization of Cu-1 wt % S Alloy Exposed to Air***

In Test 7 and Test 8, CS master alloy charges, weighing respectively 0.83 kg (831g) and 0.89 kg (891g), were melted in HYCOR alumina crucibles under air with the objectives of measuring sulfur elimination of stagnant melts exposed to the open atmosphere and verifying the reproducibility of experimental results. In both tests the crucibles were placed within a larger HYCOR alumina spill receptacle which was partially filled with silica sand.

The melt surface in both tests became partially covered with an oxide layer from the onset of sampling which was initiated just prior to the melt reaching 1523 K (see Figure 42). In both tests, the melt spontaneously effervesced (see Figure 43), i.e., erupted with bubbles and vigorously agitated the bath for 10-20 minutes, which destroyed the oxidized surface layer and accelerated sulfur elimination. A period of melt quiescence followed this effervescent episode after which the melt erupted for a second time. These eruptions sprayed material from the melt onto the interior furnace chamber and onto the fiberfrax insulation cover located 44 cm above the melt surface. The composition profiles over time of Test 7

and Test 8 are tabulated in Table 12 and presented in Figure 44 which also marks the onset of effervescence in both tests. The sampling time in Test 8 was adjusted to coincide with time scale of Test 7 when the melt assays are almost identical at about 0.16 wt % S. Oxygen impinged on the melt surfaces of both tests at 75 cm<sup>3</sup>/min did not appear to affect oxygen dissolution or sulfur elimination from the melts (see Figure 55, Chapter 5) and both tests showed thermal deviations from the setpoint temperatures which were unrelated to the surface eruptions. The source of these deviations remained undetermined.

Similar reports of effervescence were made by Rioux<sup>104</sup> in desulfurization tests of CS alloy charges top blown with oxygen at 75 cm<sup>3</sup>/min, 500 cm<sup>3</sup>/min and 1000 cm<sup>3</sup>/min. The charges were melted in the experimental apparatus used in this study and under the same crucible configuration and conditions used in Test 7 and Test 8 of this study. Rioux also did not observe any instances of Marangoni convection in any of the tests.

**Table 12. S and O determinations for Test 7 and Test 8. The time scale in Test 8 has been adjusted to coincide with the sampling time of Test 7 at t = 61 minutes where the S content of both melts is similar.**

Time minutes	Test 7 [S] wt %	Test 7 [O] wt %	Test 7 Temp. K	Test 8 [S] wt %	Test 8 [O] wt %	Test 8 Temp. K
0.00		0.061	1400			
10.00	0.445		1459			
20.00		0.089	1493			
30.00	0.425		1517			
31.67		0.136	1521			
37.57				0.333		1414
41.13	0.274		1529			
45.50				0.314	0.165	1454
50.05		0.234	1517			
55.50				0.233	0.209	1488
<b>61.00</b>	0.164		1528	0.161	0.276	1500
62.67				0.161	0.197	1503
68.34				0.183	0.192	1514
70.42		0.393	1524			
75.50				0.056		1528
82.05	0.045		1522			
83.17				0.062	0.473	1528
93.50				0.056		1511

Table 12. *Continued*

Time minutes	Test 7 [S] wt %	Test 7 [O] wt %	Test 7 Temp. K	Test 8 [S] wt %	Test 8 [O] wt %	Test 8 Temp. K
93.53		0.25	1524			
104.00					0.57	1531
109.10	0.062		1527			
116.00				0.019		1513
123.55		0.235	1512			
125.84				0.02		1523
126.95				0.056	0.598	1525
137.88	0.044		1534			
139.02		0.246	--			
140.95				0.021		1510
148.67					1.5	1514
158.15				0.019		1536
162.05		0.615	1529			
168.00				0.013	1.49	1507
174.50				0.013	1.42	--

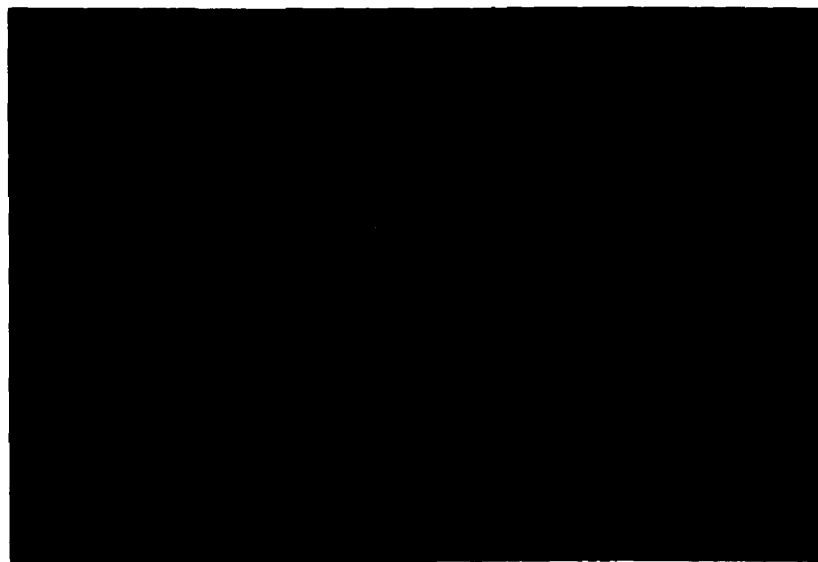


Figure 42. Photograph of the melt surface in Test 8 covered by an emissive oxide at approximately  $t = 0$  minutes. The darker spots are the exposed surface of the liquid alloy.

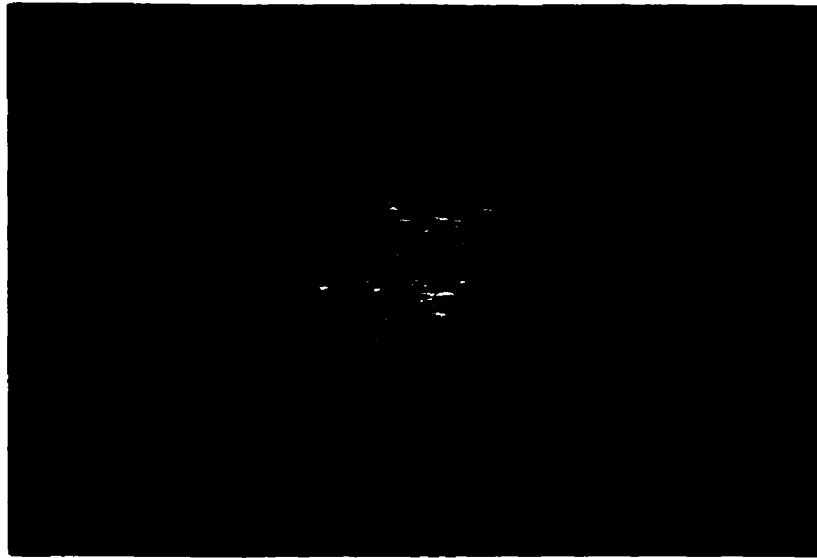


Figure 43. Photograph of the melt surface effervescing in Test 8 at  $t = 28$  minutes.

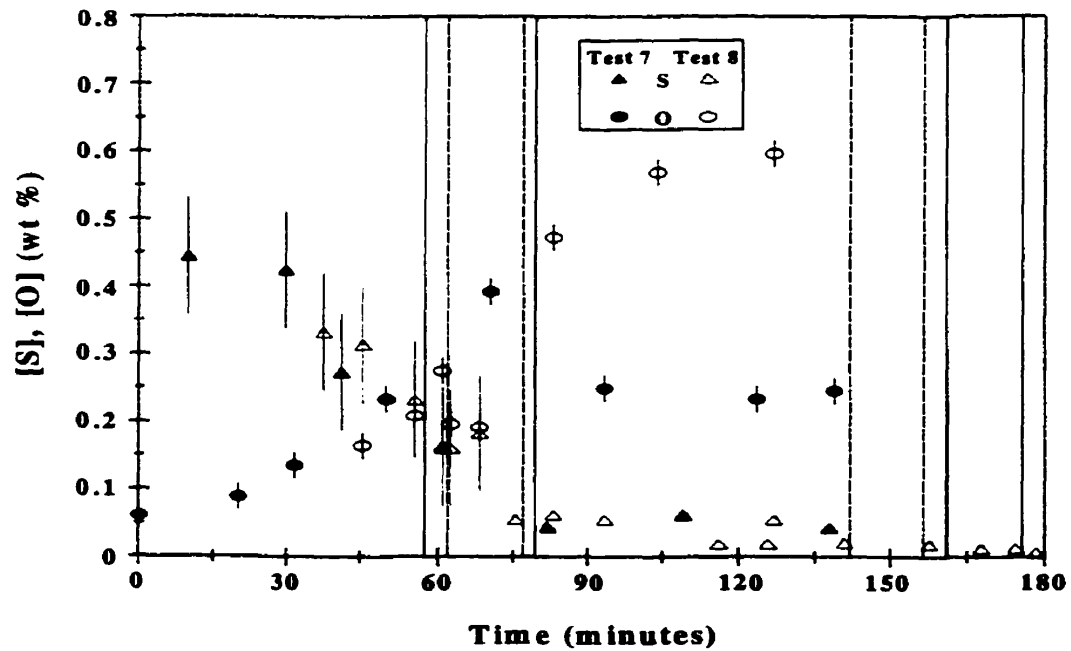


Figure 44. The dissolved S and O concentration profiles over time for Test 7 and Test 8. The dashed and solid vertical lines respectively mark the occurrence and duration of effervescence in Test 7 and Test 8.

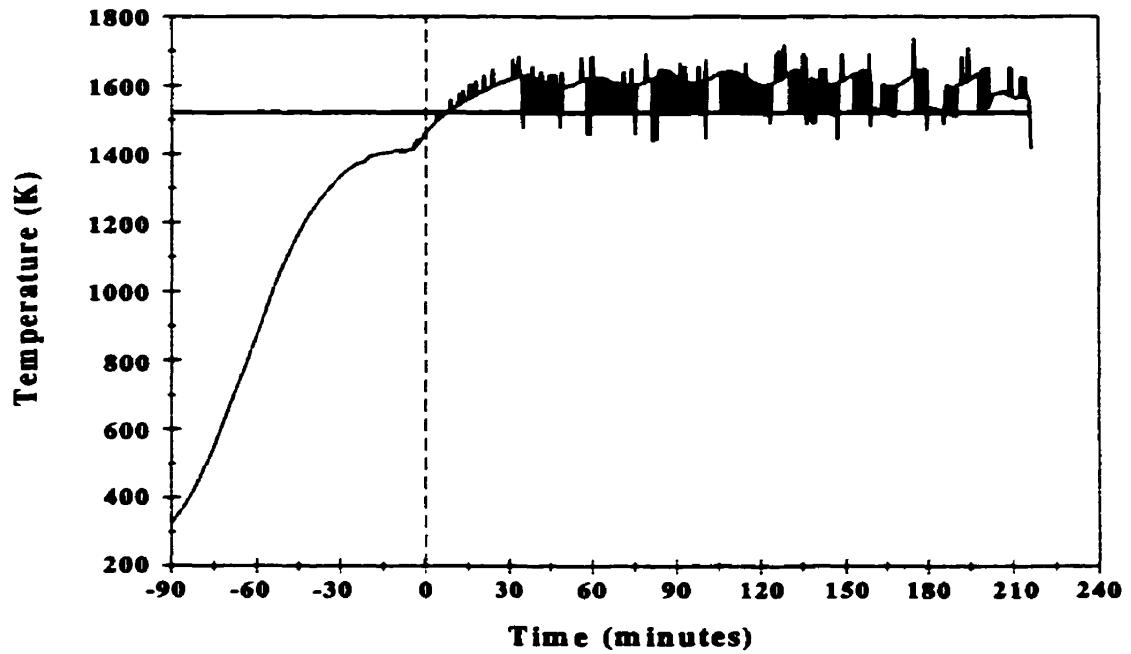


Figure 45. The time temperature profile of the melt in Test 7 relative to the sampling time  $t = 0$ ; the plateau in the curve near 1400 K indicates liquefaction of the alloy charge while the horizontal line marks the bath setpoint temperature of 1523K.

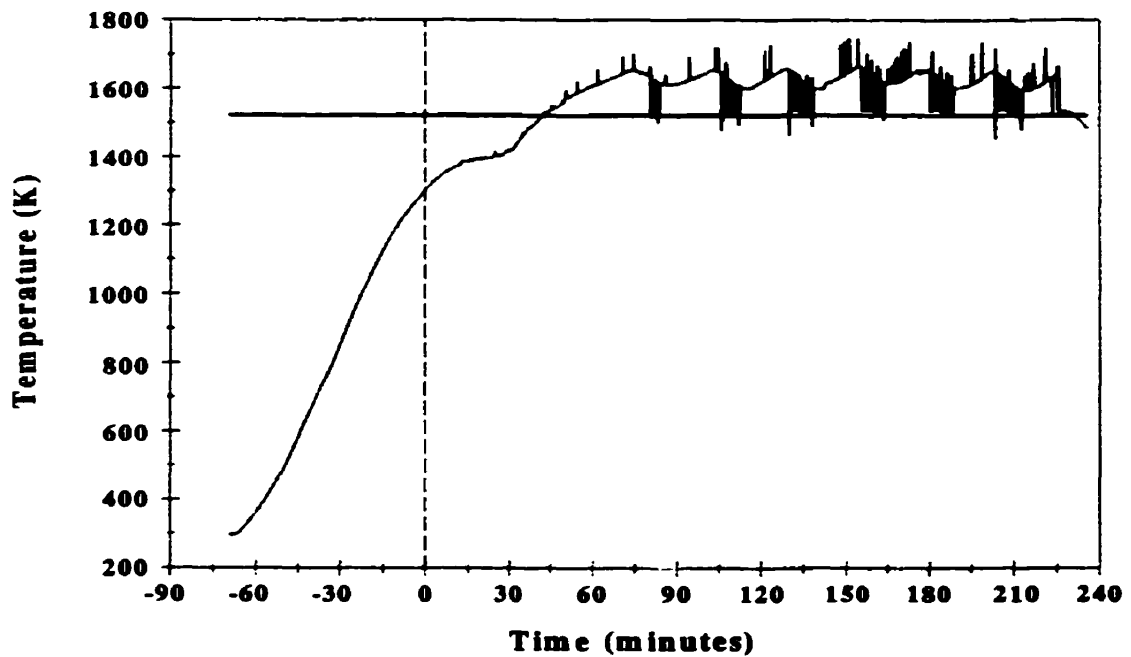


Figure 46. The time temperature profile of the melt in Test 8 relative to the sampling time  $t = 0$ ; the plateau in the curve near 1400 K indicates liquefaction of the alloy charge while the horizontal line marks the bath setpoint temperature of 1523K.

**Test 9: Desulfurization of Cu - 3 wt % Ni - 1 wt % S Alloy Exposed to Air**

The same conditions and crucible configuration which were used in both Test 7 and Test 8 were applied in Test 9 to measure sulfur elimination from a 1 kg (1035.0 g) melt of CNS master alloy. The concentration profile of the melt (see Table 13 and see Figure 47) shows a gradual decrease of sulfur over time and no greater degree of oxygen dissolution over the copper-sulfur melts in Test 7 and Test 8; nickel assays do not show any obvious trend and are above the mean alloy concentration. No spontaneous eruptions were observed and the melt surface always remained covered by an oxide layer (see Figure 48). Submerged nitrogen stirring of the bath did not affect the nickel and oxygen levels in the bath, but the increased melt agitation did result in greater sulfur removal. The time temperature profile of the bath, shown in Figure 49, displayed deviations from the setpoint temperature of 1523 K at periodic intervals.

**Table 13. Tabulated S, O and Ni assays from Test 9 for CNS alloy melted under air and then blown with pure O<sub>2</sub> at 75 cm<sup>3</sup>/min and finally subjected to submerged N<sub>2</sub> injection at 2000 cm<sup>3</sup>/min.**

<b>Sampling Time minutes</b>	<b>[S] wt %</b>	<b>[O] wt %</b>	<b>[Ni] wt %</b>	<b>Temp K</b>	<b>Experimental Condition</b>
0.00	0.673	0.119	3.01	1418	Melt exposed to air
10.57	0.465	0.146		1472	Melt exposed to air
20.82	0.046	0.191	4.39	1502	Melt exposed to air
30.07	0.329	0.21		1522	Melt exposed to air
36.88	0.374	0.215		1530	Melt exposed to air
43.90	0.358	0.22		1520	Melt exposed to air
45.20	0.309	0.228	5.03	1518	Melt exposed to air
49.88	0.292	0.195		1515	Melt exposed to air
59.95	0.211	0.192		1531	Melt exposed to air
61.23	0.282	0.187	4.84	1531	Melt exposed to air
69.82	0.25	0.232		1517	Melt exposed to air
72.73	0.23	0.266		1513	Melt exposed to air
79.90	0.223	0.265		1523	Melt exposed to air
89.73	0.064	0.316		1530	Melt exposed to air
91.73	0.181	0.276	4.17	1523	Melt exposed to air
92.73					O <sub>2</sub> introduced at 75 cm <sup>3</sup> /min

Table 13. Continued

Sampling Time minutes	[S] wt %	[O] wt %	[Ni] wt %	Temp K	Experimental Condition
110.72	0.173	0.373	4.78	1536	O <sub>2</sub> blown at 75 cm <sup>3</sup> /min
120.02		0.415		1514	O <sub>2</sub> blown at 75 cm <sup>3</sup> /min
121.68	0.193	0.38		1509	O <sub>2</sub> blown at 75 cm <sup>3</sup> /min
130.73	0.161	0.426	2.46	1520	O <sub>2</sub> blown at 75 cm <sup>3</sup> /min
143.73					N <sub>2</sub> injection at 2000 cm <sup>3</sup> /min
147.15	0.02	0.366	3.85	1508	N <sub>2</sub> injection at 2000 cm <sup>3</sup> /min
152.05	0.143	0.502		1507	N <sub>2</sub> injection at 2000 cm <sup>3</sup> /min
153.52	0.002	0.467		1510	N <sub>2</sub> injection at 2000 cm <sup>3</sup> /min
160.20	0.001	0.469	3.21	1531	N <sub>2</sub> injection at 2000 cm <sup>3</sup> /min
169.85	0.003	0.542		1521	N <sub>2</sub> injection at 2000 cm <sup>3</sup> /min
182.07	<0.001	0.525	3.63	1524	N <sub>2</sub> injection at 2000 cm <sup>3</sup> /min

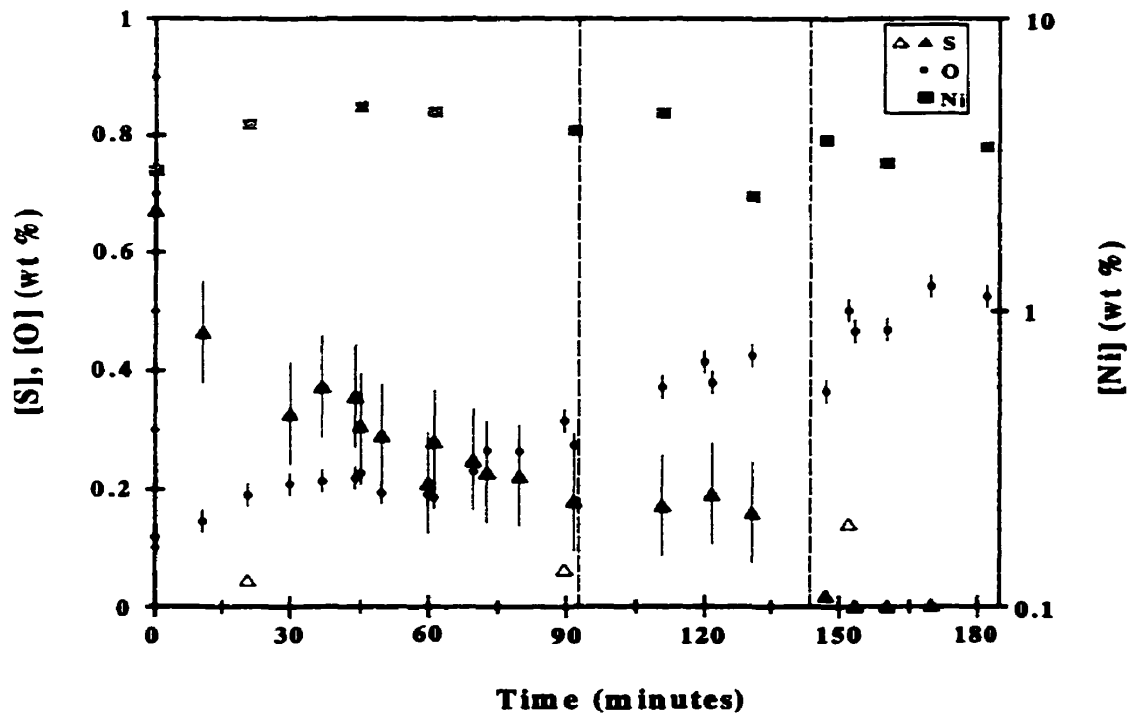


Figure 47. The S, O and Ni concentration profile over time in Test 9. The vertical lines coincide respectively with the introduction of pure oxygen onto the melt surface at 75 cm<sup>3</sup>/min and submerged nitrogen injection at 2000 cm<sup>3</sup>/min.

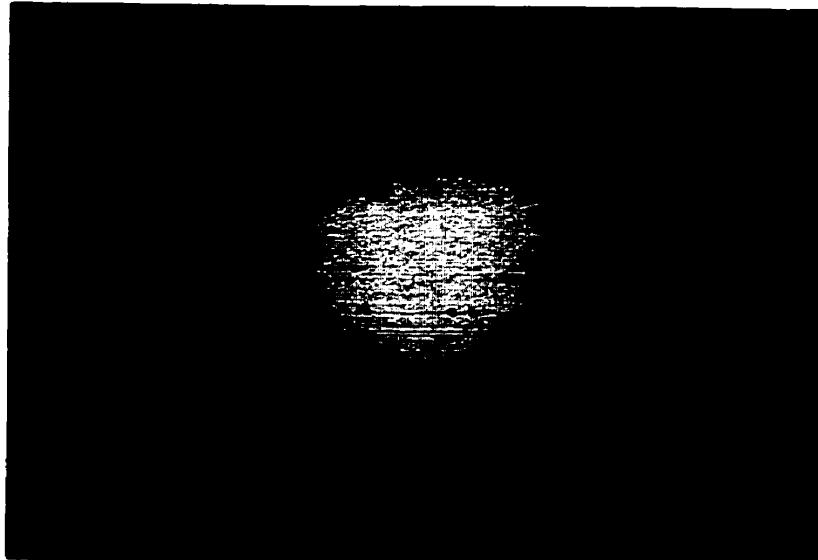


Figure 48. Photograph of the melt surface in Test 9 covered by an oxide layer at  $t = 32$  minutes.

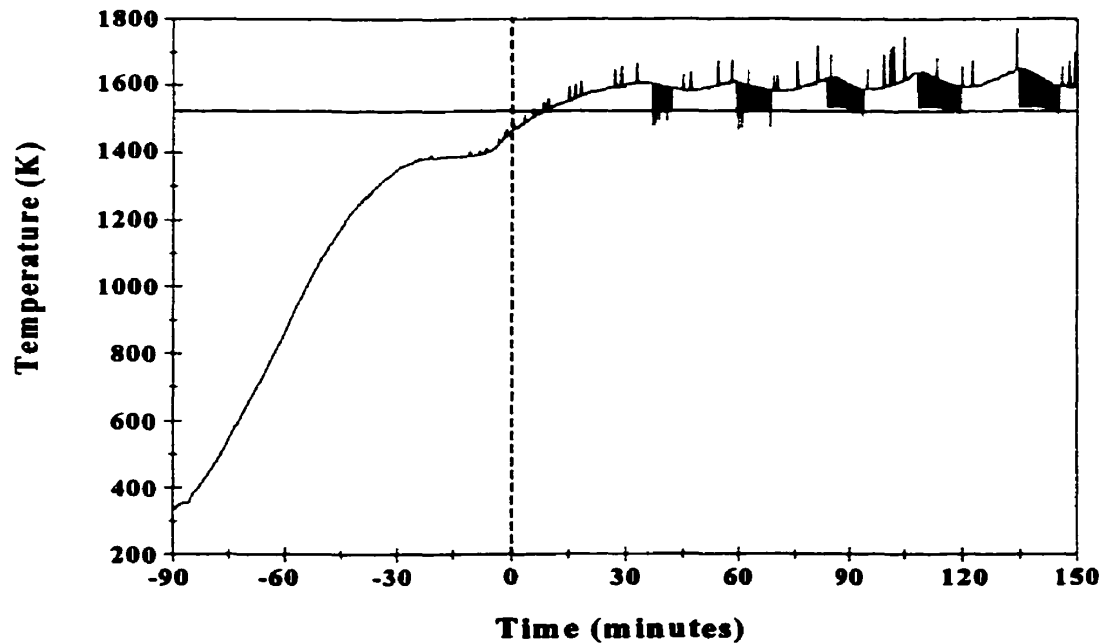


Figure 49. The time temperature profile of the melt in Test 9 relative to the sampling time  $t = 0$ ; the plateau in the curve near 1400 K indicates liquefaction of the alloy charge while the horizontal line marks the bath setpoint temperature of 1523K.

**4.2 Discussion of Errors**

Several sources of uncertainty can be identified and related to the scatter in the data plots. These include the error introduced by the analytical method, uncertainty from the sampling procedure, i.e., with respect to the depth and position of the sampling point and the size of each sample, and contamination of the quartz sampling tubes. The error of analysis for S and O assays, according to INCO, was within 2 % of the determination; uncertainty due to contamination of the sampling tubes could not be easily identified while evaluation of the sampling error, by the simultaneous extraction of two samples at the same depth and position in the melt, could not be performed accurately due to technical constraints on the test apparatus. To minimize the sampling error, all attempts at sampling were directed to the bottom of the melt however this may have also introduced an additional source of uncertainty by stirring the melt. Having two unknown quantities it was not possible to separate the contribution of each error source in the computation of the sample variance or standard deviation. Other sources of error which were not considered in this analysis included the accumulated mass loss from the melt due to sampling, which did not exceed more than 5-6% of the initial charge mass, the periodic adjustments made to the gas rotameters to maintain the desired gas flowrate and with respect to comparisons and the difference in the charge masses between the experiments since this was usually less than 10%. Statistical anomalies in the elemental determinations, especially those of oxygen, may have been caused by the oxidation of the sample during its transfer to the quench bath or the withdrawal of oxidized surface material rather than bulk liquid from the melt.

The standard deviation of the S and O determinations applied in Tests 2-9 are mostly based on the pooled average of the sample standard deviations calculated from Test 2 while the values calculated in Test 1 were applied only to that experiment. This approach was used because the calculated deviation for S was higher in Test 2 over Test 1 while the standard deviation for oxygen in Test 1 was based on elemental determinations performed at McGill University rather than at INCO. The sample standard deviation for oxygen at low concentration (<0.01 wt % O) was estimated from one result in Test 4 to be 0.004 wt% since

a similar calculation could not be performed from the assays in Test 2. The standard deviation of oxygen determinations between 0.01 wt % and 1 wt % was taken as 0.020 wt % from while readings above 1 wt % O were not plotted with an assumed standard deviation. In all tests the standard deviation of the sulfur assays between 0.1 wt % and ~ 1 wt % was assumed to be 0.087 wt %; S assays below this range were not plotted with a standard deviation because no repeat determinations were performed on low sulfur samples which were near the limit of the analytical method.

The results of the nickel determinations in Test 4 and Test 9 are difficult to assess because repeated analysis of the samples consistently registered values higher than the mean concentration of the CNS master alloy ingot with almost no variance. The nickel standard solutions used for the analysis were reproduced several times without affecting the elemental determinations. Hence the high nickel readings may have arisen from contamination of the samples by the oxidized surface layer of the melts or the influence of an unaccounted minor element in solution with the melt samples; interference from dissolved copper was not considered because the relevant atomic absorption literature precluded that possibility.

Satisfactory regression analyses could not be performed on plotted data due to the high standard deviation of analysis in many of the samples following Test 1. The calculated standard deviation of the sulfur assays was 0.087 wt % and represented almost 10 % of the initial sulfur concentration whereas the standard deviation of the low oxygen measurements almost matched the elemental determination. As a result of the large uncertainty in the plotted data and therefore the numerous possibilities regarding the selection of a best fit curve attempts at regression analyses of the data were abandoned.

**5.1 Discussion of Results****5.1.1 Marangoni Convection**

The hypothesis presented in Chapter 2 presumed that sulfur removal from a copper-nickel-sulfur melt might be impeded by the cessation of Marangoni convection upon oxygen saturation of the melt and nickel oxide formation blocking the melt surface. Marangoni convection was not observed in any of the experiments performed at the selected oxygen flowrates. Slag accumulation on the melt surface in Test 1 obstructed surface observations yet in Test 2, where a lower oxygen flowrate and a CS alloy prepared in advance were used to prevent excessive slag formation, the melt surface remained highly visible and no instances of Marangoni convection were observed. Instead, a thin oxide film was seen swirling at low velocity on the melt surface but this motion could be attributed to the impinging gas glancing against oxidized particles. However, sulfur removal, in the absence of the slag layer, proceeded more rapidly in Test 2 over Test 1 in spite of the reduced gas flowrate (see Figure 50).

Due to the absence of Marangoni convection in Test 2, the oxygen flowrate in Test 3 (CS melt) was increased to 75 cm<sup>3</sup>/min while the test crucible was cemented to a wall extension and placed in a graphite receptacle intended to prevent melt spills and ejections from damaging the quartz reaction vessel. Test 4 and Test 6 were similarly conducted with charges of CNS alloy and cathode copper respectively. The results of these three tests (see Figure 51) revealed that oxygen dissolution was greatest in the CS alloy of Test 3 and while some sulfur removal took place in Test 3 none occurred in Test 4. No instances of Marangoni convection were witnessed in any of these three experiments but all the melts experienced surface oxidation, although not to the extent seen in Test 1. The effectiveness of the slag layer against the transfer of reactants or reaction products to and from the gas-liquid interface was made evident from the results of Test 2 and Test 3 (see Figure 52) where a greater degree of sulfur elimination was achieved in the former using a lower oxygen flowrate and where the observed surface oxidation was much less and partially in the form of a fluid film rather than a solid layer.

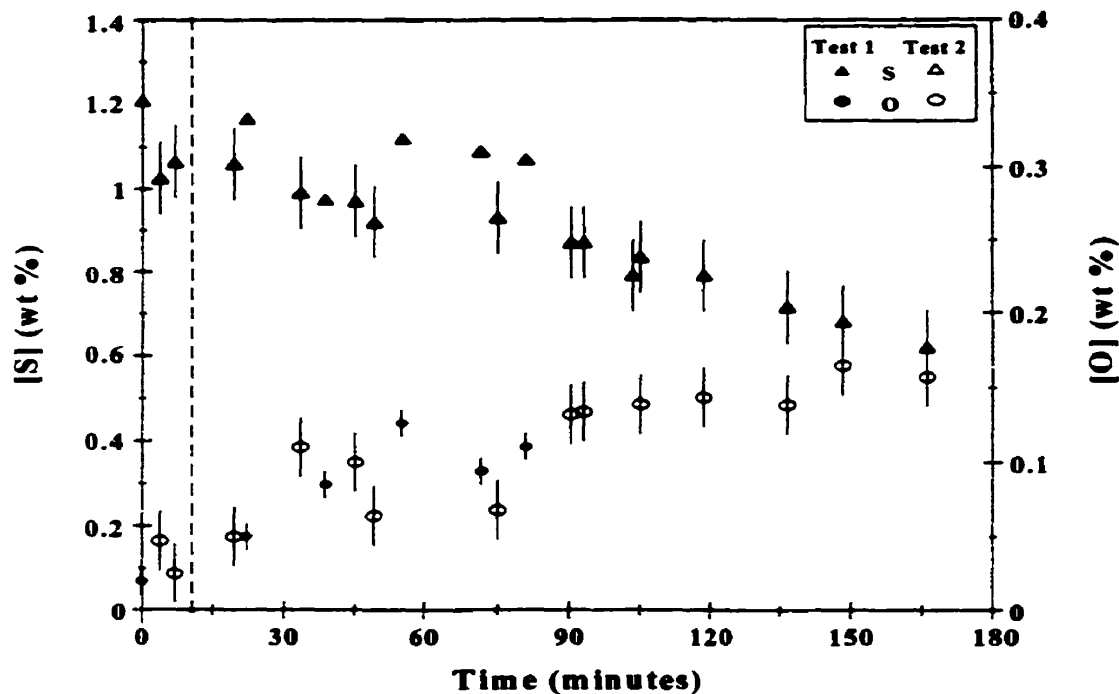


Figure 50. The concentration profiles over time in Tests 1 and 2 adjusted to the time scale of Test 1. The vertical line coincides with the start of O<sub>2</sub> delivery to both melts.

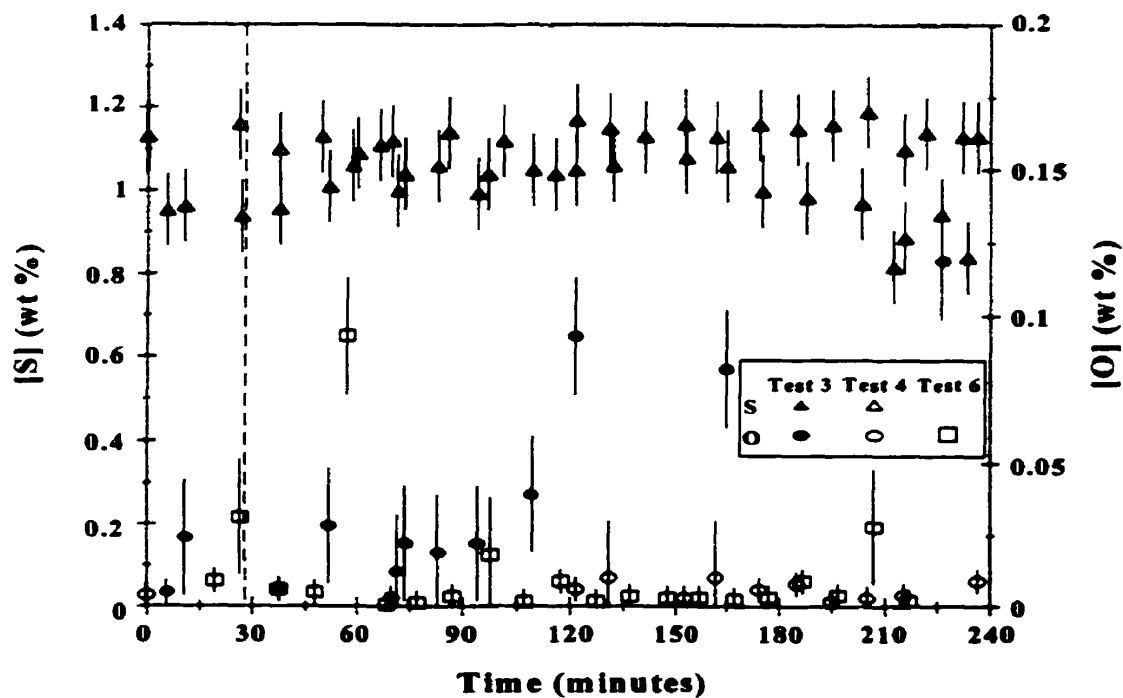


Figure 51. The concentration profiles over time in Tests 3,4, and 6 adjusted to the time scale in Test 3. The vertical line coincides with the start of O<sub>2</sub> delivery to all the melts.

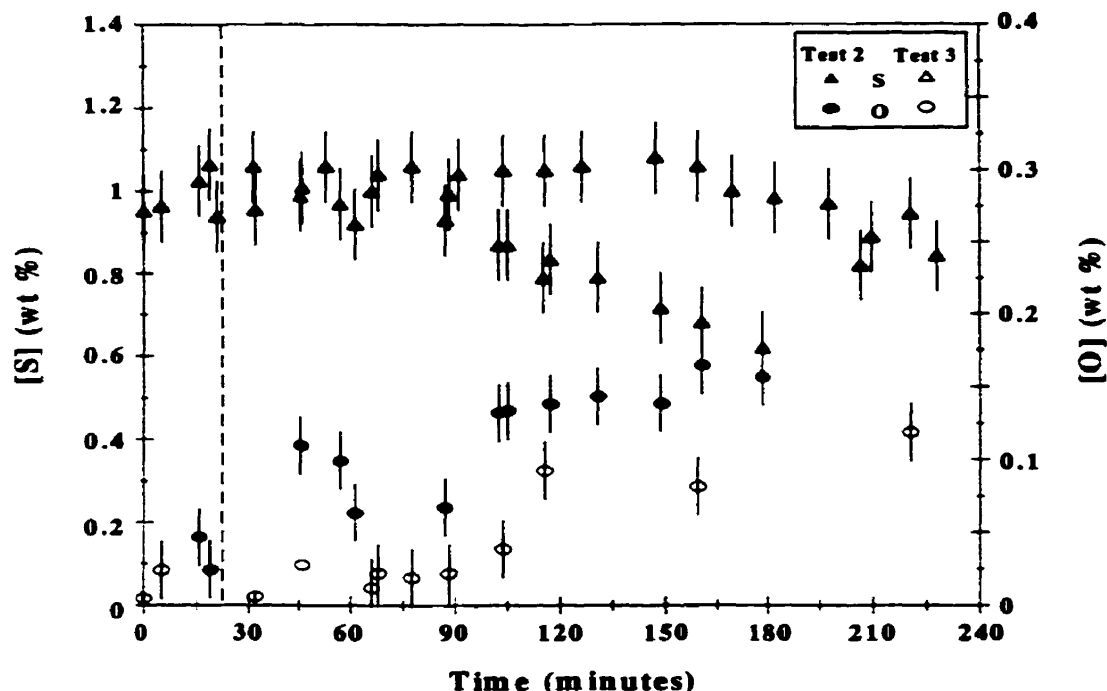


Figure 52. The concentration profiles over time in Tests 2 and 3 adjusted to the time scale of Test 3. The vertical line coincides with the start of  $O_2$  delivery to both melts.

### 5.1.2 The Role of Surface Films on Mass Transfer

Surface oxidation and hence the minor amount of desulfurization in Test 3 and Test 4 can be related to the blowing conditions and lack of melt agitation. Oxygen saturation of copper melts is typically in the range of 1 wt % at 1523 K and even higher for Cu-Ni melts according to the Cu-Ni-O phase diagram<sup>19,36</sup> (see Figure 7, Chapter 2) because nickel suppresses the activity coefficient of oxygen to about 0.7 at 1523 K<sup>37</sup> and hence increases oxygen activity. In Tests 1 - 6 the recorded oxygen values were much below oxygen saturation with the CNS alloy showing the least tendency to dissolve oxygen and the greatest likelihood to oxidize its metallic components.

Thermodynamics predicts that nickel oxidizes more readily than either copper<sup>105</sup> or sulfur; this was observed in Test 4 when the dissolved oxygen and nickel content of the melt had dropped as the oxygen flowrate was increased from 75 cm<sup>3</sup>/min to 372 cm<sup>3</sup>/min, presumably due to increased nickel oxidation, while the sulfur level remained unaffected. The low oxygen flowrates impinged on the melt surfaces did not induce any melt agitation

and in turn would have led to low rates of surface renewal thereby established and maintained large concentration gradients of oxygen between the melt surface and the bulk liquid. As previously mentioned in Chapter 2, Richardson<sup>71</sup> estimated that an iron melt containing one-tenth its saturation level of dissolved oxygen, would attain surface saturation with a monolayer of the dissolved species within milliseconds. If surface saturation is readily established in a stagnant melt then surface oxidation becomes thermodynamically favourable and the surface concentration gradients needed to drive Marangoni convection are dissipated. Some support to these arguments are also found in the observations made in Test 5. The crucible containing the cathode copper had failed almost immediately bringing the melt into partial contact with the graphite crucible for the duration of the experiment; the copper being continuously deoxidized was not subject to the surface coverage observed in Test 3, 4 and 6 and yet Marangoni convection did not take place. If the melt had been sufficiently stirred then rapid surface renewal may have maintained sufficient surface concentration gradients but under the prevailing bath conditions this may not have occurred.

### ***5.1.3 Melt Effervescence***

The difficulty in achieving substantial sulfur removal from Tests 1 through 4, prompted Tests 7 and 8, and 9, using CS and CNS alloy charges respectively, to be melted under air in order to measure desulfurization of unperturbed melts exposed to the open atmosphere. Knacke and Probst's<sup>96</sup> diagram (see Figure 15, Chapter 2) indicated that melting of a Cu-S alloy would lead to large scale sulfur evolution during melting or solidification and therefore the initial melt assays were not unexpectedly below 0.5 wt% S. Two conclusions relating to the earlier tests can be drawn: melting of the alloy charges under ultra-high purity nitrogen in Tests 2, 3 and 4 was necessary to prevent significant desulfurization prior to oxygen injection and evidence of melt ejections in these earlier tests can be partly attributed to SO<sub>2</sub> evolution during solidification of the charges upon completion of the tests. Although the melts in Tests 7 - 9 experienced surface oxidation, oxygen absorption and sulfur removal occurred to a greater extent in these tests over previous attempts with oxygen blowing at low flowrates. Desulfurization of the exposed melts was expected to be gradual in these

experiments. However in Tests 7 and 8 spontaneous effervescence for a 20 minute period caused disintegration or digestion of the oxidized surface layer and accelerated sulfur elimination; the CNS alloy charge in Test 9 did not experience turbulent eruptions and therefore sulfur elimination progressed gradually and to a lesser extent than in the CS melts (see Figure 53). At the time of the eruptions, the alloys had fully liquified and therefore the phenomenon could not be attributed solely to the melting process since several periods of effervescence were witnessed over the duration of the experiment separated by intervals of melt quiescence. Effervescence is believed to occur when the melt has reached a certain degree of oxygen super-saturation; the effervescence stops when the level of super-saturation or the 'driving force' for  $\text{SO}_2$  evolution is insufficient to nucleate bubbles.

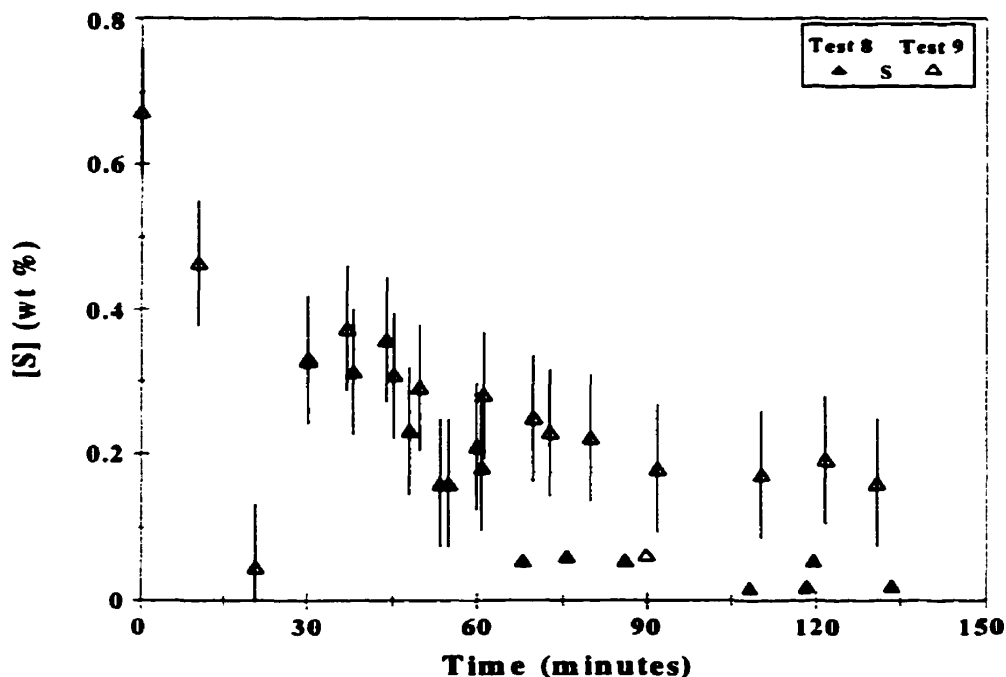


Figure 53. The S concentration profiles over time in Tests 8 and 9. The sampling time in Test 8 was adjusted to the time scale of Test 9 when a similar S concentration is observed in both melts.

Effervescence in Cu-S alloy melts was also witnessed by Rioux<sup>104</sup> while examining the effect of jet momentum on desulfurization from CS and CNS alloys melted in the test apparatus of this study and in similar conditions to Tests 7, 8 and 9. In Rioux's experiments, a pure oxygen gas stream was delivered onto the melt surface from a gas lance 1 cm above

the bath at 75 cm<sup>3</sup>/min, 500 cm<sup>3</sup>/min and 1000 cm<sup>3</sup>/min for the CS alloy and at 1000 cm<sup>3</sup>/min for the CNS alloy. The results of Rioux's experiments, reproduced in Figure 54 without alteration, show more rapid sulfur removal with increased oxygen delivery to the CS melt whereas sulfur elimination from the CNS alloy was slower than for the CS alloy blown at the same oxygen flowrate. A comparison of Rioux's CS alloy experiment blown with 75 cm<sup>3</sup> O<sub>2</sub>/min to the concentration profiles over time of Test 8 show a fair degree of similarity (see Figure 55) and indicates that this modest injection of oxygen contributed little if anything to the ensuing desulfurization. According to Rioux, increasing the gas flowrate accelerated the onset of effervescence in the CS melts but did not provoke Marangoni convection; it should be noted however that the turbulent conditions created on the melt surface at higher jet momentum could have precluded witnessing such an eventuality. Some bubbling observed by Rioux in the CNS melt was subdued compared to the eruptions of the CS alloy blown at the same oxygen flowrate; this result was probably due to the rapid coverage of the melt surface by NiO which also proceeded to consume the alumina sheath of the bath thermocouple and prematurely ended the test.

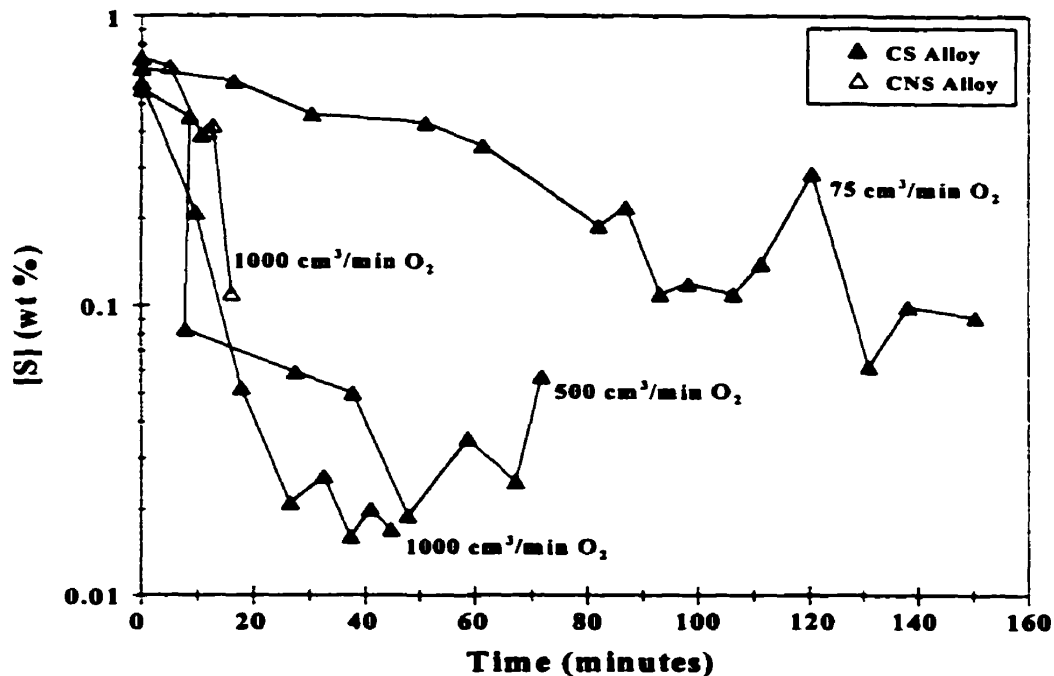


Figure 54. The S concentration profile from CS alloy blown with O<sub>2</sub> at 75 cm<sup>3</sup>/min, 500 cm<sup>3</sup>/min and 1000 cm<sup>3</sup>/min and from CNS alloy blown with oxygen at 1000 cm<sup>3</sup>/min, according to Rioux<sup>104</sup>.

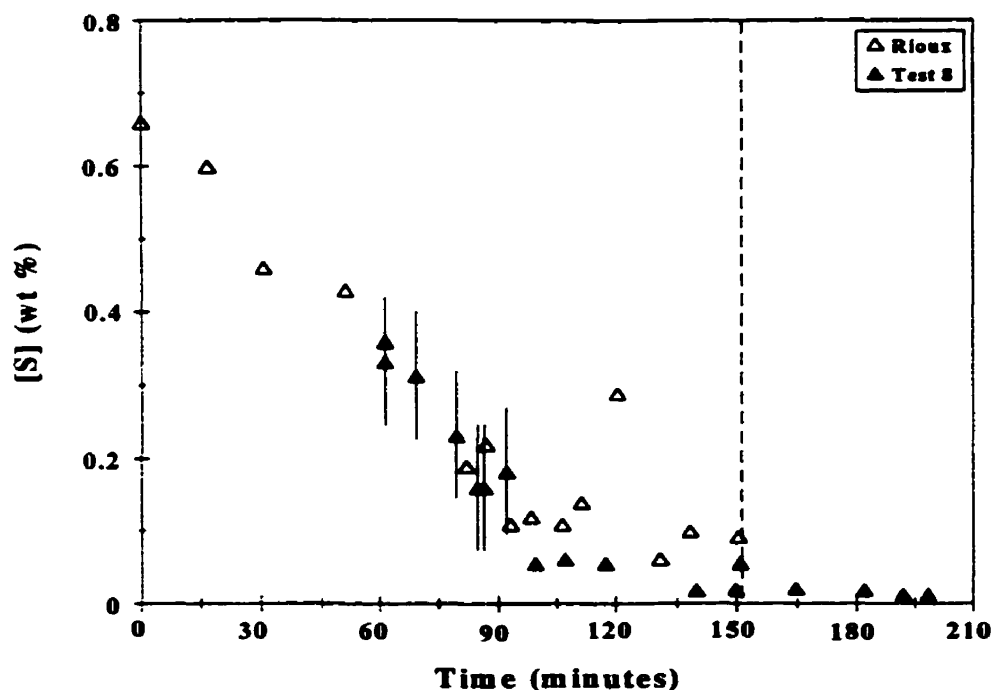


Figure 55. The S concentration profile over time in Test 8 compared to Rioux's testwork with CS alloy blown with oxygen at  $75 \text{ cm}^3/\text{min}$ . The time scale in Test 8 is adjusted to Rioux's sampling time when a similar S concentration is observed in both melts. The vertical line indicates the start of  $\text{O}_2$  blowing at  $75 \text{ cm}^3/\text{min}$  in Test 8.

## 5.2 Summary

This study failed to correlate the cessation of Marangoni convection as a factor in diminished sulfur elimination from Cu-Ni-S melts or observe surface tension driven flow in any of the copper and copper alloy melts used in this testwork. The causes of slow sulfur removal observed in this investigation can be attributed to the low oxygen flowrates used in the experiments which did not provide a sufficiently high rate of oxygen delivery to the melt or in turn agitate the liquid charges. As a consequence of melt quiescence large concentration gradients may have developed between the bath and the bulk liquid leading to surface oxidation and elimination of the surface concentration driving force required for Marangoni convection. In this regard, nickel oxidation in the copper-nickel-sulfur melts proved to be more effective in reducing or preventing desulfurization over the copper oxidation in the corresponding copper-sulfur melts. In the absence of Marangoni convection, melt effervescence was the only observed surface phenomenon that may have led to

accelerated sulfur elimination from the copper-sulfur melts; again nickel oxidation may have been responsible in suppressing this phenomenon and hence sulfur removal from the CNS liquid alloy. Under the conditions of low oxygen blowing and open atmosphere desulfurization the progress of sulfur elimination and oxygen dissolution should be considered in terms of resistance to mass transfer through an oxide layer rather than as a rate phenomenon.

Rioux's findings also corroborated that nickel oxidation impedes sulfur elimination from semi-blister melts even under increased melt agitation. Although effervescence was observed in the stagnant melts of CS alloy exposed to air in this study, Rioux demonstrated that its onset could be accelerated with more rapid oxygen delivery to the melt but also be suppressed by nickel oxidation on the melt surface. It is this author's opinion that as a result of nickel oxidation a correlation between the cessation of Marangoni convection and reduced sulfur elimination in INCO semi-blister copper cannot be satisfactorily established. Under both quiescent and agitated conditions in the melt, rapid surface coverage by nickel oxidation precludes the observation of Marangoni convection on the melt surface. The high degree of turbulent mixing required to disrupt this layer, which is already achieved in the INCO finishing converter by bottom blown gas injection, would create metallodynamic conditions where Marangoni convection could not be observed or its contribution to desulfurization be quantified.

***Test 1 to Test 6: Oxidation by a Low Momentum Oxygen Stream***

- 1) Marangoni convection was not observed in any of the melts impinged with oxygen at 66 cm<sup>3</sup>/min and 75 cm<sup>3</sup>/min. Instead the CS and CNS alloy underwent oxidation forming either a partially fluid film, as in Test 2, or a solid layer, as in Tests 3, 4 and 6, on the free surface.
- 2) Stagnant metallodynamic conditions in the melts helped sustain large concentration gradients between the gas-liquid interface and the bulk fluid by providing a low rate of surface renewal which made conditions favourable for the formation of oxide on the surface.
- 3) The surface slags formed in Tests 3, 4 and 6 impeded the transfer of reactants or reaction products to and from the gas-liquid interface. This effect was most pronounced in the CNS alloy melt whereby no discernable sulfur elimination was recorded.

***Test 7 to Test 9: Oxidation of CS and CNS Liquid Alloy in Air***

- 4) Sulfur elimination and oxygen dissolution in CS and CNS alloy melted under air proceeded more rapidly and to a greater degree than similar charges impinged with oxygen at low flowrates.
- 5) Increased sulfur elimination over earlier tests was attributed partly to the sudden evolution of SO<sub>2</sub> from the alloys, in the form of effervescence, in the course of melting them under air. Additional periods of effervescence experienced by the CS alloy charges disrupted the oxidized surface layer resulting in more rapid sulfur elimination as compared to a similarly tested CNS alloy melt which did not undergo any effervescence or eruptions thereby leaving the slag layer intact.

- 6) The onset of effervescence in liquid CS alloy is believed to occur when the melt achieves a certain degree of oxygen super-saturation. The effervescence stops when the level of super-saturation or the 'driving force' for SO<sub>2</sub> evolution is insufficient to nucleate bubbles but will reappear periodically if the melt continues to absorb oxygen until sufficient super-saturation is again reached. Once sufficient S has been removed such that the necessary super-saturation can no longer be attained the effervescence ceases since the dissolved oxygen concentration cannot exceed its level of saturation with respect to the Cu-O system,.
- 7) It is believed that the inability of the systems to achieve this level of super-saturation once sulfur is low enough and dissolved oxygen is high enough, that the oxygen content of the melt cannot be increased further and the mechanism of desulfurization changes to one in which there is no longer any SO<sub>2</sub> bubble nucleation as seen during effervescence. Consequently, desulfurization becomes slower in accord with the INCO observations during the second stage of the finishing procedure.
- 8) The Marangoni aspect of the hypothesis in Chapter 2 was not confirmed but a discovery was made about the nature of the desulfurization process in Cu-S baths, i.e., periodic effervescence.

Experiments have already been conducted by Rioux<sup>104</sup> as an extension to this investigation which examined the effect of gas jet momentum or the rate of oxygen delivery to the melt on the desulfurization of CS and CNS alloy melted under air.

It would be of interest to this author to further quantify the onset of effervescence in copper-sulfur melts by more accurate measurement of the sulfur and oxygen levels prior to bubbling since this phenomenon, to the knowledge of this author, has not been previously reported in copper melts. Rioux's assays did not involve oxygen determinations due to time and resource constraints while the scatter in the experimental data of this investigation did not provide an accurate indication to the onset of bubbling. Furthermore, it would be necessary to investigate whether the type of crucible used during experimentation may have contributed to effervescence.

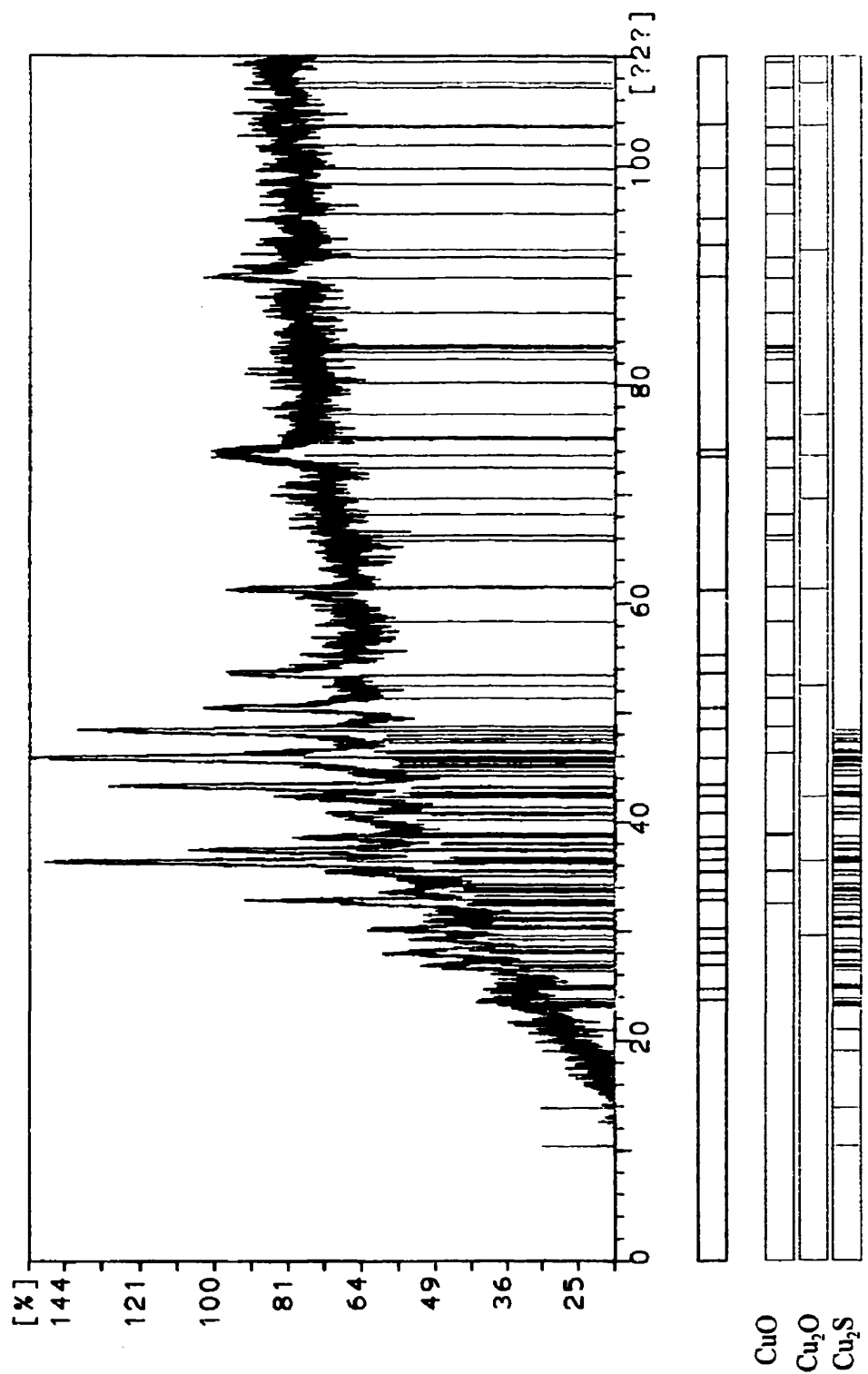


Figure A1. Qualitative identification of slag components in Test 1 by X-ray diffraction.



1. C.A. Landolt, A. Fritz, S.W. Marcuson, R.B. Crowx, J. Miszczak, Copper Making at INCO's Copper Cliff Smelter, *Proceedings of the Copper 91-Cobre 91 International Symposium, Vol. IV: Pyrometallurgy of Copper, August 18-21, 1991, Ottawa, Canada, International Symposium Organized by the Metallurgical Society of Canadian Institute of Mining, Metallurgy and Petroleum, Chilean Institute of Mining Engineers, and Minerals, Metals and Materials Society of the AIME*, ed. C. Diaz et al., Pergamon Press, Toronto, New York, 1991, pp 15-29.
2. C.A. Landolt, A Dutton, A. Fritz and S. Segsworth, Nickel and Copper Smelting at INCO's Copper Cliff Smelter, *Extractive Metallurgy of Copper, Nickel and Cobalt: Proceedings of the Paul E. Queneau International Symposium, Vol. II: Copper and Nickel Smelter Operations / sponsored by the Extraction and Processing Division of TMS and the Metallurgical Society of the Canadian Institute of Mining, Metallurgy and Petroleum (CIM)*, ed. C.A. Landolt, TMS, Minerals, Metals, Materials, Warrendale, PA. 1993, pp 1497-1528.
3. Ontario Government, Countdown Acid Rain, Ontario Ministry of the Environment, Toronto, 1987.
4. M.C. Bell, J.A. Blanco, H. Davies and P. Garritsen, Taking INCO into the 90s - The SO<sub>2</sub> Abatement Project, *CIM Bulletin*, Vol. 83, No. 933, 1990, pp 47-50.
5. J.A. Blanco and C.A. Landolt, SO<sub>2</sub> Abatement and Energy Conservation at Inco's Copper Cliff Smelter, Presented at the 73rd SCC/40th SCGCH Conference, Halifax, Nova Scotia, July 15-20, 1990.
6. C.A. Landolt, A. Dutton, J.D. Edwards, and R.N. McDonald, SO<sub>2</sub> Abatement, Energy Conservation and Productivity at Copper Cliff, *JOM*, Vol. 44, No. 9, 1992, pp 50-54.
7. J.R. Boldt Jr., *The Winning of Nickel*, Longmans Canada Ltd., Toronto, 1967, pp 275-283.
8. R.J. Neal and R.A. Reyburn, Converter Operating Practice at the Copper Cliff Smelter of INCO Metals Company, *Copper and Nickel Converters: Proceedings of a Symposium on Converter Operating Practices Sponsored by the TMS-AIME Pyrometallurgy Committee at the 108th AIME Annual Meeting in New Orleans, Louisiana, February 19-21, 1979*, ed. R.E. Johnson, Metallurgical Society of AIME, New York, 1979, pp 135-143.
9. A.A. Bustos, G.G. Richards, N.B. Gray and J.K. Brimacombe, Injection Phenomena in Nonferrous Processes, *Metall. Trans. B*, Vol. 15B, 1984, pp 77-89.
10. P.E. Queneau and S.W. Marcuson, Oxygen Pyrometallurgy at Copper Cliff - A Half

- Century of Progress, *JOM*, Vol. 48, No. 1, 1996, pp 14-21.
11. S.W. Marcuson, C. Diaz, and H. Davies, Top-Blowing, Bottom Stirring Process for Producing Blister Copper, *JOM*, Vol. 46, No. 8, 1994, pp 61-63.
  12. G.S. Victorovich, Oxygen Flash Converting for Production of Copper, *Extractive Metallurgy of Copper, Nickel and Cobalt: Proceedings of the Paul E. Queneau International Symposium, Vol. I: Fundamental Aspects*, sponsored by the Extraction and Processing Division of TMS and the Metallurgical Society of the Canadian Institute of Mining, Metallurgy and Petroleum (CIM), eds. R.G. Reddy and R.N. Weizenbach, TMS, Minerals, Metals, Materials, Warrendale, PA, 1993, pp 501-529.
  13. M.C. Bell, J.A. Bianco, H. Davies and R. Sridhar, Oxygen Flash Smelting in a Converter, *JOM*, Vol. 30, 1978, pp 9-14.
  14. H. Davies, S. Marcuson, G. Osborne, and A. Warner, Flash Converting of Chalcocite Concentrate at INCO's Port Colbourne Pilot Plant, *Extractive Metallurgy of Copper, Nickel and Cobalt: Proceedings of the Paul E. Queneau International Symposium, Vol. I: Fundamental Aspects*, sponsored by the Extraction and Processing Division of TMS and the Metallurgical Society of the Canadian Institute of Mining, Metallurgy and Petroleum (CIM), eds. R.G. Reddy and R.N. Weizenbach, TMS, Minerals, Metals, Materials, Warrendale, PA, 1993, pp 623-637.
  15. J.K. Brimacombe, S.E. Meredith and R.G.H. Lee, High Pressure Injection of Air into a Pierce-Smith Converter, *Metall. Trans. B*, Vol. 15B, 1984, pp 243-250.
  16. E.O. Hoefele and J.K. Brimacombe, Flow Regimes in Submerged Gas Injection, *Metall. Trans. B*, Vol. 10B, 1979, pp 631-648.
  17. G.N. Oryall and J.K. Brimacombe, The Physical Behavior of a Gas Injected Horizontally into Liquid Metal, *Metall. Trans. B*, Vol. 7B, 1976, pp 391-403.
  18. N.J. Themelis, P. Tarassoff and J. Szekely, Gas-Liquid Momentum Transfer in a Copper Converter, *Trans. Met. Soc. Aime*, Vol. 245, 1969, pp 2425-2433.
  19. C. Diaz, S. Marcuson, H. Davies and R. Stratton-Crawley, Conversion of Nickel and Sulfur-Containing Copper to Blister, *Proceedings of Copper 87, Vol. 4, Pyrometallurgy of Copper*, Organized by the Metallurgical Society of the Canadian Institute of Mining and Metallurgy, the Chilean Institute of Mining Engineers, the University of Chile, eds. C. Diaz et al., Facultad de Ciencias Fisicas y Matematicas, Universidad de Chile, Santiago, Chile, 1987-1988, pp 293-304.
  20. Private communication with S.W. Marcuson, Sept. 1993.

21. A.K. Biswas and W.G. Davenport, *Extractive Metallurgy of Copper*, 3rd ed., Pergamon, Tarrytown, N.Y., 1994, pp 194-199.
22. H.H. Kellogg, Thermochemical Properties of the System Cu-S at Elevated Temperature, *Can. Metal. Q.*, Vol. 8, No. 1, 1969, pp 3-23.
23. A. Yazawa and T. Azakami, Thermodynamics of Removing Impurities During Copper Smelting, *Can. Metal. Q.*, Vol. 8, No. 3, 1969, pp 257-261.
24. G.K. Sigworth and J.F. Elliot, The Thermodynamics of Dilute Liquid Copper Alloys, *Can. Metal. Q.*, Vol. 13, No. 3, 1974, pp 455-461.
25. A. Yazawa, Thermodynamic Considerations of Copper Smelting, *Can. Metal. Q.*, Vol. 13, No. 3, 1974, pp 443-453.
26. J.F. Elliot, Phase Relationships in the Pyrometallurgy of Copper, *Metall. Trans. B*, 1976, Vol. 7B, pp 17-33.
27. H. Jalkanen and M.H. Tikkanen, Equilibrium Studies on High-Copper Mattes, *Scand. J. Metallurgy*, Vol. 8, No. 2, 1979, pp 64-66.
28. R.C. Sharma and Y.A. Chang, A Thermodynamic Analysis of the Copper-Sulfur System, *Metall. Trans. B*, 1980, Vol. 11B, pp 575-583.
29. R. Schmid: A Thermodynamic Analysis of the Cu-O System with an Associated Solution Model, *Metall. Trans. B*, 1983, Vol. 14B, pp 473-481.
30. J.M. Larrain, S.L. Lee, H.H. Kellogg, Thermodynamic Properties of Copper-Sulfur Melts, *Can. Metal. Q.*, Vol. 18, No. 4, pp 395-400.
31. C.B. Alcock, *Principles of Pyrometallurgy*, Academic Press, New York, 1976, pp 170-179.
32. J.M. Larrain and S.L. Lee, Thermodynamic Properties of Copper-Nickel-Sulfur Melts, *Can. Metal. Q.*, Vol. 19, No. 2, 1980, pp 183-190.
33. S.L. Lee, J.M. Larrain, and H.H. Kellogg, Thermodynamic Properties of Molten Sulfides. Part III. The System Cu-Ni-S, *Metall. Trans. B*, Vol. 11B, 1980, pp 251-255.
34. W.J. Schlitt, R.H. Craig, and K.J. Richards, The Miscibility Gap and Distribution of Nickel in the Molten Cu-Ni-S, *Metall. Trans.*, Vol. 4, 1973, pp 1994-1996.

35. Y. Chuang and Y.A. Chang, Extension of the Associated Solution Model to Ternary Metal-Sulfur Melts, Cu-Ni-S, *Metall. Trans. B*, Vol. 13B, 1982, pp 379-385.
36. P. Taskinen, Liquidus Equilibria and Solution Thermodynamics in Copper-Rich Copper-Nickel-Oxygen Alloys, *Acta Polytechnica Scandinavica*, Chemistry Including Metallurgy Series, No. 145, Helsinki, 45 pp.
37. A.D. Kulkarni and R.E. Johnson, Thermodynamic Studies of Liquid Copper Alloys by Electromotive Force Method, Part II. The Cu-Ni-O and Cu-Ni Systems, *Metall. Trans.*, Vol. 4, 1973, pp 1723-1727.
38. U. Kuxmann and J. Riecke, Die Gleichgewichte Zwischen Nickel und Sauerstoff in Kupferschmelzen in Gegenwart von festem Nickeloxid bzw. nickeloxidhaltigen Schlacken, *Erzmetall*, 25, 1972, pp 395-404.
39. G. Astarita, *Mass Transfer with Chemical Reaction*, Elsevier Publishing, New York, 1967, pp 1.
40. F. Ajerch and J.M. Toguri, Oxidation Rates of Liquid Copper and Liquid Copper Sulfide, *Metall. Trans.*, Vol. 3, 1972, pp 2187-2193.
41. P. Schmitt and W. Wuth, Mass Transfer in Pyrometallurgical Top Blowing Systems, *Heat and Mass Transfer in Metallurgical Systems*, eds. D.B. Spalding and N.H. Afgan, MacGraw-Hill, 1981, pp 271-280.
42. A. Chatterjee and A.V. Bradshaw, Break-Up of a Liquid Surface by an Impinging Gas Jet, *J. Iron and Steel Inst.*, Vol. 210, Part 3, Mar. 1972, pp 179-187.
43. N.A. Molloy, Impinging Jet Flow in a Two-Phase System. The Basic Flow Pattern, *J. Iron and Steel Inst.*, Oct. 1970, Vol. 208, Part 10, pp 943-950.
44. K. Li, A Model Study of Splashing, *J. Iron and Steel Inst.*, Nov. 1960, Vol. 196, pp 275-291.
45. R.B. Banks and D.V. Chandrasekhara, Experimental Investigation of the Penetration of a High-Velocity Gas Jet Through a Liquid Surface, *J. Fluid Mech.*, Vol. 15, No. 3, 1963, pp 13-34.
46. F.R. Cheslak, J.A. Nicholls and M. Sichel, Cavities Formed on Liquid Surfaces by Impinging Gaseous Jets, *J. Fluid Mech.*, Vol. 36, No. 1, pp 55-63.
47. E.T. Turkdogan, Fluid Dynamics of Gas Jets Impinging on Surface of Liquids, *Chem. Eng. Sci.*, Vol. 21, 1966, pp 1133-1144.

48. F. Tanaka, R. Imai, T. Yanagiya and A. Fuwa, Energy Balance Analysis on Formation of Cavity and Splashing by Top-Blowing Gas Jet, *Metallurgical Review of MMIJ*, Vol. 12, No. 2, 1995, pp 46-59.
49. E. Kimura, Fundamental Research of Lancing Mechanism in Mitsubishi Continuous Smelting Furnace, *ISIJ International*, Vol. 23, 1983, pp 522-529.
50. R. Li and R.L. Harris, Interaction of Gas Jets with Model Process Liquids, *Pyrometallurgy '95, Papers Presented at the "Pyrometallurgy '95" Conference / Organized by the Institution of Mining and Metallurgy in Association with the Institute of Materials, and Held in Cambridge, England, from 10 to 12 July, 1995*. The Institution of Mining and Metallurgy, London, 1995, pp 107-123.
51. A.H. Castillejos and J.K. Brimacombe, Measurement of Physical Characteristics of Bubbles in Gas-Liquid Plumes. Part II. Local Properties of Turbulent Air-Water Plumes in Vertically Injected Jets, *Metall. Trans. B*, Vol. 18B, 1987, pp 659-671.
52. J. Liow and N.B. Gray, Slugging Resulting from Gas Injection in a Peirce-Smith Converter. Water Modelling, *Metall. Trans. B*, Vol. 21B, 1990, pp 987-996.
53. I.F. Taylor, J.K. Wright and N.B. Gray, Liquid Mixing Resulting From Reactive Gas Injection, *The Howard Worner International Symposium on Injection in Pyrometallurgy*, eds. M. Nilmani and T. Lehner, Melbourne, Australia, The Minerals, Metals and Materials Society, 1996, pp 163-174.
54. N.P. Bacon, J.H. Chesters and I.M.D. Halliday, Flow Patterns in Three Dimensional Shapes, *J. Iron and Steel Inst.*, July 1960, pp 286-292.
55. K. D. Peaslee and D. G. C. Robertson, Model Studies of Splash, Waves, and Recirculating Flows Within Steelmaking Furnaces, *Steelmaking Conference Proceedings, Vol. 77 1994*. Iron & Steel Soc of AIME, Warrendale, PA, pp 713-722.
56. D.G.C. Robertson, The Computation of the Kinetics of Reactions Between Multiple Phases, *EPD Congress 1995 : Proceedings of a Symposium /Sponsored by the Extraction and Processing Division, held at the TMS Annual Meeting in Las Vegas, Nevada, February 12-16, 1995*, ed. G.W. Warren, TMS, Warrendale, Pa., 1995, pp 347-361.
57. A. Chatterjee and A.V. Bradshaw, The Influence of Gas Phase Resistance on Mass Transfer to a Liquid Metal, *Metall. Trans.*, Vol. 4, 1973, pp 1359-1364.
58. R.J. Fruehan, Mass Transfer Between Liquid Metals and Injected Gases, *Metals Technology*, Vol. 7, Part 3, March 1980, pp 95-101.

59. J.K. Brimacombe, E.S. Stratigakos and P. Tarassoff, Mass Transfer Between a Horizontal, Submerged Gas Jet and a Liquid, *Metall. Trans.*, Vol. 5, 1974, pp 763-771.
60. W.G. Davenport, D.H. Wakelin and A.V. Bradshaw, Interaction of Both Bubbles and Gas Jets with Liquids, *Heat and Mass Transfer in Process Metallurgy: Proceedings of a Symposium Held by the John Percy Research Group in Process Metallurgy, Imperial College, London, 19 and 20 April 1966*, ed. A.W.D. Hills, The Institution of Mining and Metallurgy, London, 1967, pp 207-245.
61. W.F. Porter, F.D. Richardson and K.N. Subramanian, Some Studies of Mass Transfer Across Interfaces Agitated by Bubble, *Heat and Mass Transfer in Process Metallurgy: Proceedings of a Symposium Held by the John Percy Research Group in Process Metallurgy, Imperial College, London, 19 and 20 April 1966*, ed. A.W.D. Hills, The Institution of Mining and Metallurgy, London, 1967, pp 79-115.
62. N.J. Themelis and P.J. Mackey, Solid-Liquid and Gas-Liquid Interactions in a Bath-Smelting Reactor, *Proceedings of the Savard/Lee International Symposium on Bath Smelting: Proceedings of an International Symposium / Sponsored Jointly by the Minerals, Metals & Materials Society, the Iron & Steel Society and the Metallurgical Society of CIM*, eds. J.K. Brimacombe and P.J. Mackey, G.J.W. Kor, C. Bickert and M.G. Ranade, The Minerals, Metals and Materials Society, Warrendale, Pa., 1992, pp 353-375.
63. K. Mori and M. Sano, Interactions Between Injected Bubbles and Liquid Metals, *Scaninject: International Conference on Injection Metallurgy Lulea, Sweden, June 9-10, 1977 / Organized Jointly by MEFOS, Jernkontoret, MEFOS, Lulea, Sweden 1977*, pp 348-354.
64. H. Lohe, Zum Wärme- und Stoffaustausch beim senkrechten Aufblasen von Gasstrahlen auf Flüssigkeitsoberflächen, *Chem. Ing. Tech.*, Vol. 38, pp. 309-314.
65. J. Szekely and N.J. Themelis, *Rate Phenomena in Process Metallurgy*, Wiley-Interscience, New York, 1971, pp 724-728.
66. A.H. Alyaser, *Oxidation Kinetics of Molten Copper Sulphide*, Master's Thesis, The University of British Columbia, 1993, 220 pp.
67. S. Taniguchi, A. Kikuchi and S. Maeda, Model Experiments on Mass Transfer in Gas Phase Between an Impinging Jet of Gas and Liquid Iron, *Testu-to-Hagane*, 1976, Vol. 62, No. 2, pp 191-200.
68. S. Taniguchi, A. Kikuchi and S. Maeda, Kinetics of Oxidation of Graphite by the

- Impinging Jet of Gas, Testu-to-Hagane, 1977, Vol. 63, No. 7, pp 1071-1080.
69. S. Taniguchi, A. Kikuchi, T. Tadaki and S. Maeda, Numerical Analysis on the Gas-Phase Mass Transfer Between an Impinging Jet of Gas and Liquid Iron, *Testu-to-Hagane*, 1979, Vol. 65, No. 13, pp 1830-1873.
70. S. Taniguchi, A. Kikuchi, T. Tadaki and S. Maeda, Fluid Flow and Mass Transfer in the Gas-Liquid Iron System with a Laboratory-Scale Induction Furnace, *Metallurgical Applications of Magnetohydrodynamics: Proceedings of a Symposium of the International Union of Theoretical and Applied Mechanics held at Trinity College, Cambridge, UK, 6-10 September 1982*, eds. H.K. Moffat and M.R.E. Proctor, The Metals Society, London, 1984.
71. F.W. Richardson. *Physical Chemistry of Melts in Metallurgy*, Academic Press, New York, 1974, pp 426-439.
72. J.K. Brimacombe, Interfacial Turbulence in Liquid-Metal Systems, *Physical Chemistry of Process Metallurgy, Papers Presented at the July 1973 Conference / The Richardson Conference*, eds. J. H. E. Jeffes and R. J. Tait, The Institution of Mining and Metallurgy, London, 1974, pp 175-185.
73. K. Monma and H. Suto, Effects of Dissolved Sulphur, Oxygen, Selenium and Tellurium on the Surface Tension of Liquid Copper, *Trans. JIM*, Vol. 2, 1961 pp 148-153.
74. G.R. Belton, The Interplay Between Strong Adsorption of Solutes and Interfacial Kinetics at the Liquid Metal Surface, *Can. Metal. Q.*, Vol. 21, No. 2, 1982, pp 137-143.
75. G.R. Belton, Langmuir Adsorption, the Gibbs Adsorption Isotherm, and Interfacial Kinetics in Liquid Metal Systems, *Metall. Trans. B*, Vol. 7B, 1976, 35-42.
76. S. Sun and G.R. Belton, The Effect of Sulfur on the Interfacial Rates of Reaction of CO<sub>2</sub> and CO with Liquid Copper, *Metall. and Mat. Trans. B*, Vol. 29, 1998, pp 296-298.
77. B. Gallois and C.H. Lupis, Effect of Oxygen on the Surface Tension of Liquid Copper, *Metall. Trans. B*, Vol. 12B, 1991, pp 549-557.
78. G. Bernard and C.H.P. Lupis, The Surface Tension of Liquid Silver Alloys. Part II. Ag-O Alloys, *Metall. Trans.*, Vol. 2, 1971, pp 2991-2998.
79. F.D. Richardson, Interfacial Phenomena and Metallurgical Processes, *Can. Metal. Q.*,

- Vol. 21, No. 2, 1982, pp 111-119.
80. L.S. Darken and E.T. Turkdogan, Adsorption Kinetics at Elevated Temperature, Heterogeneous Kinetics at Elevated Temperatures : Proceedings of an International Conference in Metallurgy and Materials Science Held at the University of Pennsylvania, eds. G.R. Belton and W.L. Worrell, Plenum Press, New York, 1970. pp 25-95.
  81. R.J. Fruehan and L.J. Martonik, The Rate of Absorption of Nitrogen into Liquid iron Containing Oxygen and Sulfur, *Metall. Trans. B*, Vol. 11B, 1980, pp 615-622.
  82. R.J. Fruehan and L.J. Martonik, The Rate of Absorption of Hydrogen into Iron and of Nitrogen inot Fe-Cr and Fe-Cr-Ni Alloys Containing Sulfur, *Metall. Trans. B*, Vol. 12B, 1981, pp 379-384.
  83. L.E. Scriven and C.V. Stermling, The Marangoni Effects, *Nature*, Vol. 187, 1960, pp 186-188.
  84. K. Mukai, Wetting and Marangoni Effect in Iron and Steelmaking Processes, *ISIJ International*, Vol. 32, No. 1, 1992, pp 19-25.
  85. Foam, *Van Nostrand's Scientific Encyclopedia*, 8th ed., ed. D.M. Considine, Van Nostrand Reinhold, Toronto, 1995, pp 1300-1301.
  86. P. Sahoo, T. Debroy and M.J. McNallan, Surface Tension of Binary Metal- Surface Active Solute Systems under Conditions Relevant to Welding Metallurgy, *Metall. Trans. B*, Vol. 19B, 1988 pp 483-491.
  87. A.H. Alyaser and J.K. Brimacombe, Oxidation Kinetics of Molten Copper Sulfide, *Metall. and Mat. Trans. B*, Vol. 26, 1995, pp 25-40.
  88. N. Hirashima, R.T.C. Choo, J.M. Toguri and K. Mukai, The Effect of Surface Movements on Nitrogen Mass Transfer in Liquid Iron, *Metall. Trans. B*, Vol. 26B, 1995, pp 971-980.
  89. J.K. Brimacombe and F. Weinberg, Observations of Surface Movements of Liquid Copper and Tin, *Metall. Trans.*, Vol. 3, 1972, pp 2298-2299.
  90. K.W. Lange and M. Wilken, Marangoni Type Interfacial Phenomena in High and Low Temperature Systems, *Can. Metal. Q.*, Vol. 22, No. 3, 1983, pp 326.
  91. R.J. Barton and J.K. Brimacombe, Influence of Surface Tension-Driven Flow on the Kinetics of Oxygen Absorption in Molten Copper, *Metall. Trans. B*, Vol. 8B, 1977,

- pp 417-427.
92. Z. Asaki, S. Ando, and Y. Kondo, Oxidation of Molten Copper Matte, *Metall. Trans. B*, Vol. 19B, 1988, pp 47-52.
  93. Y. Fukunaka, K. Nishikawa, H.S. Sohn, and Z. Asaki, Desulfurization Kinetics of Molten Copper by Gas Bubbling, *Metall. Trans. B*, Vol. 22B, 1991, pp 5-11.
  94. Reiichi Ohno, Desulfurization and Deoxidation of Cu-S-O Alloy in Induction Melting and Solidification under Argon and Their Rates of Elimination in Vacuum Induction Melting, *Metall. Trans. B*, Vol. 22B, 1991, pp 405-416.
  95. C.F. Floe and J. Chipman, Effect of Impurities on the Solubility of Sulphur Dioxide in Molten Copper, *Trans. AIME*, 1942, Vol. 147, pp 28-38.
  96. O. Knacke and H. Probst, The Evolution of Gases in Copper on Solidification, *Metallurgical Chemistry*, ed. O. Kubaschewski, Her Majesty's Stationary Office, London, 1972, pp 527-31.
  97. G. Rottmann and W. Wuth, Conversion of Copper Matte by use of the Top-Blowing Technique, *Copper Metallurgy: Practice and Theory: Papers Presented at a Meeting Organized by the Institution of Mining and Metallurgy, With The Cooperation of the Centre Belge d'Information du Cuivre, and Held in Brussels, Belgium, on 11 February 1975*, ed. M.J. Jones. Institution of Mining and Metallurgy, London, 1975, pp 49-52.
  98. V.A. Bryukvin, O.I. Tsybin, L.I. Blokhina, and G.N. Zviadadze, An Investigation of the Oxidation Kinetics of a Copper Sulfide Melt with Oxygen, *Russ. Metall. (Engl. Trans.)*, No. 5, 1978, pp 24-28.
  99. H. Jalkanen, Phenomenology of the Oxidation Kinetics of Molten Cuprous Sulphide and Copper, *Scand. J. Metallurgy*, Vol. 10, 1981, pp 257-262.
  100. J.J. Byerley, G.L. Rempel, and N. Takebe, Interaction of Copper Sulfides with Copper Oxides in the Molten State, *Metall. Trans.*, Vol. 5, 1974, pp 2501-2506.
  101. P.T. Morland, S.P. Matthew, and P.C. Hayes, The Kinetics of S<sup>35</sup> Exchange between SO<sub>2</sub>/CO/CO<sub>2</sub> Gas Mixtures and Copper Sulfide Melts at 1523 K, *Metall. Trans. B*, Vol. 22B, 1991, pp 211-217.
  102. R.J. Barton and J.K. Brimacombe, Interfacial Turbulence During the Dissolution of Solid Cu<sub>2</sub>S in Molten Copper, *Metall. Trans. B*, Vol. 7B, 1976, pp 144-145.

103. F.P. Incropera, *Introduction to Heat Transfer*, 2nd ed., Wiley, New York, 1990, pp 681.
104. D. Rioux, The Effect of Oxygen Jet Momentum on the Rate of Desulfurization of Inco Semi-Blister Copper, B. Eng. Research Project, McGill University, 1998, 32 pp.
105. A. Yazawa and S. Nakazawa, Comparisons Between Copper, Lead and Nickel Smelting Processes from Thermodynamic Viewpoints, *Sulfide Smelting '98: Current and Future Practices, Proceedings of the Symposium Held at the 1998 TMS Annual Meeting, San Antonio, Texas, February 16-19, 1998 with additional pyrometallurgy papers presented at the 1997 TMS Annual Meeting, Orlando, Florida, February 10-13, 1997*, eds. J.A. Asteljoki and R.L. Stephens, TMS, Warrendale, Pa., 1998, pp 39-48.